THE APPLICATION OF THE KELVIN PROBE IN MATERIALS SCIENCE

Bert Lägel

This thesis is submitted to the Robert Gordon University in partial fulfilment of the requirement for the award of the degree of Doctor of Philosophy (PhD).

Submitted: August 2000

This research project was carried out in collaboration with the Defence and Evaluation and Research Agency.

Abstract

This thesis reports on the application of the Kelvin probe in materials science and in particular on the study of metal and semiconductor surfaces in both ambient and UHV environments. The concept of the work function ϕ and its importance as a parameter in materials science is discussed in the context of novel technological applications. The various methods to determine the work function are reviewed. The main measurement technique used here – the Kelvin probe - is described in detail.

The Kelvin probe measures local work function differences between a conducting sample and a reference tip in a non-contact, truly non-invasive way over a wide temperature range. However, it is an inherently *relative* technique and does not provide an *absolute* work function if the work function of the tip (ϕ_{tip}) is not known. Therefore, a novel technique has been developed to measure ϕ_{tip} with the Kelvin probe via the photoelectric effect, thus combining the advantages of both methods to provide the absolute work function of the sample surface.

High and low work function surfaces were generated as target materials for a novel ion source based on hyperthermal surface ionisation: oxidised rhenium exhibits the highest work function of 7.15eV at a temperature of ~900K whereas the lowest work function of ~2.54eV was measured on lanthanum hexaboride, LaB_6. The process of thermal and hyperthermal surface ionisation (SI, HSI) as well as the generation of hyperthermal molecular beams is discussed and a model of the surface ionisation process is developed to estimate its efficiency. Experimental data of SI and HSI are presented.

The application of the Kelvin probe for the detection of defects and impurities in semiconductors, namely iron contamination, is demonstrated via two methods based on the measurement of the surface photovoltage. We find that both methods yield a lower surface potential and surface charge for iron contaminated wafers compared to a clean sample and therefore can be used as an indicator for chemical contamination on semiconductor surfaces.

Acknowledgements

I am pleased to express my thanks to all the people who helped and assisted me in the completion of this thesis and during my stay in Scotland. Many thanks go to my supervisor Prof. Iain Baikie for the helpful and interesting discussions regarding the project and for his support and advice in a number of things in the everyday life of a researcher: from the supervision of students to refereeing of publications.

I have very much enjoyed working with Uwe Petermann who is known for his constructive ideas in solving technical problems. I am also indebted to P. Mertens and K. Kenis from IMEC (Leuven, Belgium) for the preparation of the iron contaminated Si wafers and to our collaborators from DERA, i.e. Alison Speakman, Marian Langford, Ian Pleasants and Matthew Brookes. I am most grateful for the help and assistance of Iain Tough, Peter Reid and Allan MacPherson. Finally, a special thank to my parents for their support and encouragement throughout all my studies.

This thesis is based on the following publications:

I. "A Novel Detection System For Defects And Chemicals Contamination In Semiconductors Based Upon The Scanning Kelvin Probe", B. Lägel, I.D. Baikie and U. Petermann in *Defect and Impurity Engineered Semiconductors and Devices II*, edited by S. Ashok, J. Chevallier, K. Sumino, B.L. Sopori, W. Goetz, (Mater. Res. Soc. Proc. **510**, Pittsburgh, PA, 1998), pp. 619-625.

II. "UHV Compatible Spectroscopic Scanning Kelvin Probe for Surface Analysis", I.D. Baikie, U. Petermann and B Lägel, *Surf. Sci.* **433**, 249 (1999).

III. "A Novel Detection System For Defects And Chemicals Contamination In Semiconductors Based Upon The Scanning Kelvin Probe", B. Lägel, I.D. Baikie, U. Petermann, *Surf. Sci.* **433**, 622 (1999).

IV. "In Situ Work Function Study Of Oxidation And Thin Film Growth On Clean Surfaces", I.D. Baikie, U. Petermann and B. Lägel, *Surf. Sci.* **433**, 770 (1999).

V. "Work Function Study of Rhenium Oxidation Using A UHV Scanning Kelvin Probe", I.D. Baikie, U. Petermann, A. Speakman, B. Lägel, K.M. Dirscherl, P.J. Estrup, *J. Appl. Phys.* **88**, 1 (2000).

VI. "Work Function Study Of Polycrystalline Metals Using A UHV Scanning Kelvin Probe", U. Petermann, I.D. Baikie, B. Lägel, K.M. in *Materials Science of Novel Oxide-Based Electronics*, edited by D.S. Ginley, D.M. Newns, H. Kawazoe, A.B. Kozyrev, J.D. Perkins Gossen (Mater. Res. Soc. Proc. **623**, Pittsburgh, PA, 2000) pp. G6.6.1-G6.6.6.

VII. "Work Function Study For The Search of Efficient Target Materials For Use In Hyperthermal Surface Ionisation Using a Scanning Kelvin Probe", U. Petermann, I.D. Baikie, B. Lägel, K.M. Dirscherl in *Polycrystalline Metal and Magnetic Thin Films*, edited by L. Gignac, O. Thomas, J. MacLaren, B. Clemens (Mater. Res. Soc. Proc. **615**, Pittsburgh, PA, 2000) pp. 37-42.

VIII. "A Novel Method For True Work Function Determination Of Metal Surfaces By Combined Kelvin Probe And Photoelectric Effect Measurements", B. Lägel,

I.D. Baikie, K.M. Dirscherl, U. Petermann, in *Recent Developments in Oxide and Metal Epitaxy – Theory and Experiment*, edited by M. Yeadon, S. Chiang, R.F.C. Farrow, J.W. Evans, O. Auciello (Mater. Res. Soc. Proc. **619**, Pittsburgh, PA, 2000) pp. 73-78.

IX. "A Novel Approach For True Work Function Determination Of Electron-Emissive Materials By Combined Kelvin Probe And Photoelectric Effect Measurements", B. Lägel, I.D. Baikie, K. Dirscherl and U. Petermann in *Electron-Emissive Materials, Vacuum Microelectronics and Flat-Panel Displays*, edited by K.L. Jensen, W. Mackie, D. Temple, J. Itoh, R. Nemanich, T. Trottier, P. Holloway (Mater. Res. Soc. Proc. **621**, Pittsburgh, PA, 2000) pp. R3.5.1 - R3.5.7.

Related Papers:

X. "Kelvin Probe Study Of Metastable States During Initial Oxygen Adsorption Dynamics On Si(111) 7×7", U. Petermann, I.D. Baikie, B. Lägel, *Thin Solid Films* **343-344**, 492 (1999).

XI. "Kelvin Probe and Ultraviolet Photoemission Measurements of Indium Tin Oxide Work Function: A Comparison" J.S. Kim, B. Lägel, E. Moons, N. Johansson, I.D. Baikie, W.R. Salaneck, R.H. Friend, F. Cacialli, *Synth. Met.* **111-112**, 311 (2000).

Contents

Chapter 1

Introduction

This thesis reports on applications of Contact Potential Difference (CPD) measurements via the Kelvin method [1] in materials science. It focuses on two important areas:

(i) the production and characterisation of polycrystalline metal targets for advanced mass spectroscopy systems and,

(ii) the detection of defects and impurities in semiconductor substrate wafers.

For the characterisation of these materials a novel Scanning Kelvin Probe (SKP) was employed, compatible with both air and Ultra-High Vacuum (UHV) environments. The SKP directly measures surface parameters such as changes in work function ϕ and surface potential ψ_S that are directly related to the state of the specimen surface. Any change in the electrical character of the surface, e. g. due to the adsorption of atoms, molecules, ions or absorption of photons, will reflect in a change of these parameters. Major advantages of the Kelvin method include its wide temperature compatibility (2-900) K, application in air, vacuum and liquid environments and its non-contact, non-destructive nature.

The first project was carried out in collaboration with the UK's Defence Evaluation and Research Agency (DERA). The aim of this project was to produce and characterise surfaces optimised for Hyperthermal Surface Ionisation (HSI), an alternative to Electron Impact (EI) ionisation for a novel mass spectrometer system. Analytical merits of this technique include very high sensitivity and substantially reduced amount of cracking products. This considerably simplifies the identification of molecules with high

molecular weights. This novel analytical technique therefore has potential applications for the detection and identification of trace amounts of explosives, drugs and in environmental sensing.

The second issue is of tremendous practical importance as defects and impurities in semiconductors, notably iron, are a major cause for concern in current wafer-scale semiconductor processing. Even minute amounts of impurities can alter the electrical characteristics of semiconductor devices considerably [2]. Because of its very high sensitivity to surface condition, the Kelvin probe, extended by Surface Photovoltage (SPV) measurement, is considered as an ideal tool for the detection of semiconductor defects and chemical contamination.

In this chapter we give a brief introduction into the issues covered in this thesis. In chapter 2 we treat the concept of the work function ϕ and review the various techniques for its measurement. In chapter 3 we discuss a novel approach to measure the absolute work function of metals and semiconductors by combined Kelvin probe and photoelectric effect measurements, thereby combining the advantages of both methods. Chapter 4 comprises a work function study of polycrystalline metal surfaces in order to determine the optimum conditions necessary to generate high and low work function surfaces required for the production of positive and negative ions via HSI, respectively. In chapter 5 we discuss the principle of Surface Ionisation (SI) and HSI as well as the generation of hyperthermal molecular beams and demonstrate the generation of positive and negative ions via SI and HSI. Finally, in chapter 6, we outline the theory of the surface photovoltage for both dc and ac light injection and demonstrate the application of the Kelvin probe to detect defects and chemical contamination in semiconductors via SPV measurements.

KELVIN PROBE MEASUREMENT MODES

The Kelvin probe is usually described as a vibrating capacitor device [3] that is used to measure the work function difference between a reference electrode (the Kelvin probe tip) and the sample under investigation. However, its technical realisation [4, 5] allows a much more versatile use of the device which may therefore be described in more general terms as a current sensing device. We will briefly describe the different measurement modes the Kelvin probe can be operated in and which were used in the projects of this thesis.

The basic electrical circuit of the Kelvin probe is a simple capacitor arrangement where the sample under investigation and the reference electrode of the Kelvin probe form the two plates (A and B) of this capacitor, see figure 1-1.

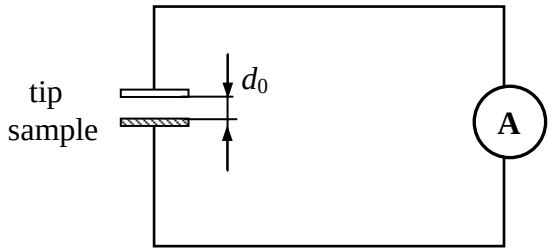

***Figure 1-1**. Schematic of the basic Kelvin probe showing the capacitor arrangement of the reference tip and the sample separated at a distance d_0, the external electrical connection and the meter sensing the current in the circuit.*

This Kelvin capacitor can thus be described by the equation for an ideal parallel plate capacitor:

$$C = \frac{\varepsilon_0 \varepsilon_r A}{d_0}, \qquad 1\text{-}1$$

where C is the capacity of the arrangement, ε_0 is the permittivity, A is the area of the capacitor plates and d_0 the distance between the plates. The dielectric constant ε_r is assumed to be equal to 1 for measurements in air or vacuum.

The capacity of the arrangement is related to the electrical charge at the plates Q and the voltage across the capacitor V by

$$Q = CV \,. \qquad 1\text{-}2$$

The current I that is sensed by the Kelvin probe as shown in figure 1-1 is defined as

$$I = \frac{dQ}{dt}. \qquad 1\text{-}3$$

Therefore, a current can be induced in the circuit by either a varying capacity or voltage which can be described by combining equations 1-2 and 1-3 to the equation given below by

$$I = V \cdot \frac{dC}{dt} + C \cdot \frac{dV}{dt}. \qquad 1\text{-}4$$

The *first* part of the equation, $I = V \cdot \frac{dC}{dt}$, describes the conventional contact potential difference (CPD, V_{CPD}) measurement mode where V_{CPD} is constant and the reference tip is vibrated with respect to the sample plate thus producing a varying capacitor. This mode is explained in more detail in chapter 2.

The *second* part of equation 1-4, $I = C \cdot \frac{dV}{dt}$, where the capacity is held constant, allows to measure externally induced changes in the work function or surface potential of the sample. This mode was used to measure changes in the surface potential in semiconductors via sine wave modulated light injection. This change in the surface potential of semiconductors with illumination is based on the phenomenon of surface photovoltage (SPV). Measurement of the SPV, as discussed in chapter 6, can give valuable information about potential contamination and defects in semiconductors.

Further, the Kelvin probe can be used to directly measure a flow of charge between the plates induced by electrons or ions. This third mode was utilised for photoelectric effect measurements, see chapter 3, and for the collection and measurement of ions created by SI and HSI, see chapter 5.

HYPERTHERMAL SURFACE IONISATION

Hyperthermal surface ionisation (HSI) is a novel ionisation technique that has been extensively investigated by Danon and Amirav [6]. The characteristics of this technique make it very attractive as an ionisation source for mass-spectrometric applications. By using suitable target materials HSI becomes extremely sensitive and the minimum detection levels are vastly improved. Further, HSI mass spectra exhibit a unique fragmentation pattern which consists of a much smaller amount of cracking products, in contrast to e.g. electron impact ionisation, and are therefore much more informative [7]. This opens up a vast variety of possible analytical and general applications for HSI, e.g. for the detection of drugs [8] and explosives [9], fast gas chromatography mass spectrometry (GC-MS) [7, 10] or as a novel ion source for ion guns and leak detection [7].

HSI is based on the well-known phenomenon of surface ionisation [11]. However, in this technique the ionisation process is realised under thermal non-equilibrium conditions where the species to be ionised is accelerated in a hyperthermal molecular beam to energies in the range (1-20)eV towards a target surface. If the molecule comes closer than a certain critical distance to the target surface, a spontaneous electron transfer can occur either to or from the molecule, depending on the energetic difference between the surface work function and the electron affinity of the molecule (for

negative ion hyperthermal surface ionisation - nHSI) or on the ionisation potential of the molecule minus the surface work function (for positive ion hyperthermal surface ionisation -pHSI), respectively. The kinetic energy of the molecule effectively assists this ionisation process by bridging the energy gap between the surface work function and either the molecular electron affinity or the ionisation potential of the molecule [6].

A key factor for the ionisation efficiency in HSI is therefore the work function of the target material. In a study commissioned by DERA searching for suitable target materials for a new mass spectrometer detection system the Kelvin probe has been efficiently utilised to characterise potential target surfaces with respect to their work function [12, 13].

In conjunction with this study our research group was awarded an EPSRC-JREI grant which provided the possibility to purchase a customised UHV system comprising a SKP, a four pocket electron beam evaporator, a Balzers mass spectrometer with a mass range from 1-200 amu and a specially designed gas inlet system with a pulsed nozzle valve (PNV) for HSI studies. The enhanced possibility with this equipment allowed to produce customised high and low work function layers and evaluate these surfaces with respect to their suitability and efficiency for HSI. Therefore the generation and characterisation of high and low work function surfaces and the implementation and testing of the HSI system are main objectives of this thesis.

REQUIREMENTS FOR FUTURE SEMICONDUCTOR DEVICES

Two of the major driving forces in modern technological applications are the semiconductor processing and computer manufacturing industries. They have experienced an unprecedented revenue growth from $126 billion in 1998 to $140 billion for 1999 [14]. Over 1 million people are employed world-wide in this sector which has shown an unrivalled growth rate of 11% over the last 12 months. Indeed, Moore's Law [15], graphically depicted in figure 1-2, has been a strong predictor of minimum feature size and thus miniaturisation of chip components and indicates that technological development must continue in order to sustain economic viability.

Applications of semiconductors range from single wafer devices for high power, high-speed (microwave) application to very high level integration (VLSI) devices, reaching a minimum size features of under 100 nm, corresponding to approximately 200 atomic layers, within the next 10 years.

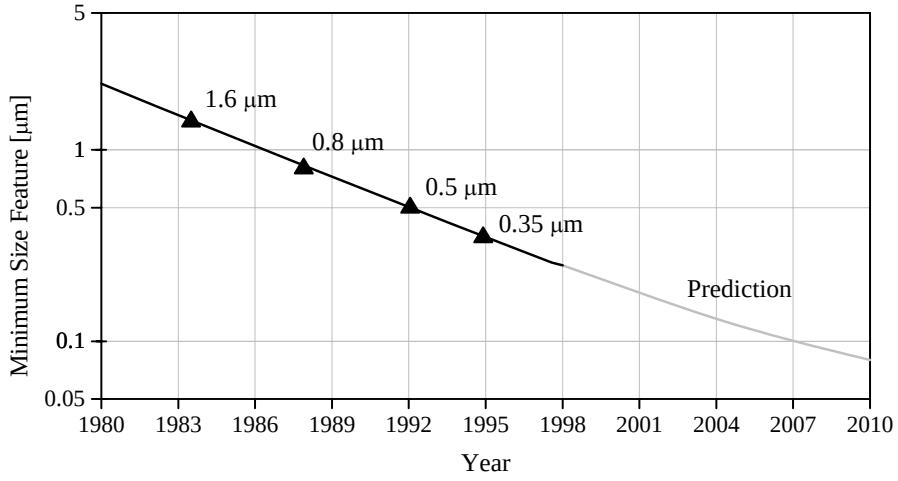

***Figure 1-2**: Moore's Law, predicting the minimum feature size with time [15].*

This continuous downscaling of the devices requires extremely accurate manufacturing of very thin films. Several adverse phenomena, deemed negligible for thicker insulation films, become critical for thinner ones, such as dielectrical breakdown.

The increasing complexity and miniaturisation of modern semiconductor devices as well as economical considerations require higher yields and hence a decreasing density of defects and materials and processes of utmost purity. Impurities are introduced into the semiconductor mainly during device production [2]. It is important to detect contamination sources at an early stage and to prevent further processing of contaminated wafers since the production of modern semiconductor devices involve typically more than 300 process steps: one single material defect or surface contamination can result in a device failure. Therefore, reliable detection methods are required, not only for in-process monitoring of wafers but also to investigate the behaviour of impurities in semiconductors and their impact on device performance.

Metal contamination is the most common impurity due to their good solubility in many chemical solutions used in semiconductor processing, iron is probably the most insidious one. It produces e.g. charge on silicon surfaces [16] and in gate oxides [17, 18] and hence degrades oxide quality. Furthermore, diffusion of surface iron into the bulk during heat treatments greatly affects the minority carrier lifetime [19]. Therefore, many impurity characterisation methods are based on surface charge imaging. Recent techniques for surface charge imaging, all employing SPV, are e.g. the ac-SPV technique [20]; the Surface Charge Analyser (SCA), [21]; the Contaminant Monitoring System (CMS) [22] and surface barrier measurement using the saturation SPV [23]. Techniques probing bulk properties affected by defects include the SPV method for diffusion length measurement [24] and its recent refinement [22] or the photo-conductivity decay by microwave reflection method (μPCD) for minority carrier lifetime measurement [25].

THE SURFACE PHOTOVOLTAGE EFFECT

The detection system investigated in this thesis is based on Kelvin probe CPD measurement extended by steady state (dc) and ac-SPV measurement as well as SPV transient recording.

A characteristic energy band diagram of a Si surface having a thermally grown oxide layer is shown in figure 1-3. The components typically contributing to the total surface charge Q_{SS} are (1) interface trapped charge, Q_{it}, (2) oxide fixed charge, Q_f, (3) oxide mobile charge, Q_m, and (4) oxide trapped charge, Q_{ot}.

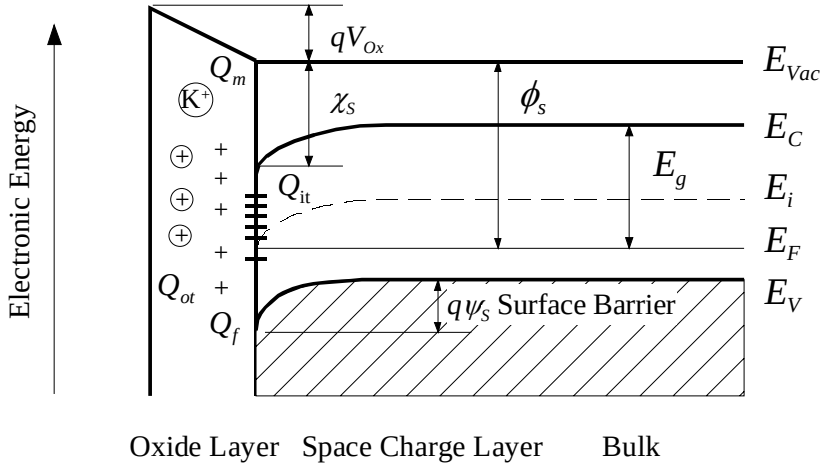

Figure 1-3. *Electronic energy level diagram of a semiconductor surface showing the work function ϕ_S, the electron affinity χ_S and the oxide barrier qV_{Ox} with q being the elementary charge. The surface space charge layer with surface potential $q\psi_S$ is induced by the total surface charge $Q_{SS} = Q_{it} + Q_f + Q_{Ot} + Q_m$. E_F denotes the Fermi energy level, E_i the intrinsic Fermi level and E_C and E_V the energy at the bottom of the conduction band and the top of the valence band, respectively.*

This total surface charge is compensated by an equal but opposite in sign space charge in the semiconductor $Q_{SC} = -Q_{SS}$, which leads to the surface potential barrier $q\psi_S$. The injection of light into this semiconductor creates electron hole pairs which are separated in the surface space charge layer. This induces the surface photovoltage (SPV) and tends to flatten the energy bands at the surface, resulting in a change of the contact

potential difference measured by the Kelvin probe. At high light intensities, where the energy bands at the surface become virtually flat, the SPV saturates and equals the surface barrier height, $q\psi_S$ [26]. This allows to calculate the total charge density at the surface [26].

An example of the SPV effect is shown in figure 1-4. A p-type Si(111) sample was partly coated with Ti ($x > 7$mm). The sample was scanned in darkness and under illumination of a 3mW laser diode ($\lambda = 670$nm). While the work function of the metal surface does not change with light injection, the work function of the semiconductor decreases by approximately 150mV due to the SPV effect.

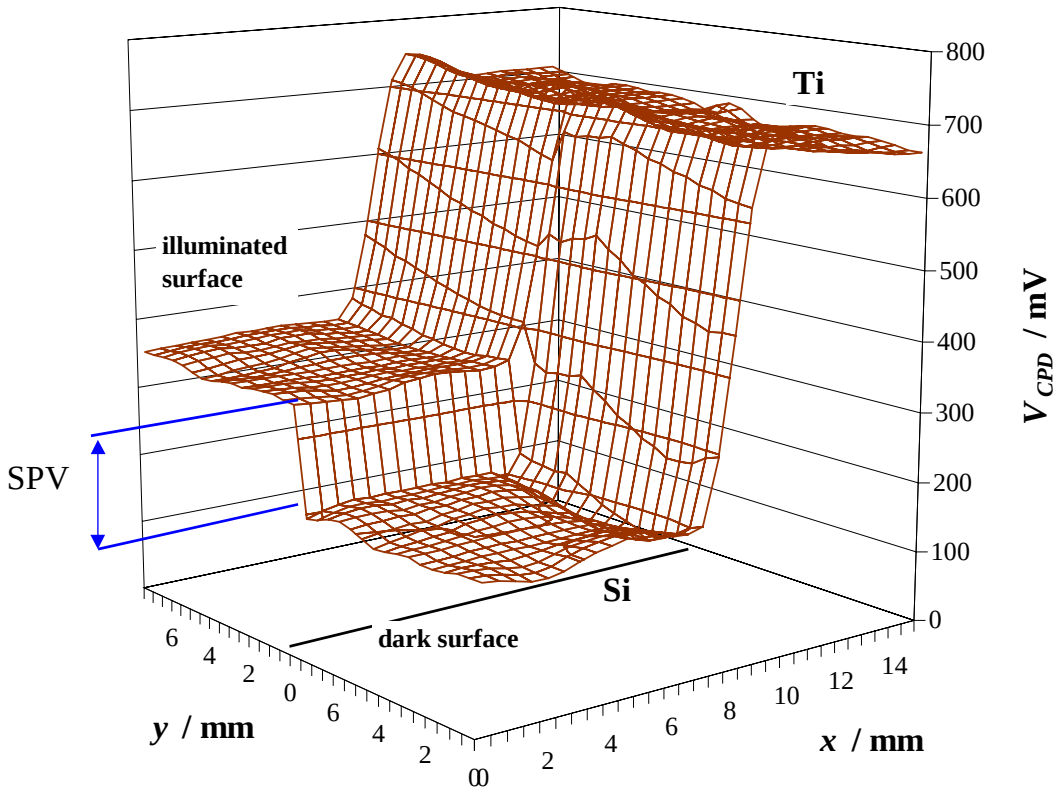

***Figure 1-4**. Illustration of the Surface Photovoltage effect: This CPD topography shows a Ti/Si(111) interface in darkness (foreground scan) and under illumination (background scan). The metal surface experiences no change in work function however, the semiconductor displays a substantial shift in the Fermi level.*

REFERENCES

1. Lord Kelvin, *Philos. Mag.* **46**, 82 (1898).

2. K. Graff, *Metal Impurities in Silicon Device Fabrication*, Springer Series in Materials Science 24, edited by H.J. Queisser, (Springer, Berlin 1995).

3. W.A. Zisman. *Rev. Sci. Instrum.* **3**, 367 (1932).

4. I.D. Baikie, K.O. Vanderwerf, H. Oerbekke, J. Broeze, A. Vansilfhout, *Rev. Sci. Instrum.* **60**, 930 (1989).

5. I.D. Baikie, P.J. Estrup, *Rev. Sci. Instrum.* **69**, 3902 (1998).

6. A. Danon, A. Amirav, *Isr. J. Chem.* **29**, 443 (1989).

7. A. Danon, and A. Amirav, *Int. J. Mass Spectrom. Ion Processes* **96**, 139 (1990).

8. S.Dagan, A. Amirav and T. Fujü, *Int. J. Mass Spectrom. Ion Processes* **151**, 159 (1995).

9. U. Petermann, I.D. Baikie, B. Lägel and K.M. Dirscherl in *Materials Science of Novel Oxide-Based Electronics*, edited by D.S. Ginley, D.M. Newns, H. Kawazoe, A.B. Kozyrev, J.D. Perkins Gossen (Mater. Res. Soc. Proc. **623**, Pittsburgh, PA, 2000) in press.

10. T. Sharhar, S.Dagan, and A. Amirav, *J. Am. Soc.Mass Spectrom.* **9**, 628 (1998).

11. J.C. Rivère in *Solid State Surface Science*, Vol. 1, edited by M. Green (M.Dekker, New York, 1969), p. 198-204.

12. U. Petermann, I.D. Baikie, B. Lägel and K.M. Dirscherl in *Polycrystalline Metal and Magnetic Thin Films*, edited by L. Gignac, O. Thomas, J. MacLaren, B. Clemens (Mater. Res. Soc. Proc. **615**, Pittsburgh, PA, 2000) in press.

13. I.D. Baikie, U. Petermann, A. Speakman, B. Lägel, K.M. Dirscherl, P.J. Estrup, *J. Appl. Phys.* **88**, 1 (2000).

14. Electronic buyers' news online, available [online], http://www.ebnews.com/story/OEG19981210S0003, [24 November 1999]

15. G. Moore, *IEEE Spectrum*, **16**, 79 (1979).

16. P. Roman, I. Kashkoush, R. Novak, E. Kamieniecki and J. Ruzyllo, in *4th International Symposium on Cleaning Technology in Semiconductor Device Manufacturing* (Electrochemical Society Proceedings, **95-20**, 1995) pp. 344-349.

17. F.M. Ross and J.M. Gibson, *Mat. Res. Soc. Proc*., **259**, 87 (1992).

18. H. Shimuzu and C. Munataka, *Appl. Phys. Lett.* **62**, 276 (1993).

19. G. Zoth and W. Bergholz, *J. Appl. Phys.* **67**, 6764 (1990).

20. C. Munakata and S. Nishimatsu, *Japan. J. Appl. Phys.* **23**, 1451 (1984), **25**, 807 (1986).

21. E. Kamieniecki, P. Roman, D. Hwang and J. Ruzyllo in *Proc. Second Intern. Symp. On Ultra-Clean Processing of Silicon Surfaces UCPSS '94*, edited by M. Heyns, M. Meuris and P. Mertens (Acco Leuven / Amersfoort, 1994), pp. 189-192.

22. J. Lagowski, P. Edelman, M. Dexter and W. Henley, *Semicond. Sci. Techn.* **7**, A185 (1992).

23. P. Edelman, J. Lagowski and L. Jastrzebski in *Photo-Induced Space Charge Effect in Semiconductors*, edited by D.D. Nolte, N.M. Haegel and K.W. Gossen (Mater. Res. Soc. Proc. **261**, Pittsburgh, PA, 1992), pp. 223-228.

24. A.M. Goodman, *J. Appl. Phys.* **32**, 2550 (1961).

25. A.P. Ramsa, H. Jacobs and F.A. Brand, *J. Appl. Phys.* **30**, 1054 (1959).

26. E.O. Johnson, *Phys. Rev*. **111**, 153 (1958).

Chapter 2

The Work Function: Fundamentals and Modes of Measurement

2.1 CONCEPT OF THE WORK FUNCTION

The concept of a work function evolved from early experiments of thermionic emission of electrons from hot metal surfaces in vacuum. The equation of the thermionic emission, as discussed in §2.4.2 was derived by Richardson assuming a potential difference of electrons inside and outside a metal surface, thus implicitly using the work function concept [1]. However, the term *'work function'* was only introduced later by Lester who described it as 'The work done by an escaping electron…' [2]. This definition however only applies for the special case of metals and does not state the initial energy state of the electron in the solid nor its energy after escaping the material.

Today, the work function ϕ is commonly defined as the *minimum* energy required to move an electron from a solid to just outside the material at the temperature $T = 0$K. This definition implies that the electron is removed from the highest potentially occupied electronic energy level in the solid, the Fermi level E_F, to an arbitrarily fixed reference level, commonly taken as the vacuum level, E_{Vac}, see figure 2-1.

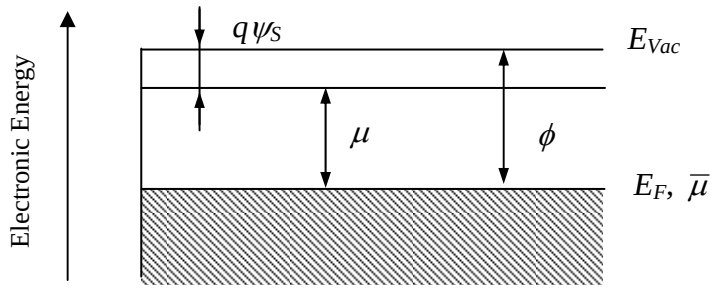

Figure 2-1. *Electronic energy level diagram of a solid showing the various energies relevant to the definition of the work function ϕ as discussed in the text.*

The Fermi energy level is equivalent to the electrochemical potential $\bar{\mu}$ which depends solely upon the material and its temperature and is therefore a bulk property of the solid [3]. However, measurements have shown that the work function depends strongly on the condition of the surface, e.g. on the orientation of single crystal surfaces and on surface adsorbates. This is due to the formation of a dipole layer at the surface, also termed the surface double layer, where the electrical potential across this layer is called the *surface potential* ψ_S. Thus the work function comprises two parts: the chemical potential μ, also referred to as the *inner* work function, which is purely a **bulk** property and the surface potential ψ_S which depends on **surface** condition [4]:

$$\phi = -\left(\mu + q\psi_S\right). \qquad 2\text{-}1$$

From figure 2-2 we find also a correlation of the work function of the elements with its place in the periodic table. The work function typically increases within each period and decreases with the atomic number in a main group of the periodic table.

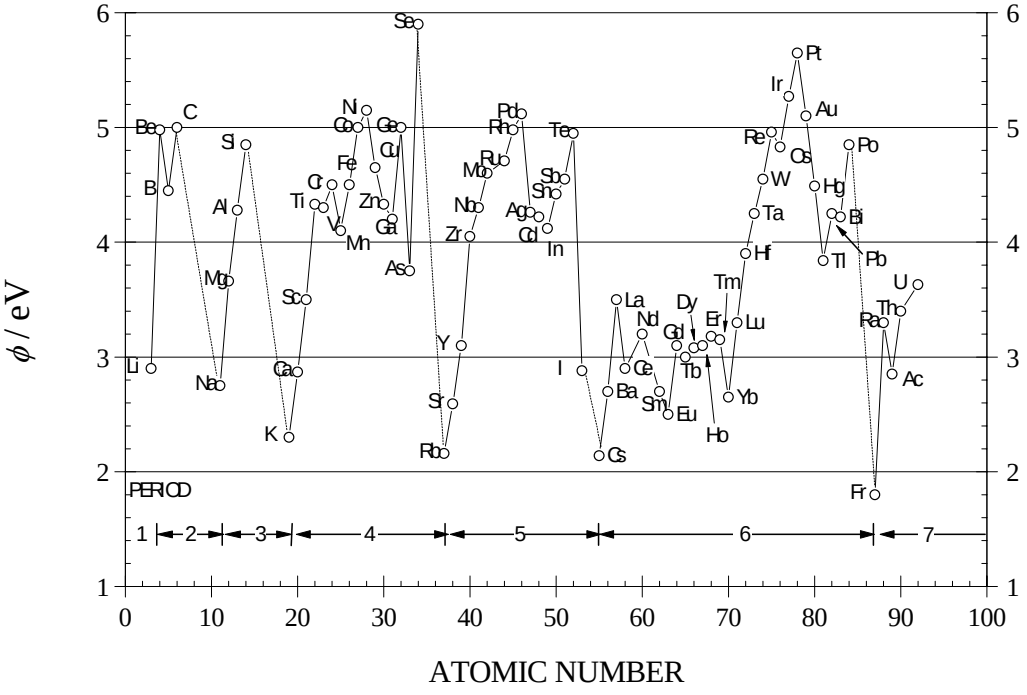

***Figure 2-2**. The work function of clean metal surfaces in vacuum versus the atomic number [5].*

2.2 THE SURFACE DOUBLE LAYER

2.2.1 Dependence of the Work Function on the Crystallographic Orientation

Although electrons in a solid are confined in a potential barrier, the electron wavefunction has a non-zero amplitude 'just outside' the surface, i.e. within approx. 10Å from the surface, decaying exponentially with increasing distance. This probability of an electron to exist outside the surface, also called 'electron overspill', is balanced by the corresponding excess positive charge remaining in the solid thus giving rise to a dipole layer which is termed the surface double layer. The voltage across this layer is the surface potential ψ_S mentioned above. The extend of the electron overspill depends on the electron density at the surface and thus increases with an increasing density of surface atoms. Since this density is a function of the crystallographic plane in a solid, the work function also depends on the crystallographic orientation of the surface [6]. As an example, the surface atom densities and work functions of different tungsten crystal planes are listed in table 2-1.

***Table 2-1**: Surface atom densities and the corresponding work function of different crystallographic planes of tungsten from [7].*

surface index	**atomic density $\times 10^{14}$ / cm^{-2}**	**ϕ / eV**
111	5.77	4.47
100	10.0	4.63
110	14.1	5.25

2.2.2 Work Function Changes Induced by Adsorbates

If the adsorption of atoms or molecules at the surface results in a charge transfer between the adsorbate and the solid, the surface electric double layer will be modified resulting in a change of the surface potential, $\Delta\psi_S$, and hence in a change of the work function. In a first approximation the dipole layer can be modelled as a parallel plate capacitor and hence $\Delta\psi_S$ can be expressed by [8]

$$\Delta\psi_S = \frac{n_{ad}}{\varepsilon_0 \varepsilon_r} \cdot \mathbf{p} \bullet \mathbf{n}, \qquad 2\text{-}2$$

where n_{ad} is the density of molecules adsorbed at the surface, **p** is the dipole moment and **n** the unit normal vector perpendicular to the surface, ε_0 the permittivity of free space and ε_r equals 1. The dipole moment is defined by

$$\vec{p} = \delta q \cdot \vec{r}, \qquad 2\text{-}3$$

where δq is the fractional charge exchanged between the adsorbate and the substrate and the vector $\vec{r}$ is determined by the orientation and length of the bond, see figure 2-3.

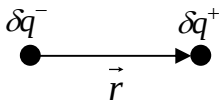

***Figure 2-3**. Definition of the dipole moment $\vec{p}$.*

From equation 2-1 we see that a change in ψ_S is directly related to a change in the work function:

$$\Delta\phi = -\Delta\psi_S. \qquad 2\text{-}4$$

The magnitude and sign of $\Delta\phi$ depends on (i) the electronegativity of the molecules involved and (ii) the orientation of the surface dipoles. For the discussion of (i) we assume that the adsorbate is on top and the dipole orientation perpendicular to the surface as shown in figure 2-4. If the adsorbate has an electronegativity, χ_{ad}, *higher* than that of the substrate, χ_{sub}, it attracts electrons, i.e. the surface potential *decreases* and the work function *increases*, i.e. $\Delta\phi > 0$, see figure 2-4 (b). If, on the other hand, χ_{ad} is *lower* than χ_{sub} the surface potential *increases* and the work function *decreases*: $\Delta\phi < 0$, see figure 2-4 (a). The magnitude of $\Delta\phi$ then depends on the degree of charge transfer between the adsorbate and the surface, i.e. on δq, see equation 2-3.

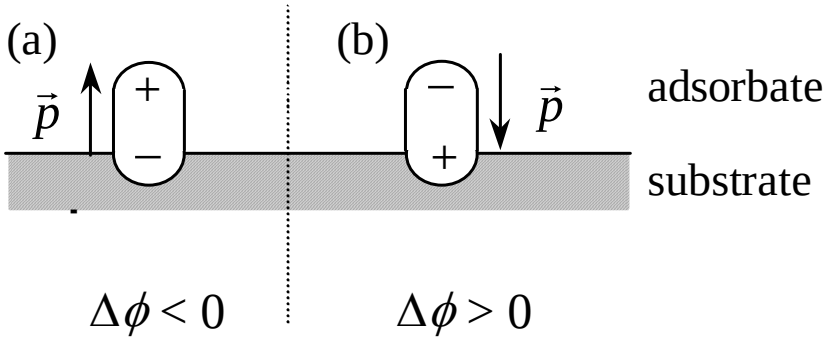

Figure 2-4*. Orientation of adsorbate-induced dipoles and the respective work function change: (a) the adsorbate is polarised with the positive pole towards the vacuum side causing a decrease in ϕ and (b), with the negative pole pointing towards the vacuum side, ϕ increases.*

The effect of the orientation of the dipole with respect to the surface plane of the substrate is expressed by the scalar product $\mathbf{p} \bullet \mathbf{n}$ in equation 2-3. Therefore, only the fraction $p_{\perp} = |\vec{p}| \cdot |\vec{n}| \cdot \cos\alpha$ contributes to $\Delta\phi$ as illustrated in figure 2-5 for the case of a 2-atom bonding, assuming that $\chi_{ad} < \chi_{sub}$. Then, for an angle of e.g. $\alpha = 45^{\circ}$, the contribution to the direction normal to the surface plane is $p_{\perp} = |\vec{p}| \cdot \frac{1}{\sqrt{2}}$.

If the adsorbed molecule is however embedded below the surface, the sign of the dipole moment $p_\perp$ will be reversed. For instance, for a dipole with $\alpha = 225^\circ$, $p_\perp = |\vec{p}| \cdot -\frac{1}{\sqrt{2}}$.

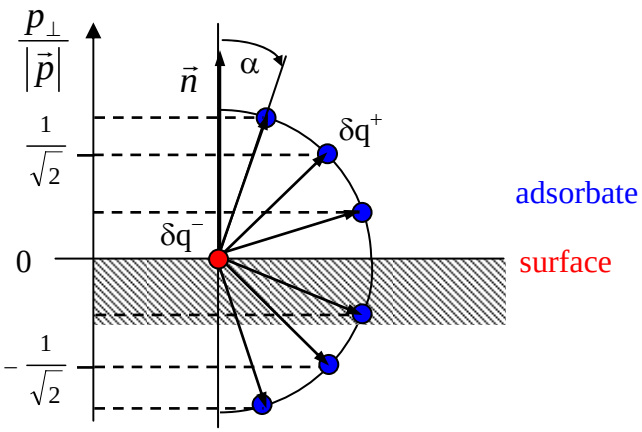

***Figure 2-5**. The fraction of the dipole moment perpendicular to the surface, denoted by $p_\perp$, as a function of the orientation of the dipole with respect to the substrate surface, represented by the unity normal vector $\vec{n}$.*

Similarly, if the adsorbed molecule is bonded to 2 substrate atoms, the magnitude of the dipole is doubled compared to the mono-atomic bond discussed above, as shown in figure 2-6 below.

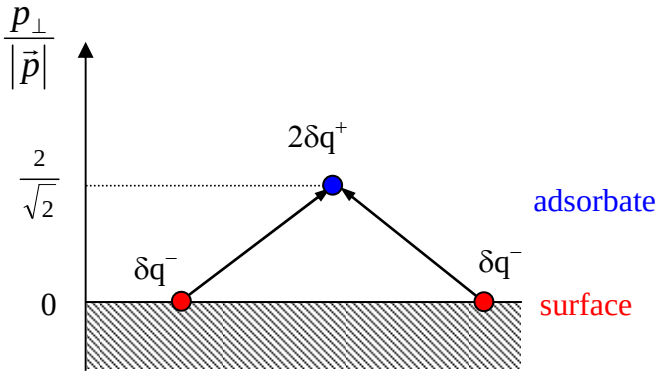

***Figure 2-6**. Dipole contribution to $\Delta\psi_S$ for the case that the adsorbate is bonded to 2 substrate atoms, effectively doubling $\Delta\psi_S$ compared to the mono-atomic case.*

2.3 TEMPERATURE DEPENDENCE OF THE WORK FUNCTION

The temperature dependence of the Fermi level can be approximated by [9]

$$E_F \approx E_{F0}\left[1-\frac{(\pi kT)^2}{12{E_{F0}}^2}\right], \qquad 2\text{-}5$$

where E_{F0} is the Fermi energy at T = 0K. Practically, the change in E_F with temperature is very small. For instance, for metallic sodium, having a Fermi energy of 3.1eV [9], the decrease in E_F is less than 10meV at 2000K according to equation 2-5. However, the temperature dependence of ϕ is often obscured by changes in the surface condition as the specimen is heated, e.g. by changes in surface adsorbates or preferential growth of crystal faces at elevated temperatures.

Further, as the temperature increases, the probability $f(E)$ of an electron to occupy the energy state E in the solid higher than the Fermi level E_F increases. $f(E)$ is given by [9]

$$f(E)=\frac{1}{e^{\frac{E-E_F}{kT}}+1}, \qquad 2\text{-}6$$

where k is Boltzmann's constant and T the absolute temperature. This function is illustrated in figure 2-7.

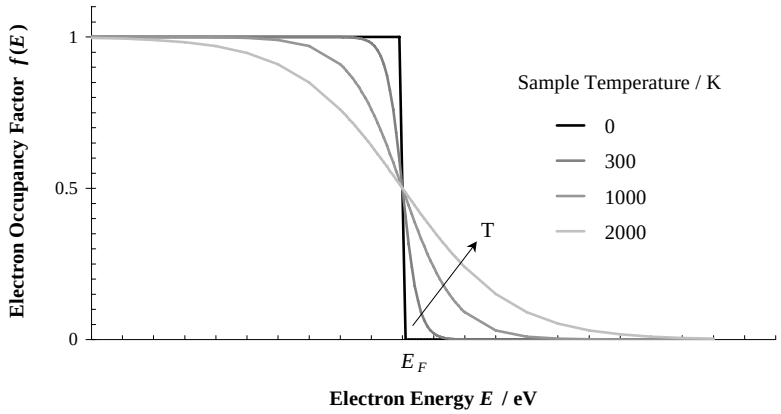

Figure 2-7*. The Fermi-Dirac probability function f(E) for electrons to occupy the energy state E. With increasing temperature T the 'tail' of the function spreads, i.e. more electrons occupy energy levels higher than the Fermi level* E_F.

Therefore, the energy spread of electrons emitted from a specimen at elevated temperatures increases, affecting the results of the 'direct' work function measurement methods that are based on electron emission. For example, the thermal energy spread $2\Delta E = 3kT$ at 2000K is ≈ 0.5eV, see figure 2-8.

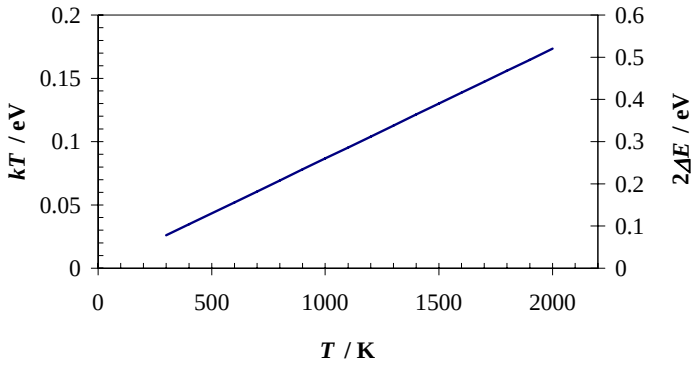

Figure 2-8*. Electrons thermal energy spread with increasing sample temperature.*

Experimentally the work function change $\Delta\phi$ for clean metals was found to be in the order of approximately 10^{-5} to 10^{-4} eV/K, see e.g. table 2-2.

Table 2-2*: Examples of the temperature coefficient of the work function of metals.*

Element	$d\phi/dT$ **/ (eV/K)**	**Reference**
Molybdenum	1.52×10^{-4}	[10]
Tantalum (110)	0.6×10^{-4}	[20]
Nickel	1.5×10^{-4}	
Copper (111)	-0.1×10^{-4}	

In the temperature range we have investigated, from 300K to 1000K, this is less than 0.1eV and hence small compared to $\Delta\phi$ caused by changes in the surface part of the work function $\Delta\psi_S$ due to the adsorption of gases. For instance, $\Delta\phi$ during the oxidation of polycrystalline rhenium at elevated temperatures is up to 2.05eV.

2.4 REVIEW OF WORK FUNCTION MEASUREMENT METHODS

2.4.1 Overview

Experiments to measure the work function can in general be divided into two groups: direct and indirect methods. The first group is based upon

(i) electron emission from the sample surface stimulated either by high temperature (thermionic emission), illumination with light in the visible, UV and X-ray spectrum (photo - emission) or by the application of high electric fields (field - emission) or,

(ii) an electron transfer between the surface and a gas molecule if the molecule is either adsorbed on or in close vicinity of a solid surface.

The second group is based upon the effect of the Contact Potential Difference (CPD) that occurs if two metals of different work functions are brought in electrical contact. Direct methods are used to determine the *absolute* work function of the sample whereas indirect methods typically produce work function data of a sample *relative* to that of a reference electrode.

In spite of the fact that the work function plays a decisive role in all applications requiring electron emission or transfer, the values given for ϕ in a vast number of publications scatter widely, see e.g. table 2-3. This is mainly due to differences in the experimental conditions, e.g. the homogeneity of the sample surface or surface contamination, and the fact that the ϕ values measured depend strongly on the measurement method as will be pointed out in the review of these methods below.

***Table 2-3**: Compilation of photoelectric (P) and thermionic (T) work function data [11] of polycrystalline metals illustrating the wide spread values of ϕ depending on the measurement method and experimental conditions.*

Element	**ϕ / eV (P)**	**ϕ / eV (P)**	**ϕ / eV (T)**
Titanium	4.33 ± 0.10	4.45	3.6-4.3
Molybdenum	4.604.33 ± 0.15	4.3	4.33
Palladium	5.55 ± 0.10	5.5	4.9
Platinum	5.65± 0.10	5.2	5.80

2.4.2 Direct Methods

A. Thermionic Emission

As pointed out in section 2.3, the amount of electrons having energies higher than the Fermi level E_F increases as a metal is heated and some are thus able to escape the metal. A schematic of the diode configuration for measuring this emission current I_{therm} is shown in figure 2-9.

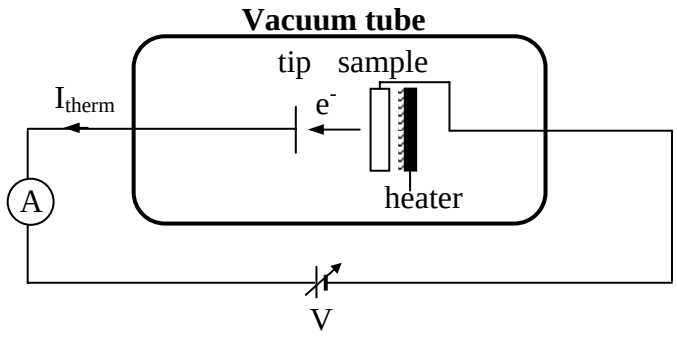

***Figure 2-9**. Schematic of the circuit for work function measurement by thermal emission of electrons (e^-) emitted from the heated sample and collected by the tip.*

The electron current density J_0 under saturation condition, i.e. all emitted electrons are collected, is given by the Richardson-Dushman equation [12, 13]:

$$J_0 = A(1-r)T^2 \cdot \mathrm{e}^{\frac{-\phi}{kT}}, \qquad \textit{2-7}$$

where q is the elementary charge, ϕ and T are the work function and temperature of the sample, respectively, and r denotes the reflection coefficient for electrons upon hitting a metal surface. The constant A, termed the Richardson constant, is equal to $120\frac{\mathrm{A}}{\mathrm{cm}^2\mathrm{K}^2}$ and is related to elemental physical constants by

$$A = 4\pi m_e k^2 \cdot \frac{q}{h^3}. \qquad \textit{2-8}$$

If the saturation current is measured for a series of different temperatures, the slope of the plot of $\ln(J_0/T^2)$ versus $1/T$, termed the Richardson plot, is equal to $-q\phi/k$ and leads to the so called 'Richardson' or 'apparent' work function ϕ^* since the temperature dependence of ϕ can, in general, not be neglected. The intercept of the plot with the $1/T$ axis gives the 'apparent' emission constant A^*. Thus the true work function ϕ is related to ϕ^* by [13]

$$\phi(T) = \phi^* + T\frac{\mathrm{d}\phi}{\mathrm{d}T}. \qquad \textit{2-9}$$

Assuming that $\mathrm{d}\phi/\mathrm{d}T = a$ is constant with T, the Richardson plot yields the work function extrapolated to $T = 0$K. Thus this method relies on the knowledge of a for the specific sample material and the assumption of its independence of temperature which is however not generally true. A selection of experimentally obtained thermionic work function and emission constant data for metals is listed in table 2-4.

***Table 2-4** : Selection of thermionic work function and emission constant data from [3].*

Metal	ϕ^* **/ eV**	A^* / $\frac{\mathrm{A}}{\mathrm{cm}^2\mathrm{K}^2}$
Platinum	5.32	32
Tungsten	4.52	72
Molybdenum	4.37	115
Tantalum	4.1	37

Since the measurement of the saturation current involves the application of relative high accelerating fields between the emitter and the collector electrode, a correction must be introduced to account for the resulting lowering of the potential barrier at the surface which is also known as the SCHOTTKY effect. Further, when studying polycrystalline or inhomogeneous surfaces, patch field effects should be considered. Since the same consideration applies for the photoelectric measurement methods, both effects will be discussed separately in section D – 'Field Emission'.

To obtain measurable electron currents, i.e. typically $I_{therm} > 1\mathrm{nA}$, the sample has to be heated to temperatures of typically >2000K. Therefore, the thermionic measurement method is restricted mainly to high melting point materials such as refractory metals, i.e. it is not generally applicable. Further, for semiconductors, ϕ^* will not produce the sample work function ϕ_S but the energy difference between the vacuum level and the upper level of the valence band, i.e. $\phi^* = E_{vac} - (\chi_S + E_g)$, see figure 2-10.

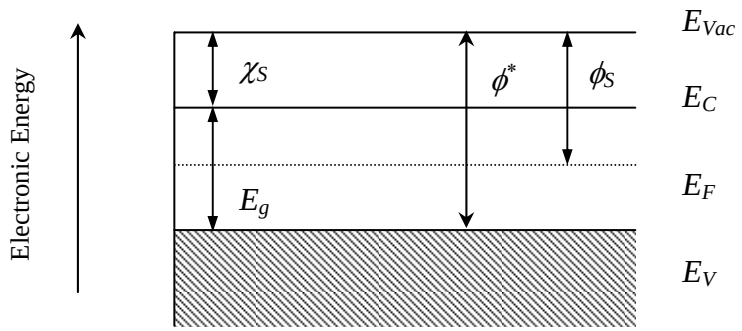

***Figure 2-10**. Simplified electronic energy level diagram of a semiconductor showing the difference between ϕ_S and ϕ^*, the energy obtained by direct electron emission. E_C denotes the bottom of the conduction band, E_V the top of the valence band, E_{gap} the energy difference between E_C and E_V, E_{vac} and E_F denote the vacuum and the Fermi level, respectively, and χ_S is the electron affinity.*

B. Photoelectric Method

If a metal surface with work function ϕ_S is illuminated by monochromatic light of energy $h\nu$ with $h\nu > \phi_S$ (see figure 2-11), the maximum kinetic energy E_{max} of the electrons emitted is given by the Einstein equation [14]

$$E_{\max} = h\nu - \phi_S \,. \qquad 2\text{-}10$$

Therefore, at the threshold frequency ν_0 below which no emission occurs, E_{max} equals zero, i.e.

$$h\nu_0 = \phi_S \,. \qquad 2\text{-}11$$

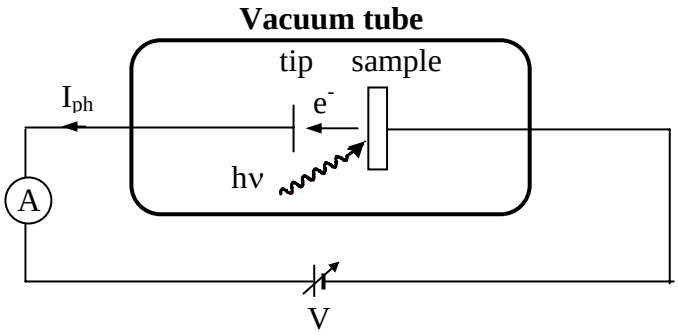

***Figure 2-11**. Schematic of the circuit for observing the photoelectric effect. When monochromatic light of energy $h\nu > \phi_S$ strikes the sample plate photoelectrons (e^-) are ejected and collected by the tip.*

The work function of the emitter (sample) can thus be determined by a measurement of the photocurrent as a function of the photon energy. As pointed out by several authors [15, 16], the photocurrent emitted from a conductor near the threshold is a function of ν given by

$$I_{ph} \propto \left(h\nu - \phi_S\right)^2 . \qquad 2\text{-}12$$

This suggests that ϕ_S can be determined by a linear extrapolation of $I_{ph}^{1/2}$ to zero current provided that the temperature is sufficiently small. For finite temperatures, emission occurring below ϕ will result in deviations from relation 2-12 near threshold and thus errors in the determination of ϕ are of the order of kT. These errors can be avoided by using the expression derived by Fowler [15]:

$$J_0 = B\left(kT^2\right)\cdot f\cdot\left(\frac{h\nu - \phi_S}{kT}\right), \qquad 2\text{-}13$$

where B is a constant independent of T and ν and the function f(x) is given in [15]. To determine the work function of the sample ϕ_S, a so called Fowler plot is made by plotting $\log(J_0/T^2)$ versus $h\nu/kT$. The horizontal shift necessary to fit this curve to the curve $\log f$(x) yields the work function ϕ while the vertical shift determines the constant B. A similar method to determine ϕ_S was introduced by DuBridge where J_0 is measured as a function of the temperature T [17].

As pointed out in section A –'Thermionic Emission' – electrons in semiconductors are emitted from the top of the valence band and hence these methods do not yield the work function ϕ.

C. Effects of External Accelerating Fields on the Measured Work Function

Since absolute work function methods are based on the physical emission of electrons from the surface, any electrical fields present in the vicinity of the surface will affect the emission properties.

A lowering of the potential barrier and hence the *effective* work function ϕ_{eff} at the surface, the so called 'Schottky' effect, results from a superposition of the image potential energy (figure 2-12, a) with the potential energy curve when an external electrical field E is applied (figure 2-12, b). The total potential energy (PE), see figure 2-12 (c), is given by [18]

$$\mathrm{PE}(x) = \frac{q^2}{16\pi\varepsilon_0 x} + qEx \qquad \textit{2-14}$$

The barrier lowering $\Delta\phi$ is obtained at the maximum of the PE curve, i.e. where d[PE(x)]/dx = 0, at the distance x_m from the surface. $\Delta\phi$ is thus given by

$$\Delta\phi = \sqrt{\frac{qE}{4\pi\varepsilon_0}} \qquad \textit{2-15}$$

and x_m by

$$x_m = \sqrt{\frac{q}{16\pi\varepsilon_0 E}}\,. \qquad \textit{2-16}$$

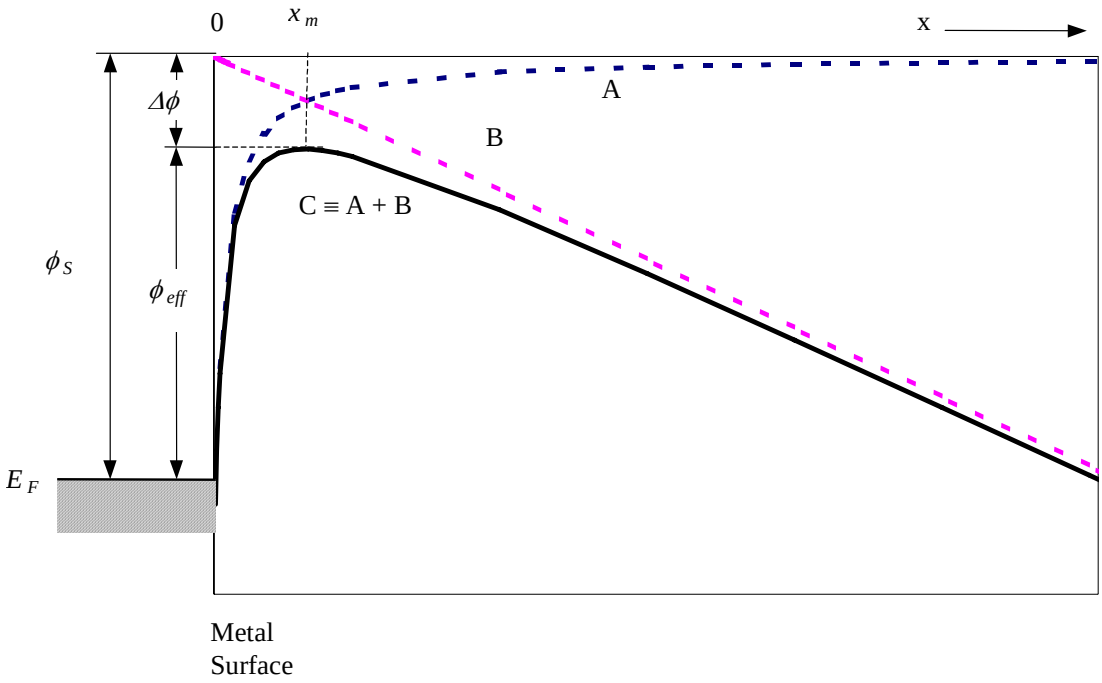

***Figure 2-12**. The potential energy curves at a metal surface with work function ϕ_S: (A) the image potential curve, (B) the potential curve due to the applied electrical field and (C) the total potential energy curve showing the effective work function ϕ_{eff} due to the combined effects of the field and image force.*

The effects of electron emission from patchy work function surfaces, i.e polycrystalline or otherwise inhomogeneous surfaces, has been discussed by Herring and Nichols for the case of thermionic emission for two limiting cases [3]:

(i) In case of a strong external field (x_m << patch dimensions) each patch emits according to its individual work function. Therefore the work function measured for the whole surface is governed mainly by *low* ϕ patches which have the most intensive emission.

(ii) In case of a weak external field (x_m >> patch dimensions), patches with $\phi_i \le \bar{\phi}$, where $\bar{\phi}$ is the average work function of the surface, emit as a single patch of work function $\phi = \sum_i f_i \phi_i$ where f_i is the fractional area occupied by the i^{th}

patch and ϕ_i its work function and electrons emitted from these patches must overcome the potential barrier of $\overline{\phi}$. Patches with $\phi_i > \overline{\phi}$ emit according to their individual work function. Therefore, the measured work function will be $\geq \overline{\phi}$.

The effect of patches on the work function determined by the photoelectric effect is similar to that in the thermionic case [19].

D. Field Emission

If strong accelerating fields are applied to a metal surface electron current densities are observed much larger than expected from a simple Schottky lowering of the surface barrier. This effect was explained by Fowler and Nordheim by a tunnelling of electrons through the barrier since the thickness of the potential barrier *z* can become very small, see figure 2-13.

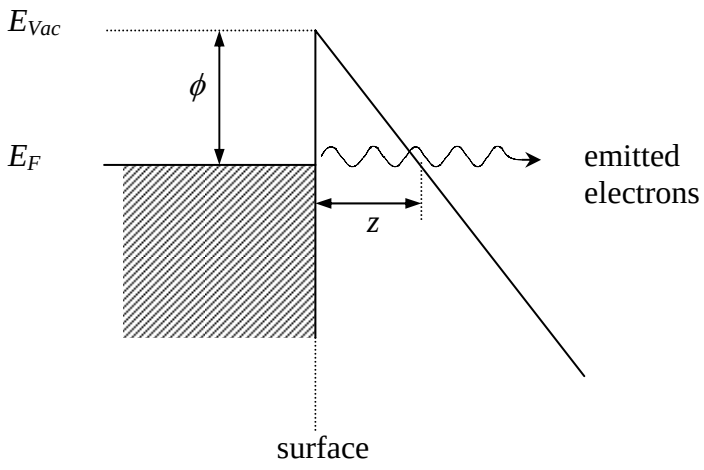

Figure 2-13*. The potential energy for an electron at a metal surface where the electric field is sufficiently large to lower the thickness of the potential barrier z such as to allow electrons to tunnel through the barrier.*

Although a theoretical treatment relates the measured electron current density to the work function of the surface [19], the work function measured, also called the

'effective' work function, is heavily biased towards low ϕ patches and needs to be corrected for the field induced Schottky-type lowering of ϕ. Further, the method suffers from inherent inaccuracies in determining the exact electrical field and field distribution at the emitter tip which is necessary to determine ϕ [19].

E. Surface Ionisation

If an elemental gas is in thermal equilibrium with a solid surface at temperature T, a certain portion α of the gas will be ionised, see figure 2-14, depending on the ionisation potential of the gas I_g and its electron affinity χ_g with respect to the work function of the sample surface ϕ_S. For a high ϕ_S electron transfer from the gas molecules to the surface will prevail, leading to positive surface ionisation (pSI) whereas for a low ϕ_S electron transfer to the gas molecules is the dominant process, leading to negative surface ionisation (nSI). For pSI, the ratio $\alpha_+ = n_+/n_0$ of the density of positive ions n_+ to the density of neutral atoms n_0 can be expressed by the approximation given below as [13]:

$$\alpha_+ = C_+ \cdot \mathrm{e}^{\frac{\phi_S - I_g}{kT}}, \qquad \textit{2-17}$$

where C_+ is composed of several other physical quantities. Analogous, for nSI, the ratio $\alpha_- = n_-/n_0$ of the density of negative ions n_- to the density of neutral atoms n_0 can be expressed by the approximation [13]:

$$\alpha_- = C_- \cdot \mathrm{e}^{\frac{\chi_g - \phi_S}{kT}}. \qquad \textit{2-18}$$

To determine ϕ_S a plot of $\ln(\alpha_\pm)$ versus $1/T$ is made where a straight line would have a slope $q(\phi_S - I_g)/k$ and $q(\chi_S - \phi_S)/k$, respectively, and the intercept $\ln(C_\pm)$ at $1/T = 0$.

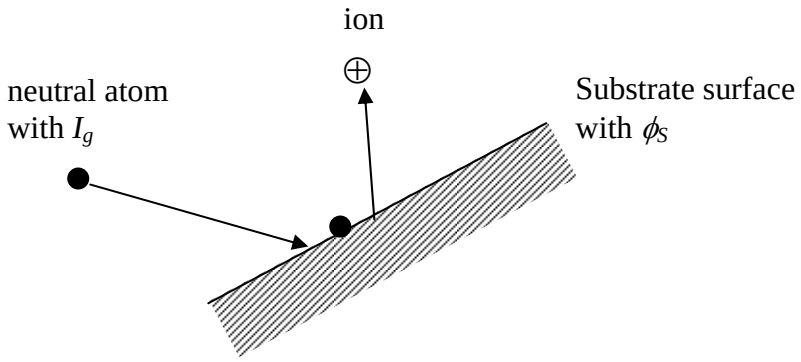

Figure 2-14*. Schematic of the surface positive ionisation process.*

2.4.3 Indirect Methods

A. The Contact Potential Difference

As mentioned above, all relative methods are based on the effect of the Contact Potential Difference (CPD, V_{CPD}). If an external electrical contact is made between the two electrodes their Fermi levels equalise and the resulting flow of electrons from the metal with the lower work function produces a contact potential difference, V_{CPD}, between the plates, see figure 2-15 (b)

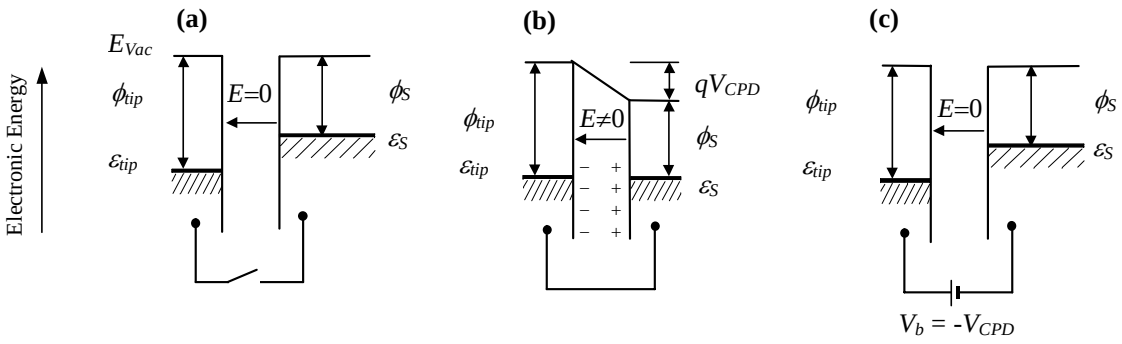

Figure 2-15*. Electron energy level diagrams of two different metals (a) without contact, (b) with external electrical contact, where E indicates the electrical field between the plates, and (c) with inclusion of the backing potential V_b. ε_{tip} and ε_S refer to the Fermi levels of the tip and sample, respectively.*

Therefore V_{CPD} is given by:

$$qV_{CPD} = \phi_S - \phi_{tip}\,, \qquad 2\text{-}19$$

where q is the electronic charge and ϕ_{tip} and ϕ_S are the work functions of the tip and sample, respectively. Work function data of a sample can therefore be obtained *relative* to that of the reference electrode. Measurements of the CPD can be made in either a diode or a capacitor configuration [20].

B. The Diode Method

In the diode method the electron current density J is measured as a function of the applied bias voltage V_b between the anode and an electron emitting cathode, typically via thermionic emission. The total diode voltage is thus the sum of the applied bias voltage and the contact potential difference. A change in the anode work function, $\Delta\phi$, changes the CPD and hence causes a parallel displacement ΔV of the characteristic curve of the diode as shown in figure 2-16.

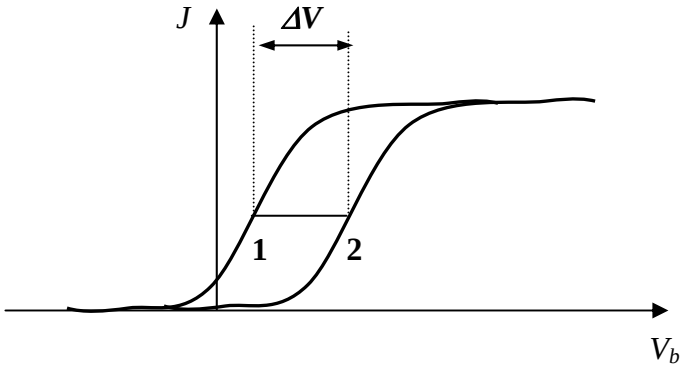

Figure 2-16*. Displacement of the J-V_b characteristic of the diode due to change in the anode work function $\Delta\phi = \phi_2 - \phi_1$ where $\phi_1 < \phi_2$ and $q\Delta V = \Delta\phi$.*

Since the cathode work function is not related to the height of the potential barrier, it has basically no effect on the anode current. The same considerations with respect to polycrystalline or otherwise patchy anode surfaces apply as discussed above. If the

electrons are emitted via field or photo emission, it is also possible to obtain the absolute work function of the anode [20]. This asset of this method was utilised to determine the work function of the reference electrode of the Kelvin probe tip via photoemission from a low work function surface as described in chapter 3.

C. Condenser Methods

This group of methods is based solely on the effect of the contact potential difference and has significant advantages over the direct measurement methods outlined above. For instance, since electrons are neither directly emitted nor collected, the condition of the specimen surface is not altered in any way. Further, the CPD determined with these methods is the *average* work function difference of the specimens and not biased towards low work function patches [19, 21]. Also, the CPD is truly related to the Fermi level of semiconductors as opposed to the direct methods where electrons are emitted either from the valence band or surface states and the theories of emission outlined in section 2.4.2 are either more complicated or not applicable at all [13, 19].

Therefore the range of applications is far wider than for the other methods with respect to the materials to be examined, temperature range and the measurement environment. The most widely used method in this group is the Kelvin method utilising a vibrating capacitor arrangement. Since this is the main measurement method this thesis is based on, it will be discussed separately in section 2.5 – ‘The Kelvin Method’.

2.5 THE KELVIN METHOD

The Scottish scientist Lord Kelvin first postulated the so called 'Kelvin method' just over a century ago [22]. Zisman further developed it in the 1930's into the familiar ac-method used nowadays [23]. Difficulties with UHV compatibility, stability and noise problems have caused its unpopularity in the mid 60's. However, technological progress and innovative materials resulted in its recent comeback.

The basic electrical circuit of the Kelvin probe is shown in figure 2-17. The probe consists of a flat circular electrode (reference electrode, tip) suspended above and parallel to a stationary electrode (the specimen, S) separated at a distance d_0, thus creating a simple capacitor.

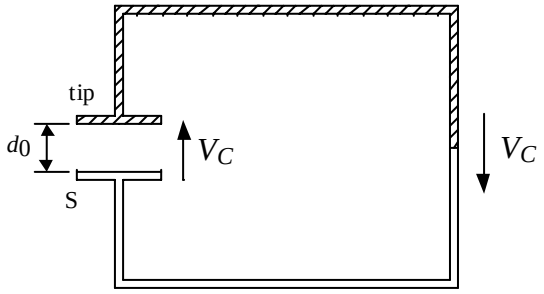

Figure 2-17*. Basic electrical circuit of the Kelvin probe.*

This Kelvin capacitor can thus be described by the equation for an ideal parallel plate capacitor:

$$C_K = \frac{\varepsilon_0 \varepsilon_r A}{d_0} \qquad \textit{2-20,}$$

where C_K is the capacity of the arrangement, ε_0 is the permittivity and A is the area of the capacitor plates. The dielectric constant ε_r is assumed to be equal to 1 for measurements in air or vacuum.

The capacity of the arrangement is related to the electrical charge at the plates Q and the voltage across the capacitor V_C by

$$C_K = \frac{Q}{V_C}. \qquad 2\text{-}21$$

By vibrating the probe, a varying capacitance is produced:

$$C_K(t) = \frac{C_0}{1 + \beta \cos(\omega t)} \qquad 2\text{-}22$$

where β is the modulation index given by

$$\beta = \frac{d_1}{d_0}, \qquad 2\text{-}23$$

with d_0 being the mean spacing between the sample and the probe tip and d_1 the amplitude of oscillation of the probe This periodic Kelvin capacity causes a flow of charge Q back and forth between the plates, which can be described as an alternating current $I(t)$ with the following equation:

$$I(t) = \frac{dQ}{dt} \qquad 2\text{-}24$$

and with equation 2-21 by

$$I(t) = V_C \cdot \frac{dC_K}{dt}. \qquad 2\text{-}25$$

Inclusion of a variable 'backing potential' V_b in the external circuit permits biasing of one electrode with respect to the other. Hence, the voltage across the Kelvin capacitor V_C can be expressed by

$$V_C = V_{CPD} + V_b. \qquad 2\text{-}26$$

At a unique point, where $V_b = -V_{CPD}$, the voltage across the capacitor equals zero and the electrical field between the plate vanishes, see figure 2-15 (c). Under this condition, according to equation 2-25, the amplitude of the output signal is equal to zero. The work function difference between the electrodes is thus equal and opposite to the dc-potential necessary to produce a zero output signal.

2.6 TECHNICAL REALISATION OF THE KELVIN PROBE

2.6.1 Principle of the Measurement

The method explained above suggests to determine the unique point, where $V_b = -V_{CPD}$ in order to measure V_{CPD}. The contact potential difference in this null output condition has conventionally been determined by using a lock-in-amplifier (LIA) with proportional [24, 25] or integral [26, 27] feedback. However, this measurement method works in the disadvantageous region of the balance point where the signal-to-noise (S/N) ratio reaches a minimum and noise, especially overtalk from the driving coil creates an offset [28, 29]. Moreover, the proportional feedback comprises an error signal which is a function of both mean spacing d_0 and amplitude d_1 of the oscillation of the Kelvin probe [28, 30].

To avoid these sources of erroneous measurement results, the Kelvin probe that was used here incorporates advanced ‘off null’ detection, where the balance point is determined by linear extrapolation rather than nulling with a resolution of <1mV. This system also includes automatic control of the tip-to-sample spacing, which is an important requirement for accurate measurements [31]. In this mode, the probe tip is connected to a low noise operational amplifier (op-amp), acting as a current-to-voltage converter as shown in the schematic circuit diagram in figure 2-18.

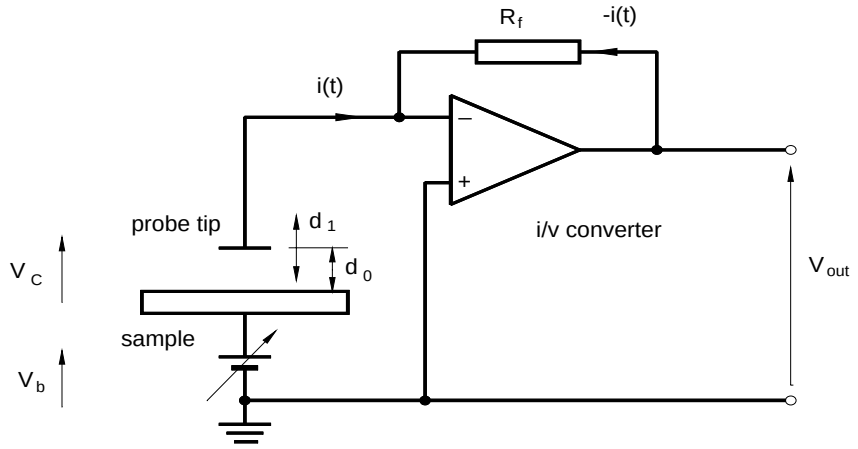

***Figure 2-18**. Electronic circuit diagram of the Kelvin probe input stage. R_f is the I-V converter feedback resistance, d_0 is the mean spacing between the sample and the probe tip and d_1 is the amplitude of oscillation of the probe.*

For small β, i.e. $\beta < 0.3$, the output voltage *V(t)*, see figure 2-19, can be given by [32]:

$$V(t) = (V_{CPD} - V_b) R_f C_0 \omega \beta \sin(\omega t + \varphi), \qquad 2\text{-}27$$

where V_{CPD} represents the voltage difference between probe tip and sample, V_b is the externally applied bias voltage used to balance (or null) the circuit, C_0 is the mean Kelvin probe capacitance, ω the angular frequency of vibration and φ the phase angle.

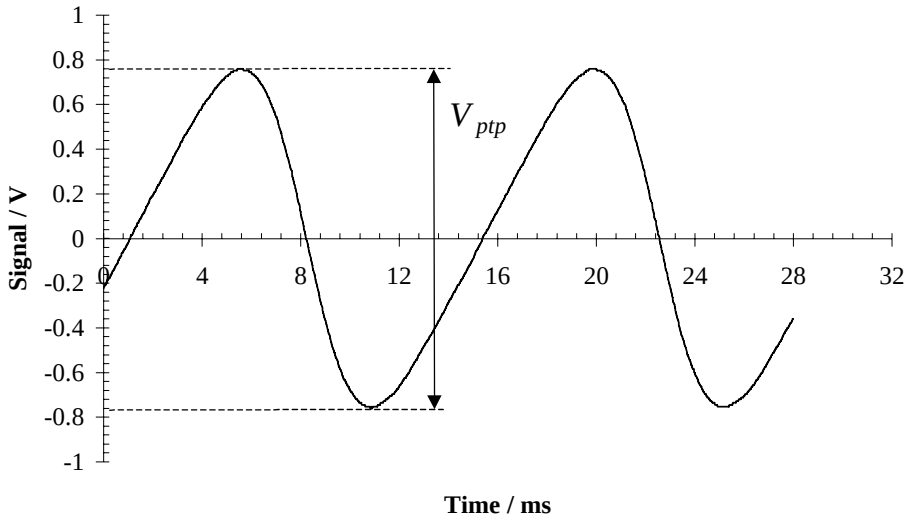

***Figure 2-19**. Typical output signal of the Kelvin probe where V_{ptp} denotes the peak-to peak voltage of the signal.*

In order to determine the condition where $V_b = -V_{CPD}$, the backing potential V_b is set to a range of potentials and a plot of V_{ptp} versus V_b is made as shown in figure 2-20. The output is linear of the form

$$V_{ptp} = mV_b + c\,, \qquad 2\text{-}28$$

where m is the gradient and c the intersect of the curve with the y-axis. The intersection of the least square fit of the data with the x-axis, i.e. where $V_{ptp} = 0$, thus equals the contact potential difference $V_{CPD.}$ For practical measurements, it is sufficient to set the backing potential to just 2 values, typically to +5V and –5V.

Curves (b) and (c) in figure 2-20 were measured on aluminium and gold, respectively, resulting in a shift of the curve along the x-axis. This shift equals the difference in the work function of these surfaces, $\Delta\phi$.

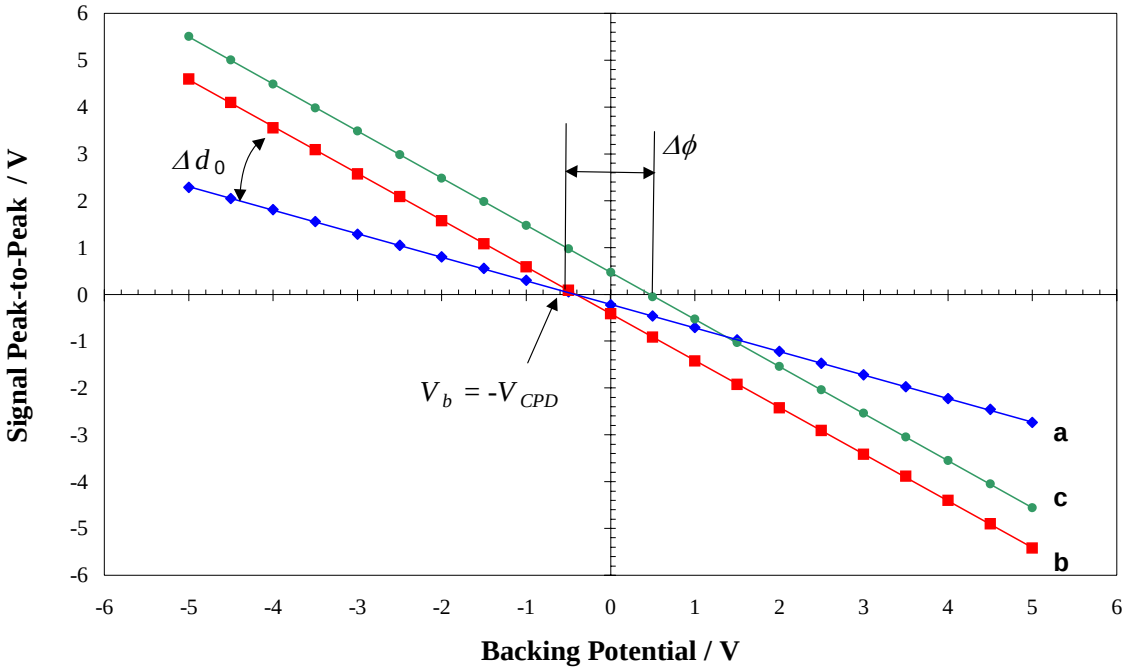

***Figure 2-20**. Schematic diagram showing (a) the variation of the peak-to-peak output signal V_{ptp} with backing potential V_b. Curve (b) shows the effect of an increase in mean spacing d_0 and (c) the change in the contact potential difference, V_{CPD}.*

Also shown in figure 2-20 is the effect of a change in the mean spacing d_0 via curves (a) and (c), resulting in a change of the gradient of these curves, see equations 2-27 and 2-28. Therefore, the gradient of the V_{ptp} versus V_b data provides a direct indication of the sample to tip spacing d_0, where the gradient is proportional to d_0^{-2} [33]. This parameter can therefore be used to keep the mean spacing d_0 of the capacitor constant during scanning operation via a feedback loop.

2.6.2 Instrumentation

A. Overview

An overview of the ambient version of the scanning probe arrangement is shown in figure 2-21. The host PC controls 3 subsystems: the digital oscillator (DO) which sets the voice coil frequency, amplitude and signal trigger, the data acquisition system (PCI 1200, National Instruments) which acquires the Kelvin probe signal and sets the backing potential V_b via a 12-bit digital-to-analogue converter (DAC) and the sample translation stage.

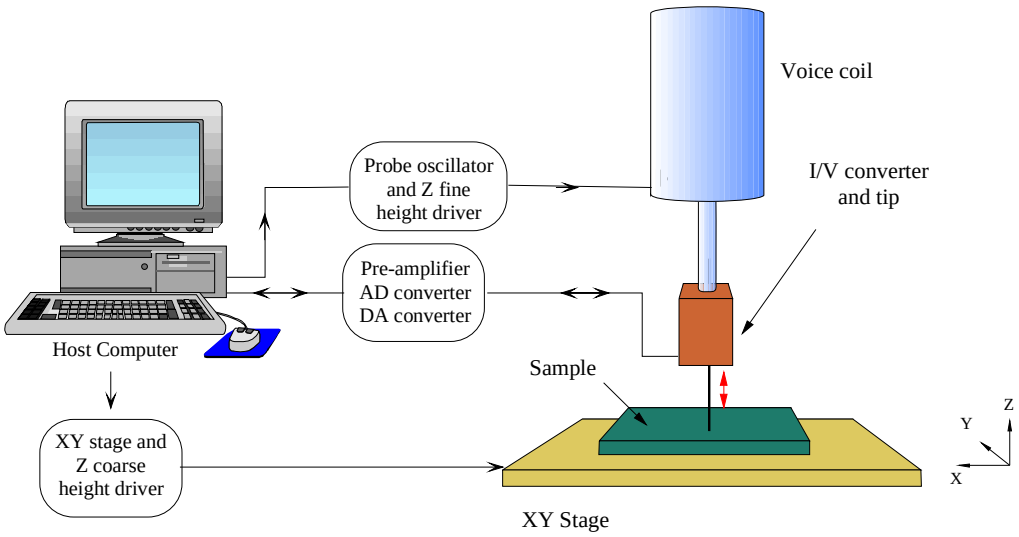

***Figure 2-21**. The scanning Kelvin probe system (ambient version).*

For the ambient version of the probe the probe tip is directly mounted onto the I-V converter. The backing potential can be applied to either the sample or the tip. The trigger signal is used to synchronise the data acquisition so that signal averaging can be performed. This trigger is set by a variable delay from the digital oscillator in order to acquire the relevant part of the signal to obtain V_{ptp}. Application of a dc-offset to the voice coil permits vertical probe positioning with high accuracy (40nm). In the following sections the 3 main components of the Kelvin probe, the voice coil driver, the digital oscillator and the amplifier will be discussed in more detail.

B. Voice-Coil Head Unit

The head stage, see figure 2-22, contains the voice coil driver element, SmCo permanent magnets (Dexter Magnetic Corp.) attached to a stainless steel tube which is suspended by two stainless steel diaphragm springs (∅ = 25.4mm). The springs have a laser cut "meander" pattern allowing a large amplitude of vibration and flexibility along the axis of vibration with a high rigidity to off-axis displacements [28, 32, 34].

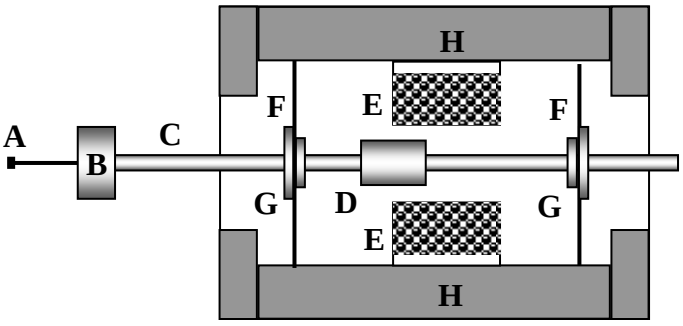

Figure 2-22*. Cross sectional view of the voice coil head unit: (A) the probe tip, (B) I-V converter (ambient version only), (C) shaft, (D) SmCo magnets, (E) coil, (F) diaphragm springs, (G) spring clamps, (H) housing.*

The configuration of the ambient probe differs somewhat from the UHV version due to the different requirements. For the ambient probe the tip is mounted directly onto the input of the low noise I-V converter (OPA 111, BURR BROWN) via a clamp for rapid

tip exchange. Depending on the requirements for the spatial resolution, tip diameters from 5mm down to 50μm were used.

For the UHV compatible version, the suspension system is incorporated into a UHV bellow and manipulator arrangement, which allows a 50 mm travel for the mean spacing variation between tip and sample. A 3mm diameter stainless steel tip is mounted to the central shaft via an insulator as shown in figure 2-23. A spiral wire is attached to the tip forming the electrical contact to the external preamplifier via a UHV electrical feedtrough.

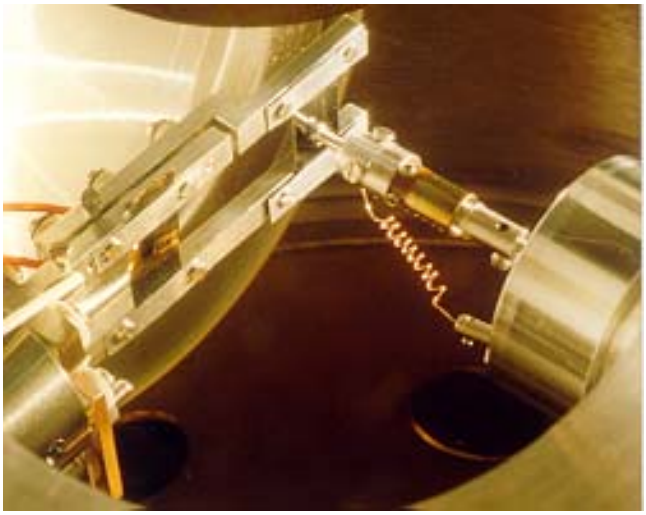

Figure 2-23*. Photograph of the Scanning Kelvin Probe mounted on the UHV system. The tip of the probe is shown in front of a Si sample.*

C. Digital Oscillator

The oscillator allows digital control of the frequency and amplitude of the probe vibration, signal triggering and, in conjunction with the 12-bit DAC output of the PC1200 data acquisition board, the dc-offset level. The oscillation frequency is synthesised from a 4 MHz clock signal. This signal is divided by a programmable divider, the output of which is fed into a counter, producing the desired variable frequency clock. A comparator, armed with a user selectable integer value generates an

output pulse at the respective point in the wave form which is used as an external trigger output. This allows signal averaging via “boxcar” integration [35].

An erasable programmable read-only memory (EPROM) storing 256 values of a digitised sine wave is read at the frequency of the counter and this output is converted to an analogue signal by the onboard DAC. A second DAC on the PC-1200 DAS is used to add a dc-offset to the ac waveform which allows to move the tip either toward or away from the sample. Last, a dc power amplifier outputs the signal to the voice coil. The oscillator is capable of setting the frequency of the vibration in a range from 10 Hz to 300 Hz within steps of 0.2 Hz and the amplitude of the oscillation within 0.5% of the maximum.

D. Pre-Amplifier

The pre-amplifier, see figure 2-24, being the input stage of the Kelvin probe circuit, is an important part of the probe instrumentation and has been thoroughly investigated [32]. Due to the low currents involved, typically <10nA, a low noise, low bias current op-amp type (OPA111, BURR BROWN) is used for the I-V converter having a gain of $10^7 VA^{-1}$. A further differential amplifier stage eliminates the voltage offset if the backing potential is applied to the input stage.

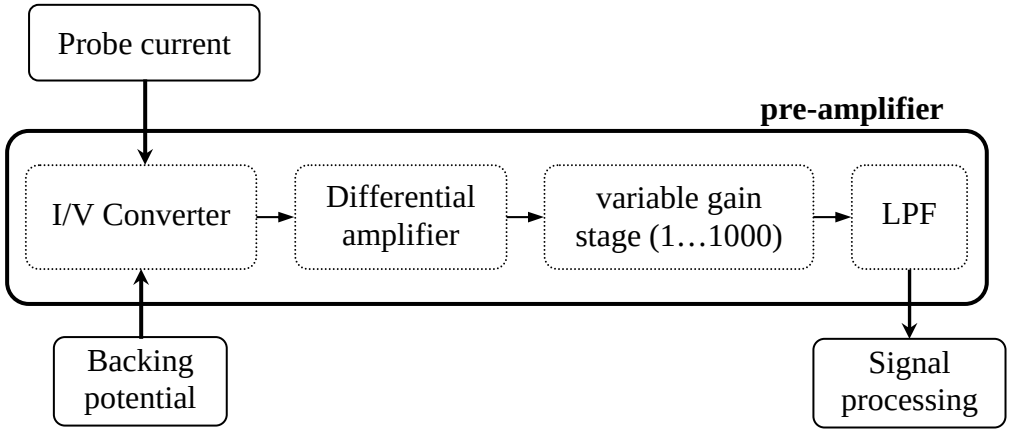

Figure 2-24*. Schematic of the pre-amplifier with its external connections.*

The variable gain stage allows further amplification of the signal up to 1000 times. The low pass filter (LPF), having a cutoff frequency of 800Hz, limits the high frequency noise and hence increases the signal-to-noise ratio. The output of the pre-amplifier is finally fed into the AD converter of the data acquisition card where the digitised signal is processed by the software program of the host computer.

2.6.3 Software Development

The software to operate the Kelvin probe was written for the 32-bit Microsoft® Windows™ operating system environment in the object orientated programming language Borland® Delphi™. A block diagram of the program is presented in figure 2-25.

Initially all the measurement parameters are input. Then the backing potential V_b is set via the DAC of the data acquisition card. The signal acquisition is initiated by the externally applied trigger. The data is then transferred and stored from the DAS to an internal array in the PC's memory and the program proceeds with the next acquisition. The second array is added to the first for the required number of averaging loops 'n'. This method (boxcar integration) effectively reduces noise. The program then calculates all the necessary parameters, such as V_{ptp}, V_{CPD} and the gradient m of the V_{ptp} versus V_b plot which is used as a measure of the tip to sample spacing, see section 2.6.1.

In the so called 'tracking' mode, the actual gradient is compared with the required gradient set by the user and, if necessary, the tip-to sample distance will be adjusted via a voice coil dc-offset or z-axis movement of the scanning stage to achieve the requested gradient within predefined margins. For this, a new dynamic tracking mode was implemented that reduces the time to reach the desired gradient [36].

Additionally, safety procedures were implemented to prevent damage of the probe and sample in cases of tip-sample contacts or faulty electrical connections.

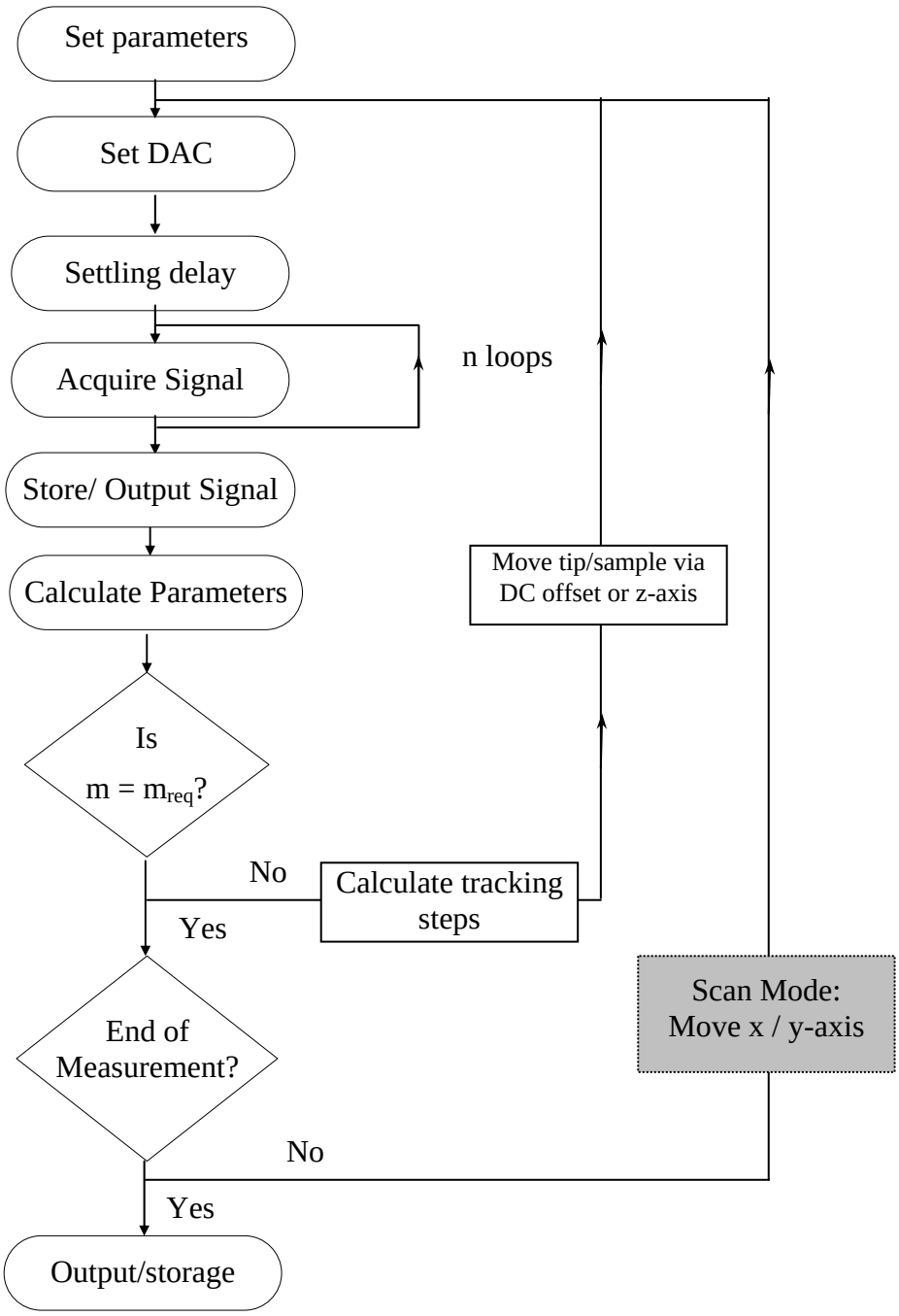

***Figure 2-25**. Main Kelvin probe measurement loop.*

The parameters of the current measurement point are displayed and stored as required. If the scanning option is activated, the sample is moved to the next position and the above measurement routine is repeated until the scan is finished or the user stops the measurement.

(a)

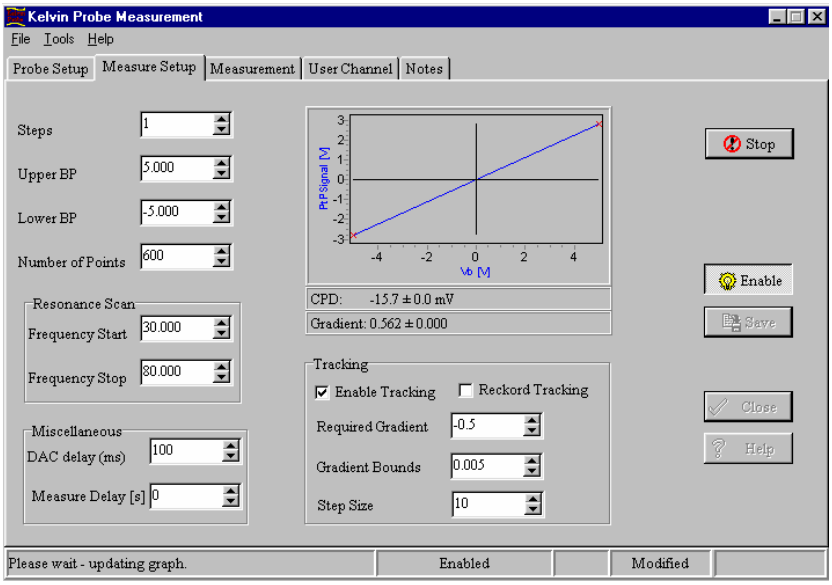

(b)

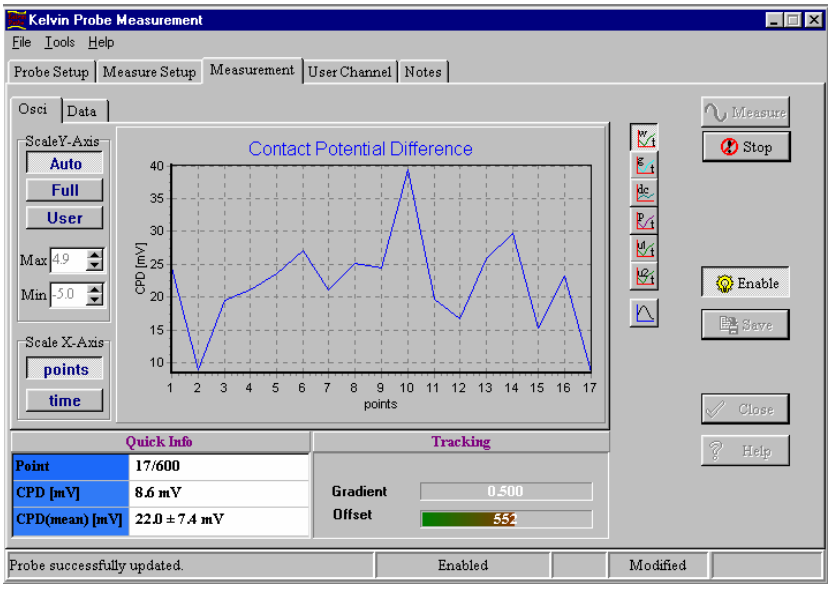

***Figure 2-26**. Screenshots of the Kelvin probe measurement program showing (a) the measurement setup page with the V_{ptp} vs. V_b plot using the currently set parameters and (b) the recording of the CPD change over time.*

The final data set can be stored either as a text based file or, via the clipboard tool, directly inserted into other Microsoft® Windows™ based applications. Further, the data can be directly transferred and saved into the spreadsheet program Microsoft® Excel™ using Object Linking and Embedding (OLE) automation [37]. Post processing and data display can be performed via a customised Excel 'Add-In' program written in the macro language 'Visual Basic for Applications'. This design thus provides a user-friendly application interface, see figure 26, and allows a high degree of flexibility using state of the art software programming technology.

2.7 FINAL COMMENTS

This chapter is intended to give a general view of existing methods for the work function determination. The main measurement method that was utilised for the research projects reported in this thesis is the Kelvin probe technique used to determine differences or changes in the work function of the specimens. Results of these measurements are given in chapters 4 and 6.

A combination of the Kelvin probe and the photoelectric effect method has been developed to determine the *absolute* work function of the specimen and thereby utilising the advantages of both methods. This novel technique is discussed in detail in chapter 3.

Further, the ion source for a novel mass spectrometer technique investigated in this thesis is based on the effect of Hyperthermal Surface Ionisation (HSI) that is closely related to the surface ionisation effect reviewed in this chapter. HSI is discussed in more detail in chapter 5.

REFERENCES

1. O. W. Richardson, *Proc. Camb. Phil. Soc.* 286 (1901).

2. H.H. Lester, *Phil. Mag.* **31**, 197 (1916).

3. C. Herring, M.H. Nichols, *Rev. Mod. Phys.* **21**, 187 (1949).

4. P.M. Gundry, F.C. Tompkins, in *Experimental Methods in Analytical Research*, edited by R. Anderson (Academic Press, 1968), p. 113-116.

5. H.B. Michaelson, *IBM J.Res. Dev*. **22**, 72 (1978).

6. M. Prutton, *Introduction to Surface Physics* (Clarendon Press, Oxford, 1994), p. 118.

7. R.W. Strayer, W. Mackie and L.W. Swanson, *Surf. Science* **34**, 225 (1973).

8. G. Attard, C. Barnes, *Surfaces* (Oxford Chemistry Primers **59**, Oxford University Press, Oxford, 1998), p. 63.

9. J.S. Blakemore, *Solid State Physics*, 2nd ed. (Cambridge University Press, Cambridge, 1985) pp.170-176.

10. R.G. Wilson, *J. Appl. Phys*. **37**, 3170 (1966).

11. D.E. Eastman, *Phys. Rev*. **B2**, 1 (1970).

12. S. Dushman, *Rev. Mod. Phys.* **2**, 381 (1930).

13. J.C. Rivère, in *Solid State Surface Science*, Vol. 1, edited by M. Green (M.Dekker, New York, 1969), pp. 180-204.

14. A. Einstein, *Ann. d. Phys.* IV, **17**, 132 (1905).

15. R.H. Fowler, *Phys. Rev*. **33**, 45 (1931).

16. F. Wooten, R.N. Stuart, *Phys. Rev*. **186**, 592 (1969).

17. L.A. Du Bridge, *Phys. Rev*. **39**, 108 (1932).

18. S.M. Sze, *Physics of Semiconductors*, 2nd ed. (John Wiley & Sons, New York 1981), pp. 250-251.

19. M. Cardona and L. Ley in *Photoemission in Solids*, edited by L. Ley (Topics in Applied Physics **26**, Springer Verlag, Berlin 1978) pp. 22-23.

20. J. Hölzl, F.K. Schulte in *Solid Surface Physics*, edited by G. Höler (Springer Tracts in Modern Physics **85**, Springer Verlag, Berlin 1979) pp. 51-68.

21. I.D. Baikie, E. Venderbosch, J.A. Meyer and P.J.Z. Estrup, *Rev. Sci. Instrum*. **62**, 725 (1991).

22. Lord Kelvin, *Philos. Mag.* **46**, 82 (1898).

23. W.A. Zisman. *Rev. Sci. Instrum*. **3**, 367 (1932).

24. H. Palevsky, R.K. Swank, R. Grenchik, *Rev. Sci. Instrum*. **18**, 298 (1947).

25. J.C. Mitchinson, R.D. Prongle and W.E.J. Farvis, *J. Phys*. **E 4**, 525 (1971).

26. Y. Petit-Clerc and J.D. Carette, *Rev. Sci. Instrum*. **39**, 933 (1968).

27. B.H. Blott and T.J. Lee, *J. Phys.* **E 2**, 785 (1969).

28. I.D. Baikie, K.O. van der Werf, J. Broeze and A van Silfhout, *Rev. Sci. Instrum*. **60**, 930 (1989).

29. H.A. Engelhardt, P. Feulner, H. Pfnür and D. Menzel, *J. Phys.* **E10**, 1842 (1977).

30. L.B. Harris and J. Fiasson, *J. Phys.* **E 17**, 788 (1984).

31. I.D. Baikie, S. Mackenzie, P.J.Z. Estrup and J.A. Meyer, *Rev. Sci. Instrum*. **62**, 1326 (1991).

32. I.D. Baikie, Ph.D. thesis, University of Twente, 1988, ISBN 90-9002444-1.

33. I.D. Baikie, P.J Smith, D.M. Portefield, and P.J. Estrup, *Rev. Sci. Instrum*. **70**, 1842 (1999).

34. I.D. Baikie and P.J. Estrup, *Rev. Sci. Instrum.* **69**, 3902 (1998).

35. I.D. Baikie, K.O. van der Werf, and L.J. Hanekamp, *Rev. Sci. Instrum.* **59**, 2075 (1988).

36. U. Petermann, Ph.D. thesis, Robert Gordon University, 2000.

37. S. Teixeira, X. Pacheo, Borland® Delphi™ 4 Developers Guide (SAMS Publishing, Indianapolis, 1998), pp.654-712.

Chapter 3

Absolute Work Function Determination

3.1 INTRODUCTION

As discussed in the previous chapter, the Kelvin probe offers a number of advantages over other methods to measure *changes* in the sample work function. The Kelvin method is a non-contact, truly non-destructive technique. In contrast, e.g., the photoelectric effect method typically requires a high energy photon source which is likely to cause desorption of molecules from the sample surface and therefore changes its work function [1] which is also the case at the high temperatures required for the thermionic measurement method. Further, it is not possible to determine the work function of semiconductors with either the photoelectric, thermionic or field-effect method and, moreover, the work function of metal surfaces obtained with these methods is often biased towards low work function patches.

The Kelvin probe measures changes in the work function with a very high accuracy, typically < 1meV [2], in a temperature range from 2K up to 1000K. The measurement is fully automated and controlled by a host computer and can be performed with a rate of up to 1 data points per second. Further, it is possible to obtain work function topographies of the sample with the Scanning Kelvin Probe (SKP) [2]. In contrast, both the photoelectric and thermionic method are rather time consuming and a work function topography of the sample is not easily accomplished.

Despite its advantages, however, the Kelvin method is an inherently *relative* technique and does not provide the *absolute* work function of the sample if the work function of

the tip, ϕ_{tip}, is unknown. Yet, knowledge of the absolute work function value is of primary importance for a variety of applications, including e.g. the investigation of novel materials exhibiting a high or low work function such as metal oxides and lanthanum borides that can be applied for example to novel ion sources in mass spectrometer applications, see chapter 4.

Among the various techniques that measure the absolute work function the photoelectric effect method appears most suited since it neither requires high sample temperatures nor a special sample geometry as it is the case for the thermionic or field effect methods, resepctively [3]. Therefore a relatively simple extension of the Kelvin probe technique was developed to obtain ϕ_{tip}. This is achieved via measurement of the current voltage (I-V) characteristic of the photoelectric emission from a low work function surface [4, 5]. The work function of any conductor or semiconductor can then be obtained by subsequent Kelvin probe contact potential difference (CPD) measurements.

3.2 PRINCIPLE OF THE MEASUREMENT

As discussed in chapter 2, if a metal surface with work function ϕ_S is illuminated by monochromatic light of energy $h\nu$ with $h\nu > \phi_S$, see figure 3-1, the maximum kinetic energy E_{max} of the electrons emitted is given by the Einstein equation [6]

$$E_{\max} = h\nu - \phi_S \,. \qquad 3\text{-}1$$

Therefore, at the threshold frequency ν_0 below which no emission occurs, E_{max} equals zero, i.e.

$$h\nu_0 = \phi_S \,. \qquad 3\text{-}2$$

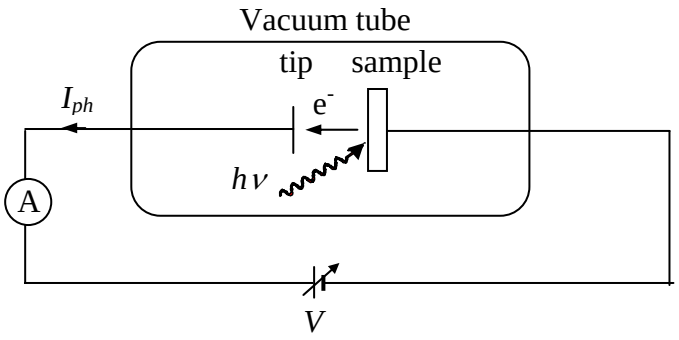

***Figure 3-1**. Schematic of the circuit for observing the photoelectric effect. When monochromatic light of energy $h\nu > \phi_S$ strikes the sample plate photoelectrons (e^-) are ejected and collected by the tip.*

The work function of the *emitter* (sample*)* can thus be determined by a measurement of the photocurrent as a function of the photon energy where the photocurrent near threshold is a function of ν given by [7, 8]

$$I_{ph} \propto (h\nu - \phi_S)^2 \qquad 3\text{-}3$$

and hence ϕ_S can be determined by a linear extrapolation of $I_{ph}^{1/2}$ to zero current.

On the other hand, the work function of the *collector* (tip) can be determined by illuminating the sample with monochromatic light of a fixed energy $h\nu$ with $\phi_{tip} > h\nu > \phi_S$ and varying the bias potential between collector and sample [9, 10]. This second method can be used to determine the work function of the Kelvin probe tip, ϕ_{tip}. This is visualised in figures 3-2 and 3-3 by means of the electron energy level diagrams and a schematic of the photocurrent characteristic depicted as a function of the bias potential applied between tip and sample. In figure 3-2 (a), upon electrical contact of the two metal surfaces, their Fermi levels equalise, resulting in a contact potential difference V_{CPD} which equals the work function difference between tip and sample:

$$qV_{CPD} = \phi_S - \phi_{tip}\,, \qquad 3\text{-}4$$

where ϕ_{tip} and ϕ_S are the work functions of the tip and sample, respectively.

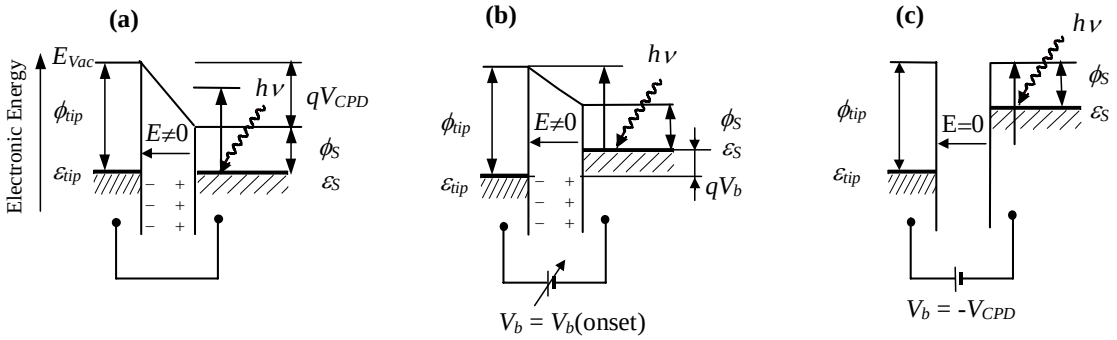

***Figure 3-2**. Energy level diagrams of the Kelvin probe in photocurrent measurement mode as a function of V_b with $\phi_{tip} > h\nu > \phi_S$: (a) no photoelectrons are collected at the tip, (b), the onset of the photocurrent is measured where $\phi_{tip} = h\nu + qV_b(onset)$ and in (c) the saturation current where $V_b = -V_{CPD}$. ε_{tip} and ε_S refer to the Fermi levels of the tip and sample, respectively.*

At zero bias potential, because of the retarding electrical field caused by V_{CPD}, assuming that $\phi_{tip} > \phi_S$, none of the emitted electrons will reach the collector, i.e. $I_{ph} = 0$, see figure 3-3 (a). With increasing bias potential V_b the Fermi level of the sample ε_S is shifted upwards with respect to ε_{tip}. At the point where electrons emitted from ε_S can just overcome the potential barrier the onset of the photocurrent at the Kelvin probe tip is measured, see figure 3-2 (b). In this case, the work function of the tip equals the photon energy E_{ph} plus the required bias potential at the onset supplied by V_b, i.e.:

$$\phi_{tip} = h\nu + qV_b(onset). \qquad 3\text{-}5$$

With further increasing bias potential, analogous to the first method, the photocurrent typically increases with V_b^2, see figure 3-3 (b), [10]:

$$I_{ph} \propto V_b^{\,2}. \qquad 3\text{-}6$$

When V_b equals $-V_{CPD}$ (figure 3-2 (c)), electrons emitted from energy states below ε_S with virtually zero velocity are only just able to reach the collector and the photocurrent saturates, see figure 3-3 (c).

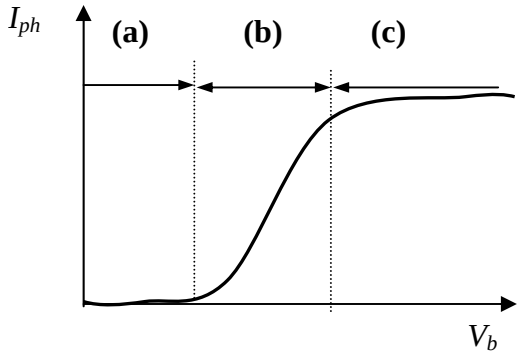

Figure 3-3*. Schematic of the photocurrent versus bias voltage (I-V) characteristic showing the 3 regions of the curve, a, b and c, corresponding to the 3 cases depicted in figure 3-2.*

3.3 EXPERIMENT

3.3.1 The Ultra-High-Vacuum System

The photoelectric effect measurements were carried out in the custom designed UHV chamber as shown in figure 3-4. The system is pumped by a turbo molecular pump (EXT351 CF160, BOC EDWARDS), a titanium sublimation pump (AML) and a roots pump (RV8, BOC EDWARDS). This design together with the fast entry load lock allows quick sample exchange and fast pump down of the system. The system pressure is monitored by an Bayard-Alpert (BA) type ionisation gauge and a wide range gauge (BOC EDWARDS) both controlled by an active gauge controller (AGC, BOC EDWARDS) which can be interfaced with a computer via the RS232 serial port. Residual gas analysis was performed with a quadrupole mass spectrometer (PRISMA QMS 200, BALZERS) in a mass range from 1 to 200 amu.

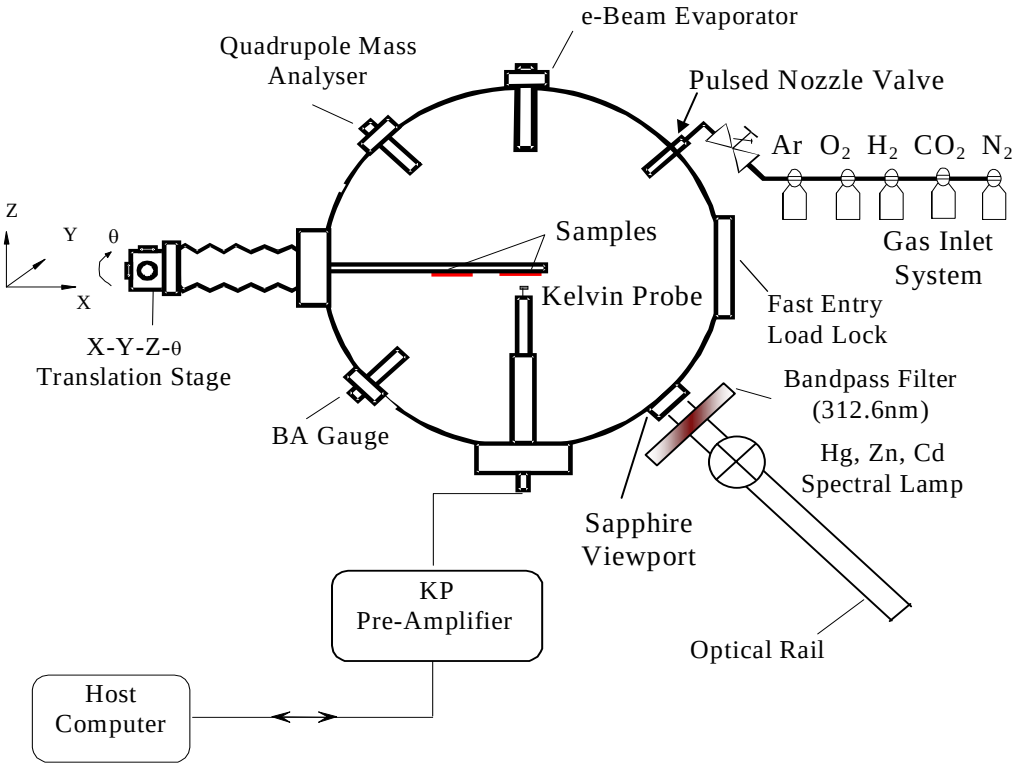

Figure 3-4. *Schematic of the UHV system including the Kelvin Probe and UV light source for absolute work function determination.*

Two samples can be mounted onto the sample holder where each sample has a separate external electrical connection. A manual (X-Y-Z-Θ) translator allows to change the position of the samples. Additionally, the chamber is equipped with a four pocket electron-beam evaporator (EGN4, Oxford Applied Research) for molecular beam evaporation, a Kelvin probe for contact potential measurements, a sapphire viewport which is transparent for wavelengths from 5μm down to 200nm to illuminate the sample via an external light source and a seperately pumped gas inlet system. The electron-beam evaporator and the gas inlet system are described in more detail in chapter 4 and 5, respectively. The Kelvin probe is discussed in chapter 2.

3.3.2 The Light Source

For the photocurrent measurements a low work function sample surface, used as a photoelectron source, is illuminated by a 100W Hg-Cd-Zn spectral lamp (Philips, 93146E) through the sapphire viewport. Figure 3-5 shows the relative intensities of the mercury (Hg) emission spectrum from 250nm to 550nm. Discrete emission lines of the spectral lamp can be selected by narrowband interference filters (FHMW = ± 20nm) for wavelengths of 253.7nm, 312.6nm and 365nm, which equal photon energies of 4.86 eV, 3.95 eV and 3.38 eV, respectively.

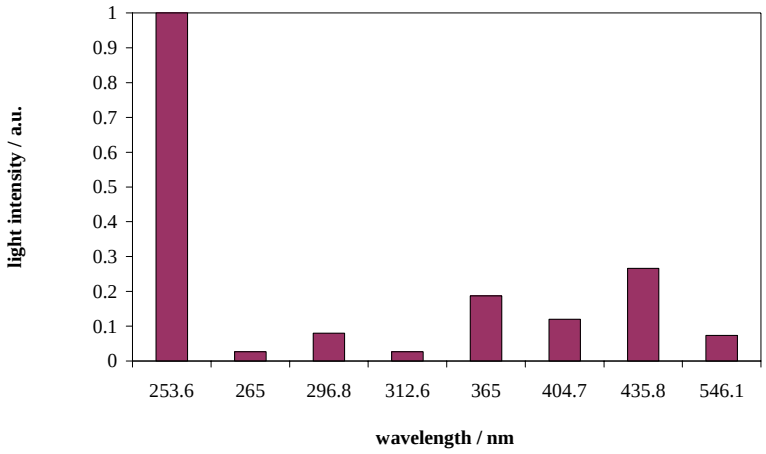

***Figure 3-5**. Relative light intensities of selected mercury emission lines [11].*

The light output signal of the spectral lamp is an ac-signal with a frequency of 100Hz as shown in figure 3-6.

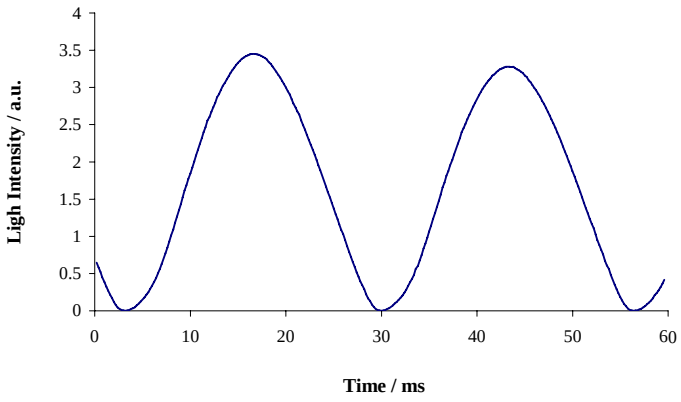

***Figure 3-6.** Light output of the Hg-Zn-Gd spectral line lamp.*

3.3.3 Photocurrent Measurement Instrumentation

The input stage of the Kelvin probe that is used for CPD measurements can also be used for the measurement of the photocurrent as shown in the circuit diagram in figure 3-7. The photocurrent I_{ph} emitted by the illumination sample plate (curved plate in the schematic) is collected by the stainless steel Kelvin probe tip (Ø2.5mm, flat plate in the schematic) that is connected to the inverting input (–) of the low noise operational amplifier (op-amp). The op-amp circuit converts this current into a voltage signal. The output voltage is determined by the feedback resistance R_f (=10^7 Ω) given by

$$V_{out} = -I_{ph} \cdot R_f \qquad 3\text{-}7.$$

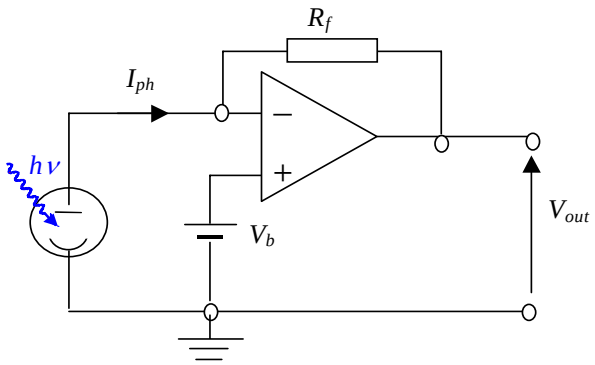

Figure 3-7. *Circuit diagram of the Kelvin probe input stage for photocurrent measurements.*

The emitter plate is held at ground potential and the voltage of the tip is set by the bias voltage V_b connected to the non-inverting input (+) of the operational amplifier. Since the voltage difference between the inputs of the amplifier is zero, the voltage of the inverting input and hence of the tip is determined by V_b [12]. This signal is then further amplified by a variable gain stage, filtered and digitised by the 12-bit AD-converter of the data acquisition card (PCI 1200, National Instruments) and processed by the host PC using the dedicated software program as shown in figure 3-8. The bias potential V_b is programmatically set by one of the 12-bit DAC's on the data acquisition system (DAS).

3.3.4 Software Development

The software program to automate the measurement of the photoemission I-V characteristic was written for the 32-bit Microsoft Windows™ operating system environment in the object orientated programming language Borland Delphi™. A block diagram of the program is presented in figure 3-9. Initially, all the experimental parameters are input, i.e. the start and final value and the step size of the bias potential, the number of averages as well as the parameters for the signal acquisition.

(a)

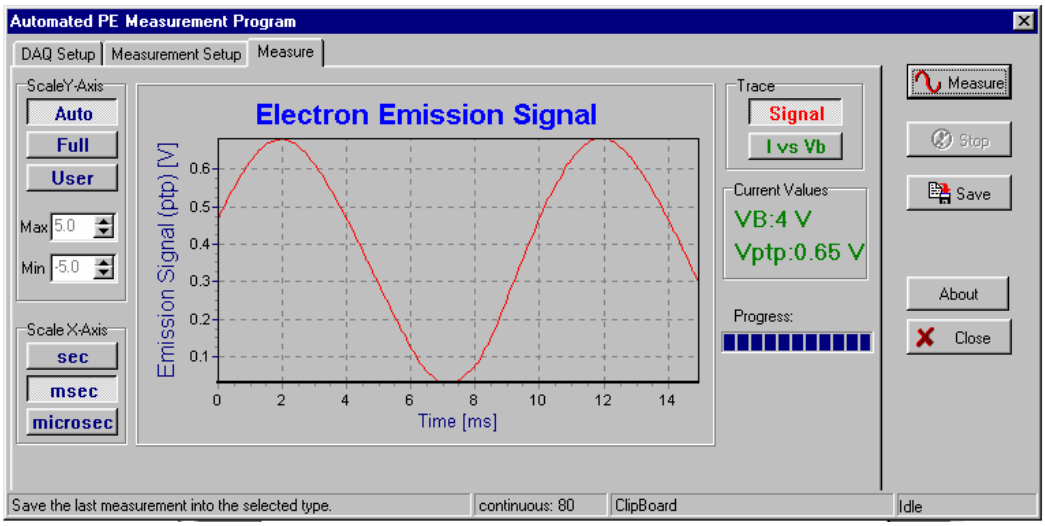

(b)

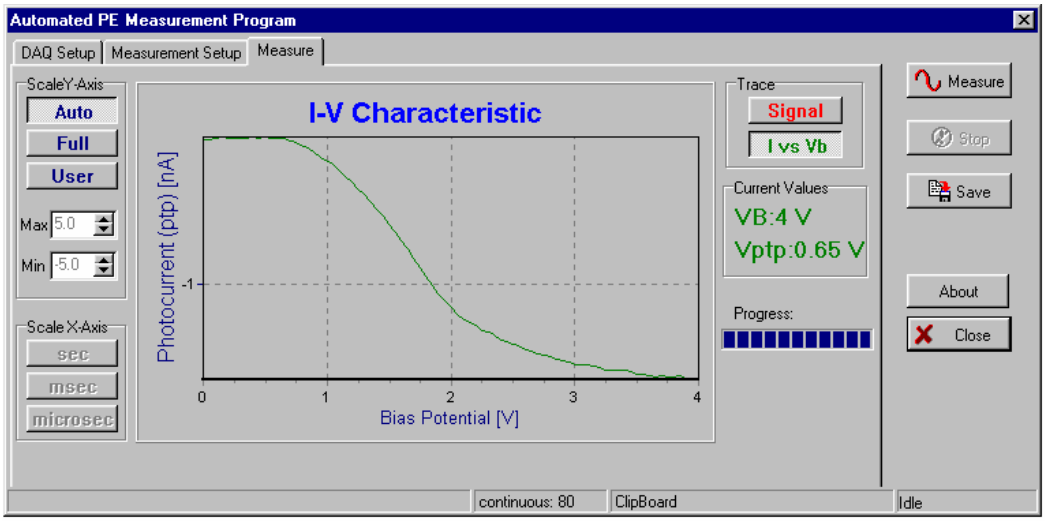

***Figure 3-8**. Screenshots of the photocurrent measurement program showing (a) the acquired ac-signal of the electron emission and (b) the corresponding I-V_b characteristic.*

The bias potential V_b is set using DAC1 and a short delay is built in to allow the output signal to settle. Then the DAS acquires the signal which is stored to an internal array and the program proceeds with the next measurement. The second array is added to the first for the required number of averaging loops 'n'. This method (boxcar integration) effectively reduces noise.

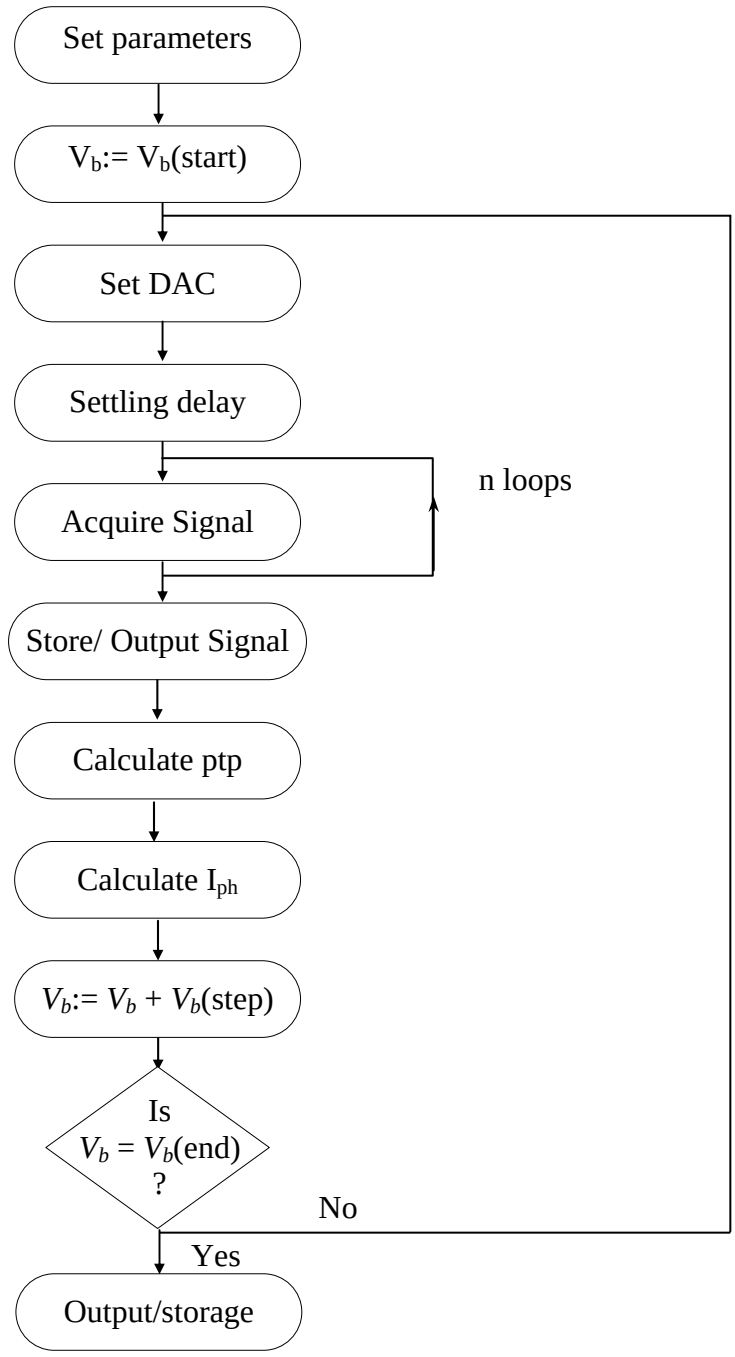

Figure 3-9. *Block diagram of the photo-effect measurement program.*

Upon completion of the measurement the data are divided by ‘n’, the peak-to-peak (ptp) voltage of the signal is determined and the voltage signal is converted back into the photocurrent. This value is then stored together with V_b in a second array and plotted against the applied bias potential and the above process repeated for the next value of V_b.

3.4 RESULTS

A polycrystalline gadolinium (Gd) foil ($25\times12\times0.1mm^3$,ADVENT, 99.99%) was used as the *photoelectron source*. The sample was cleaned by repeated resistive heating up to 1200K for several minutes. Gd has the advantage of having a relatively low work function of approximately 3.1eV [13] and is available in form of thin foils. Further, it was found that the work function of Gd remained very stable with exposure to residual gas over a prolonged period of time (see below). Subsequent CPD measurements were made on a polycrystalline rhenium foil ($25\times12\times0.025mm^3$, ADVENT, purity 99.99%) that was evaluated as a target surface for HSI, see chapter 4. This foil was cleaned by repeated flash annealing to temperatures above 2000K. Experiments were carried out at base pressures of the UHV system of $< 4\times10^{-9}$ Torr. The system was darkened during the measurements and all filaments were extinguished.

Figure 3-10 shows the I-V characteristics of the photoemission from the Gd surface for the 3 Hg emission lines. The photocurrent increases as expected with increasing photon energy. Due to the small difference between ϕ(Gd) and E_{ph} at the 365nm line, the magnitude of the photocurrent is very small and hence the signal to noise ratio (S/N) is poor. On the other hand, although giving the highest signal magnitude, photons emitted at 253.7nm, having an energy of 4.86eV, may cause additional emission from the Kelvin probe tip or metal parts in the UHV chamber that might interfere with the

measurement. Thus, the 312.6nm line with E_{ph} = 3.95 eV is best suited for this setup and was used for subsequent measurements.

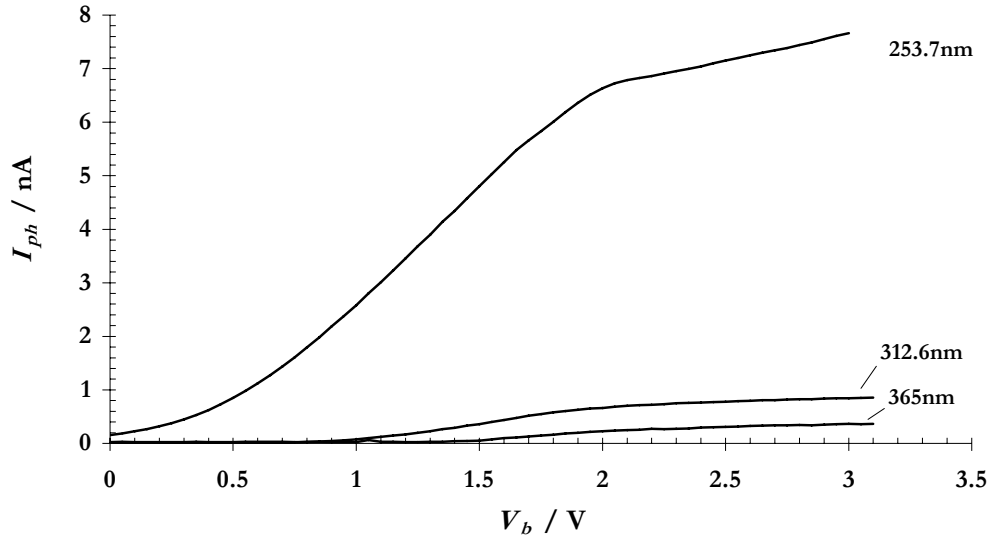

Figure 3-10. *The current-voltage (I-V) characteristic of the photoemission used to determine the work function of the Kelvin probe tip.*

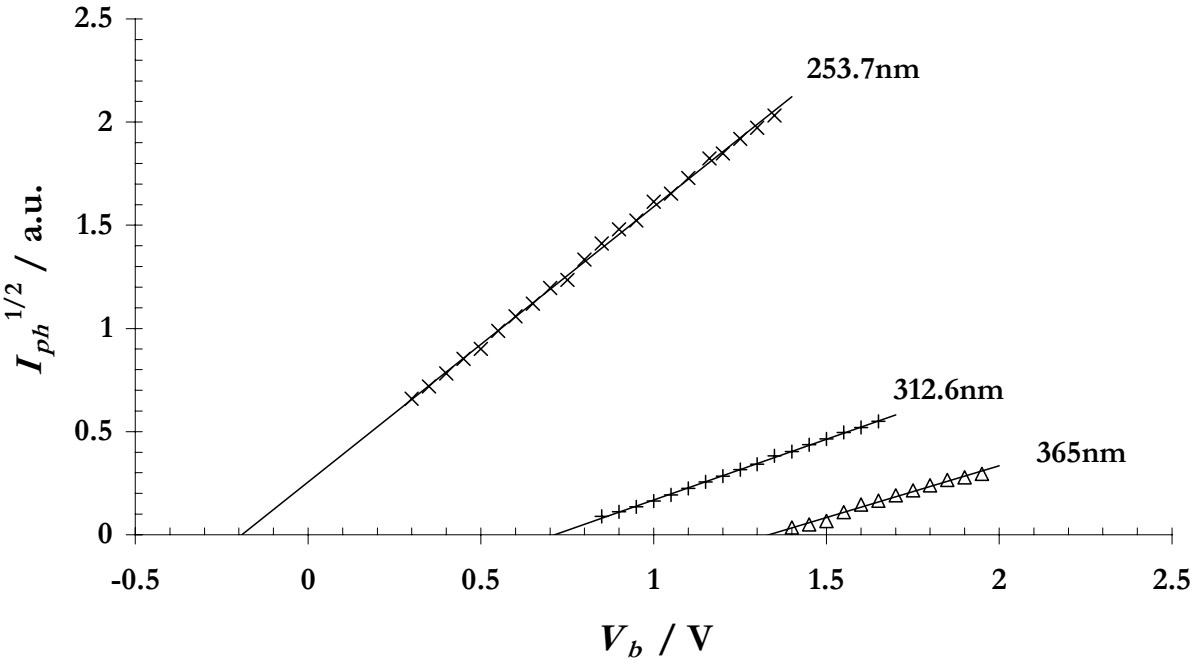

Figure 3-11. *The plot $I_{ph}^{1/2}$ of the data in figure 3-10 versus bias voltage. Note that only data from the linear portion of the curves are included in the linear fit.*

In order to determine the onset of the photocurrent I_{ph}, the square root of I_{ph} is plotted versus the applied bias voltage V_b, see figure 3-11, and a least square fit of the linear part of the curve is extrapolated to zero current. ϕ_{tip} is then calculated via equation 3-5. The results of the measurements are summarised in table 3–1. It can be seen that the values for ϕ_{tip} measured by 3 different Hg emission lines agree within 30mV. The uncertainty of the extrapolation for the 312.6nm line is ±10mV. Taking the measurement error due to the thermal energy distribution into account, i.e. 26mV at 300K, and small changes in tip work function during the measurement, typically <20meV, the overall error of the work function measurement is estimated to be ±50meV.

***Table 3-1**. Results of the measurements to determine the absolute work functions.*

Hg line / nm	E_{ph} **/ eV**	V_b**(onset) / V**	ϕ_{tip} **/ eV**
253.7	4.86	-0.192 ± 0.007	4.672
312.6	3.95	0.714 ± 0.010	4.662
365	3.38	1.335 ± 0.067	4.716
Average	/	/	4.683 ± 0.030

The work function of the sample, ϕ_S, is then determined via a subsequent measurement of V_{CPD} and using equation 3-4. An example of such measurements is shown in table 3-2. The work function of the Kelvin probe tip was determined as described above. The contact potential difference was then measured for the Gd surface that was used as the photoelectron source and the rhenium foil after cleaning. The work function determined for Gd of (3.075 ± 0.050) eV is, within the measurement error, in agreement with that of (3.10 ± 0.15) eV given in [13]. The work function determined for the clean Re substrate, in this case of (5.171 ± 0.050) eV, was used as a calibration point for the absolute work function values of Re given in chapter 4.

***Table 3-2**. Results of the measurements to determine tip and sample work functions.*

Measurement	E_{ph} / eV	V_b(onset) / V	V_{CPD} / V	ϕ / eV
Kelvin Probe tip	3.966	0.551± 0.016	/	4.518
Gd	/	/	-1.443	3.075
Re	/	/	0.653	5.171

The work function of low ϕ materials is known to increase with the adsorption of residual gas molecules. Therefore the stability of the work function of the gadolinium foil that is used as the photoelectron source was determined immediately after the cleaning process and after 16 hours of exposure to the residual gas envelope in the UHV chamber at a base pressure of 3.7×10^{-9} Torr, see figure 3-12.

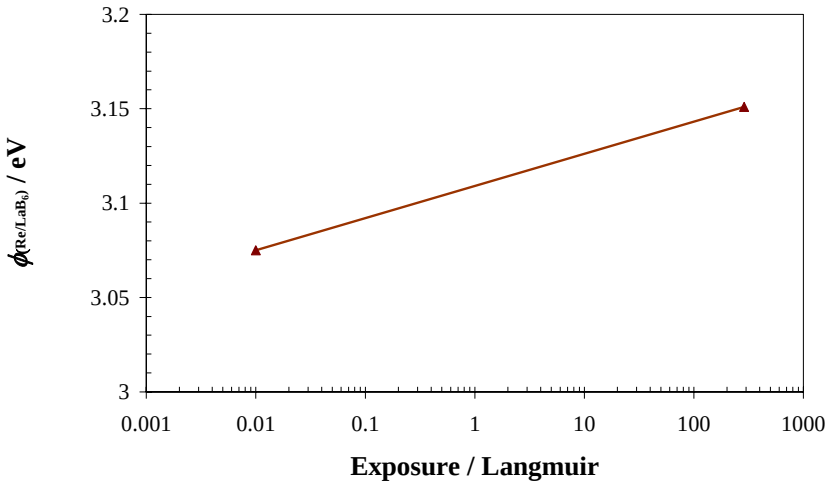

***Figure 3-12**. Work function increase of Gd due to the adsorption of residual gas molecules at 300K and a base pressure of 3.7×10^{-9} Torr.*

We find that the work function increases by only 70meV after an exposure of 200L. This shows that the work function of Gd is relatively unaffected by the exposure to gas molecules, in contrast to other low work function materials as e.g. lanthanum hexaboride (LaB_6) or calcium (Ca), see chapter 4.

REFERENCES

1. J.S. Kim, B. Lägel, E. Moons, N. Johansson, I.D. Baikie, W.R. Salaneck, R.H. Friend, F. Cacialli, *Synth. Met.* **111-112**, 311 (2000).

2. I.D. Baikie, U. Petermann, B. Lägel, *Surf. Sci*. **433-435**, 249 (1999)

3. J.C. Rivère, *in Solid State Surface Science*, Vol. 1, edited by M. Green (M.Dekker, New York, 1969), pp. 180-204.

4. B. Lägel, I.D. Baikie, K. Dirscherl and U. Petermann in *Electron-Emissive Materials, Vacuum Microelectronics and Flat-Panel Displays*, edited by K.L. Jensen, W. Mackie, D. Temple, J. Itoh, R. Nemanich, T. Trottier, P. Holloway (Mater. Res. Soc. Proc. **621**, Pittsburgh, PA, 2000) in press.

5. B. Lägel, I.D. Baikie, K. Dirscherl and U. Petermann in *Recent Developments in Oxide and Metal Epitaxy – Theory and Experiment*, edited by M. Yeadon, S. Chiang, R.F.C. Farrow, J.W. Evans, O. Auciello (Mater. Res. Soc. Proc. **619**, Pittsburgh, PA, 2000) in press.

6 A. Einstein, *Ann. d. Phys.* (4) 17, 132 (1905).

7. R.H. Fowler, *Phys. Rev.* **33**, 45 (1931).

8. F. Wooten, R.N. Stuart, *Phys. Rev.*, **186** (1969).

9. P.M. Gundry, F.C. Tompkins, in *Experimental Methods in Analytical Research*, edited by R. Anderson (Academic Press, 1968), p. 113-116.

10. L. Apker, E. Taft, J. Dickey, *Phys. Rev.* **73**, 46 (1947).

11. Handbook of Chemistry and Physics, 74th ed., edited by D. R. Lide (CRC Press, Boca Raton, 1993-1994), p. 10-57.

12. P. Horowitz, W. Hill, *The Art of Electronics* (Cambridge University Press, Cambridge, 1980) pp. 92-99.

13. D.E. Eastman, *Phys Rev.* **B2**, 1 (1970).

Chapter 4

Evaluation of High and Low Work Function Surfaces

4.1 INTRODUCTION

The aim of this study was to produce and characterise surfaces optimised for Hyperthermal Surface Ionisation (HSI), an alternative to electron impact ionisation for a novel mass spectrometer system. HSI is based on the well-known phenomenon of surface ionisation [1] which is discussed in chapter 5. The species to be ionised is accelerated in a supersonic molecular beam towards a target surface. At a certain critical distance from the target surface, a spontaneous electron transfer can occur either to or from the molecule, thus creating a negative or positive ion, respectively. The first process is termed negative ion hyperthermal surface ionisation – n-HSI and the latter positive ion hyperthermal surface ionisation – p-HSI. A key factor for the ionisation efficiency in both HSI processes is the work function ϕ of the target material: mainly positive ions are created on high ϕ surfaces whereas for negative ion production low ϕ surfaces are required.

Potentially suitable target surfaces were identified via a literature study. The polycrystalline metals tungsten (**W**), molybdenum (**Mo**), rhenium (**Re**), palladium (**Pd**) and platinum (**Pt**) were found particularly interesting as p-HSI target surfaces since oxidation substantially increases their work function. The following parameters were investigated: a) the magnitude and sign of $\Delta\phi$ with molecular oxygen exposure as a function of substrate temperature, b) the effect of molecular hydrogen pre-adsorption on

the clean surface, and c) the effect of the surface cleaning procedure, i.e. Flash-Anneal (FA) and Sputter-Anneal (SA) cleaning, in terms of work function stability.

The low work function materials lanthanum hexaboride (**LaB_6**), calcium (**Ca**) and gadolinium (**Gd**) were investigated as potential target materials for n-HSI, i.e. the generation of these surfaces and the stability of their work function.

4.2 HIGH WORK FUNCTION SURFACES

4.2.1 Discussion

Three aspects have to be considered for the choice of materials for high work function surfaces: (i) the work function of the clean surface, (ii) the work function change due to the adsorption of electronegative gases and (iii) their stability at the high temperatures ($T > 1000$K) that are necessary to keep the surfaces clean from contamination. Refractory metals, listed in table 4-1 are excellent candidates in this respect, since they typically have a high melting point *and* a relatively high work function, see e.g. figure 2–2.

***Table 4-1**. Work function and melting point of a selection of polycrystalline metals [2].*

Element	**work function / eV**	**melting point / °C**
Pt	5.65	1772
Pd	5.12	1554
Re	4.96	3180
Mo	4.60	2617
W	4.55	3410
Ir	5.27	2410
Ni	5.15	1453
Rh	4.98	1966
Ru	4.71	2310

As discussed in chapter 2, the work function change $\Delta\phi$ is closely related to the dipole moment induced by the adsorbed molecule which depends on the degree of charge transfer in the bonds to the surface atoms. This charge transfer can be described by the concept of the electronegativity, χ, which is the magnitude of the energy change if an atom or molecule gains an electron. Most widely used is Paulings's electronegativity scale [3] that will be utilised here to give a prediction of the degree of charge transfer to be expected between the adsorbate and the different metal surfaces.

To achieve a work function increase, as pointed out in chapter 2, the adsorbate should exhibit a high – and the surface atoms a low electronegativity, respectively. Table 4-2 gives an overview of electronegative gases for the choice of the adsorbate. Although fluorine is the most electronegative of all elements, its use is restricted because of its high toxicity. Therefore, oxygen is used as the preferred reactant.

***Table 4-2**. Electronegativities of a selection of gases.*

Element	**$\chi_{(Pauling)}$ / eV**
F	3.98
O	**3.44**
N	3.04
H	2.20

Table 4-3 compiles the atomic electronegativities of the metals given in table 4-1 and their difference in electronegativity compared to oxygen. Since the work function change depends on charge transfer as well as the direction and length of the dipole, table 4-3 also contains experimentally obtained maximum work function data and their source in the literature. These data were used to select the most suitable candidates for this high work function surface study.

***Table 4-3**. Electronegativities and work functions of the metals listed in table 4-1. The element in bold letters were chosen for the work function study.*

Element	$\chi_{(Pauling)}$ **/ eV**	$\Delta\chi$ **/ eV**	$\Delta\phi$**(peak) / eV**	ϕ**(peak) / eV**	**Reference**
Re	1.90	1.54	1.8	7.15	[4]
Mo	2.16	1.28	1.35	6.3	[5]
Pt	2.28	1.16	1	6.3	[6]
Ir	2.20	1.24	1	6.3	[7]
Rh	2.28	1.16	1	6.0	[8]
Pd	2.20	1.24	0.7	5.8	[9]
Ni	1.91	1.53	0.65	5.8	[10]
Ru	2.20	1.24	0.85	5.55	[11]
W	2.36	1.08	0.85	5.4	[12]

Among these potential target materials several had to be ruled out for various reasons. The work function of the oxidised surface of iridium was found to decrease with increasing temperature and strongly affected by hydrogen adsorption [7], which is used as a carrier gas in HSI. Similarly, nickel exhibits an unstable and even decreasing work function with increasing oxygen exposure [10]. Ruthenium (Ru) is an extremely brittle material and hence difficult to handle whereas rhodium (Rh) is the rarest metal on earth and therefore exceptionally expensive. Of the remaining metals we find a good correlation between $\Delta\chi$ and the experimentally found work function change $\Delta\phi$, with rhenium the most favourable candidate because of its high initial work function *and* $\Delta\chi$ or $\Delta\phi$, respectively.

4.2.2 Experiment

A. The UHV-SKP System

The UHV system used for this study is illustrated in figure 4-1. The chamber comprises a volume of ≈ 85l pumped by a 20.5m^3 h^{-1} rotary pump (Edwards, RV18), a 250ls^{-1} turbomolecular pump (TMP, Edwards EXT 200), an ion-getter unit (4×25 ls^{-1}, AEI P1250) and a 3-rod Ti sublimator pump (TSP). Bayard-Alpert (BA) type ionisation gauges (VG, VIG17) on the main system and on top of the TMP provide the pressure reading of the system (p_{sys}) and at the TMP (p_{tmp}), respectively.

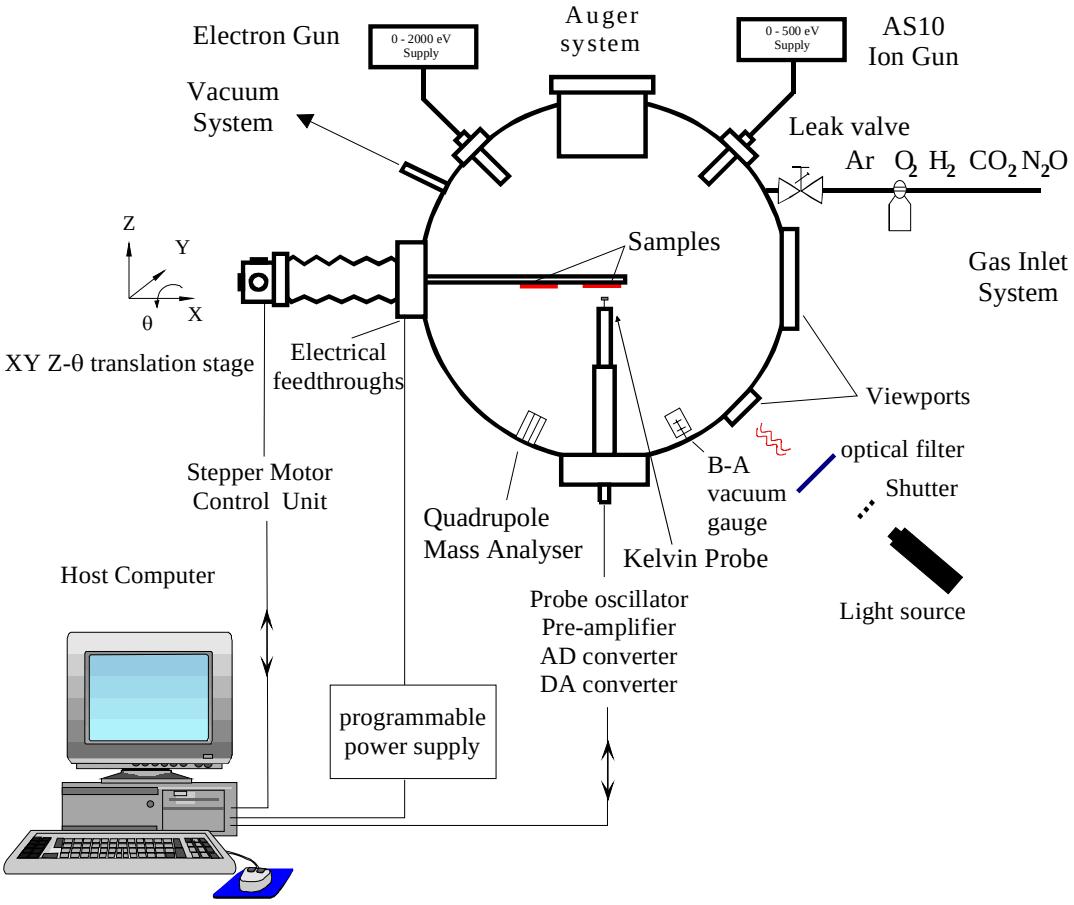

***Figure 4-1**: Schematic of the main UHV system with its associated peripherals and facilities.*

The system further comprises a Scanning Kelvin Probe (SKP), Auger-Electron Spectroscopy (AES), a Low Energy Electron Diffraction (LEED) unit and an argon ion gun for sputter cleaning. Residual gas analysis (RGA) can be performed with a 'Vacscan' quadrupole mass-spectrometer (QMS) with a detection range from 1 to 100 a.m.u.. A typical mass spectrum of the system after bake-out is shown in figure 4-2 with H_2, H_2O, CO and CO_2 being the main constituents. Additionally, the QMS was frequently used for checking the purity of the inlet gases and for leak detection.

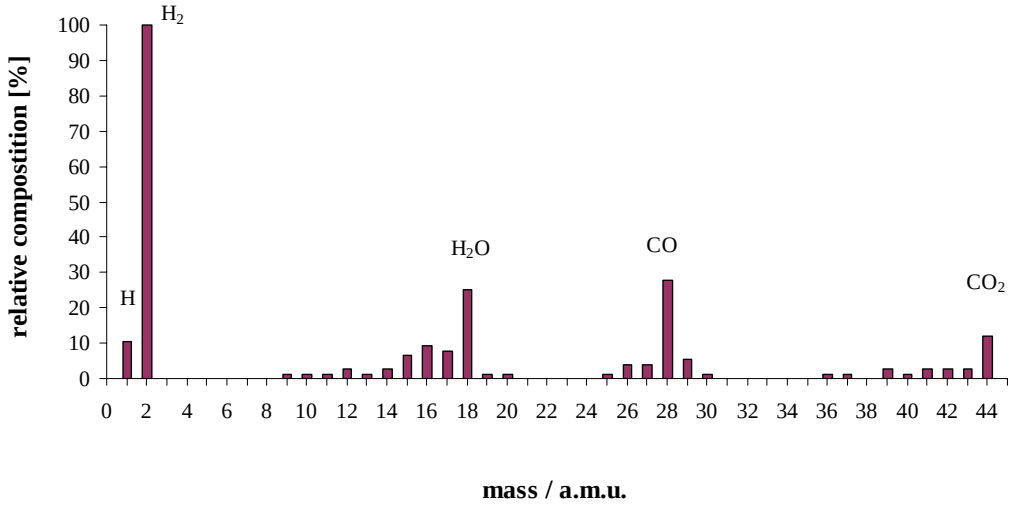

Figure 4-2. *Typical residual gas spectrum after bake-out, at a system base pressure of* $\leq 1\times10^{-10}$ *Torr.*

After the initial pump down the system was baked out at approximately 120°C for 48 hours thus reducing the H_20 peak to below 1% of its initial value. System pressures of typically $\leq 1\times10^{-10}$ Torr were achieved by operating the ion getter pump and using the TSP to reduce the amount of H_2 which is typically the main residual in the chamber. The monolayer formation time at this pressure is more than 20 minutes and hence long enough to ensure that the gases let in to the system are indeed adsorbed on a clean sample surface.

B. Gas Inlet

The gas inlet system, shown in figure 4-3, is separately pumped by a rotary pump and a $65ls^{-1}$ TMP (EDWARDS, EXT70). The pressures at the different parts of the inlet system, p_{rot}, p_{tmp} and p_{inlet}, are indicated by the corresponding pressure gauges. The gases used for the experiments, O_2 and H_2 (MESSER GRIESSHEIM), are provided in 1l metal cans with a purity of 99.998 and 99.999 Vol.%, respectively.

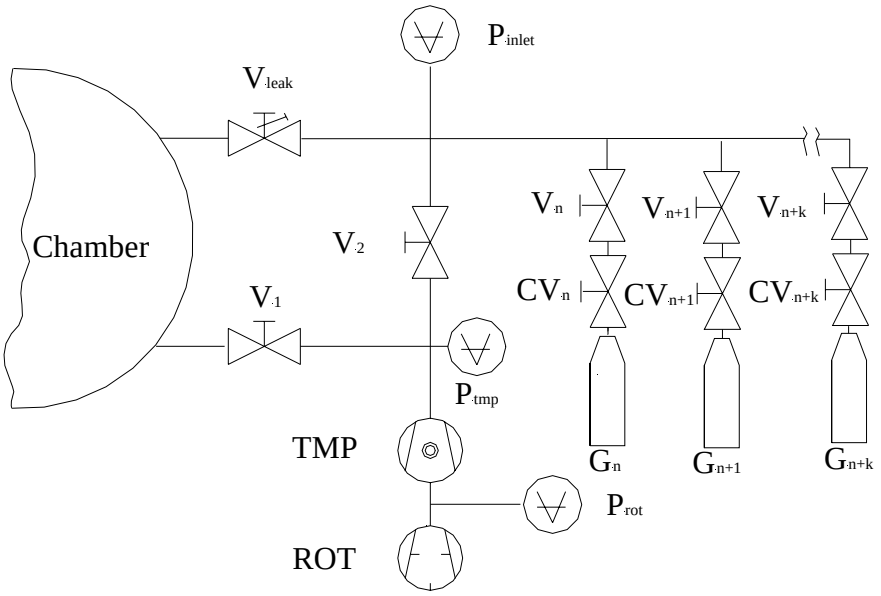

Figure 4-3. *Schematic of the gas inlet system and its components: the rotary pump (ROT), TMP, P_{rot}, P_{tmp} and P_{inlet}, - pressure gauges of rotary and turbomolecular pump and inlet system, V_{leak}, V_1, V_2, V_{leak}, V_n … V_{n+k} – UHV valves (see text), CV_n … CV_{n+k} – control valves of the gas cans, G_n … G_{n+k} – gas canisters for the various gases.*

For the admission of gas into the main system, e.g. for dynamic gas adsorption experiments or for argon ion sputtering, the valve V_2 to the TMP is shut. Gas from the high pressure can is admitted first into the small volume of the coupling tube between control valve CV_n and the UHV valve V_n by opening CV_n. Subsequently, control valve CV_n is shut and the UHV valve V_n opened. Finally, the gas is admitted into the main system via the leak valve V_{leak} that allows to adjust the gas pressure in the main system between 5×10^{-10} Torr and 1×10^{-3} Torr.

During gas inlet the ion-getter unit and the system ionisation gauge are switched off to prevent damage of these components at higher gas inlet pressures. This also avoids potential side effects that might be caused by fragmentation of gas molecules on the hot filaments of the ionisation gauge [13, 14]. The pressure reading was therefore taken from the ionisation gauge mounted onto the TMP. To correlate the pressure at the TMP, p_{tmp}, to the pressure in the main system, p_{sys}, the readings of both gauges were recorded simultaneously from the analogue outputs of the gauge controllers. Figure 4-4 shows for example the output voltages of both gauges as a function of the pressure of molecular oxygen in the main chamber. ·

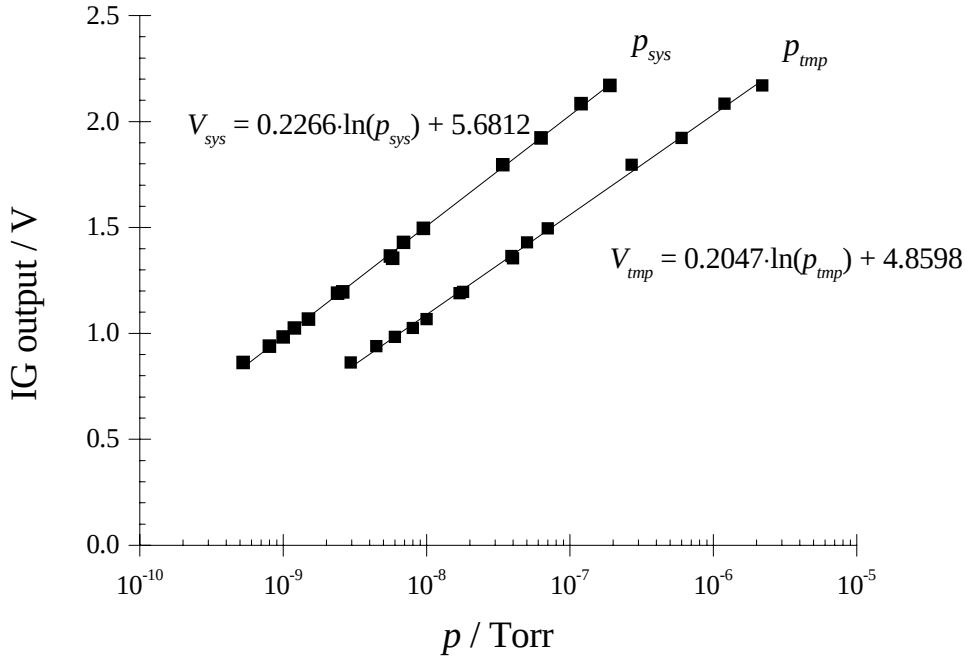

***Figure 4-4**. Relationship between the pressure in the main system and the analogue output of the ionisation gauges mounted onto the main system and the TMP, respectively.*

C. Sample Preparation, Heating and Temperature Measurement

The polycrystalline metal foils (13mm × 25mm × 25μm) were mounted onto the UHV sample holder via tantalum pressure contacts. Clean sample surfaces were generated by either Flash-Anneal (FA) cycles to temperatures as listed in table 4-4 or via Sputter-Annealing (SA). SA is performed by Ar Sputtering (45^o, $2\mu Acm^{-2}$, 20 mins) and a subsequent annealing step (1200K, 60mins) followed by a FA. For FA cleaning the samples were resistively heated by an ac power supply unit (PSU) and by a dc PSU for Kelvin probe CPD measurements at elevated temperatures. The initial sample cleaning was performed by a series of FA cleans. The work function was monitored during the FA cleans and a stable ϕ value was obtained typically after 6 to 8 cycles.

Table 4-4: *Melting point T_m and flash anneal temperatures T_{FA} of the polycrystalline metal samples used.*

Element	T_m **(°C)**	T_{FA} **(°C)**
Re	3180	≈1800
W	3410	≈1800
Mo	2617	≈1800
Pt	1772	≈1100
Pd	1554	≈900

Sample temperatures in the range from 600°C to 3000°C were measured with an optical pyrometer (MINOLTA, LAND Cyclops 152A). Optical pyrometry is a non-contact measurement technique where the amount of energy emitted from a hot surface is determined [15]. The power *P* radiated from an object is related to the temperature of its surface T_S by the Stefan-Boltzmann law:

$$P = \varepsilon \sigma A T_S^{\,4}, \qquad 4\text{-}1$$

where ε is the emissivity of the surface, A is the sample surface area and σ is the Stefan-Boltzmann constant. Thus, in order to determine T_S, it is necessary to know the emissivity of the sample surface. The values of ε used for the studied samples are listed below in table 4-5.

***Table 4-5**: Emissivity values of the samples investigated [2].*

Samples	Emissivity
Pt	0.30
Pd	0.33
Mo	0.37
Re	0.42
W	0.43

To determine the sample temperature below the measurable range of the pyrometer, i.e. <600°C, the input power P_{in} versus temperature data were fitted to equation 4-2 via a Levenberg-Marquardt iteration [16] and extrapolated to temperatures below 600°C as e.g. shown in figure 4-5. In a vacuum, bodies can exchange heat only via thermal radiation or thermal conduction through external contacts. Thus, the input power P_{in}, which is equal to the power loss in steady state, and the sample temperature can be correlated by:

$$P_{in} = \beta_0 (T_S^4 - T_0^4) + \beta_1 (T_S - T_0), \qquad 4\text{-}2$$

The first part in the above equation describes the heat loss via radiation where β_0 is the thermal radiation factor and the second part the heat loss via thermal conduction where β_1 is the thermal conductivity factor. T_0 is the temperature of the surroundings, i.e. normally 300K. The thermal radiation factor is given in equation 4-1 by

$$\beta_0 = \varepsilon\sigma A\,. \qquad 4\text{-}3$$

An example of such a dataset is plotted in figure 4-5 together with the fit of the data and the two contributions to the heat loss of the sample according to equation 4-2.

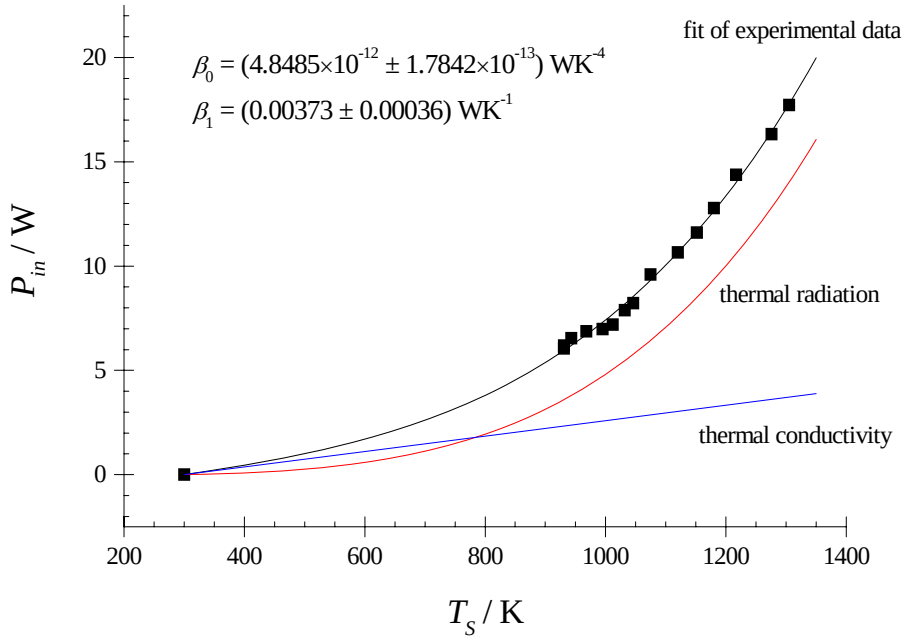

***Figure 4-5**. Input power as a function of the Re sample temperature.*

We see that for temperatures up to 800K the heat is dissipated mainly by thermal conduction through the contacts of the sample holder which represents a significant thermal mass compared to the metal foil. At temperatures above 800K thermal radiation dominates the heat loss.

By using equation 4-2 we assume the temperature measured to be a constant over the whole surface area, which is however not generally the case. With the value obtained for β_0 for the example in Figure 4-5, according to equation 4-3, the effective area would be 1.98cm^2 compared to the true sample area of 2.21cm^2. This difference is probably due to the inhomogeneous temperature distribution across the sample surface, especially close to the sample contacts. The sample contacts are a crucial factor in how good the

power is dissipated in the vicinity of the contacts. Therefore the fit parameters will vary from sample to sample and have to be determined for each sample individually.

D. Thermal Cycling

For rapid determination of the work function as a function of the substrate temperature during gas adsorption the substrate temperature was gradually increased until a saturation value of ϕ was achieved. The change in the potential of the sample, caused by passing a heating current through the sample, produces an apparent shift in ϕ. This shift was eliminated by post-processing of the data. All work function data were obtained by taking $\Delta\phi$ at the equilibrium oxygen pressure p_{ox} of ~1×10^{-5} Torr at the various temperatures. The measurements were started at room temperature until a stable work function was achieved followed by subsequent heating steps up to temperatures of 1100K.

E. Absolute Work Function Values

In order to determine absolute ϕ values and to monitor for possible changes in the tip work function ϕ_{tip} during sample processing two tip calibration procedures have been implemented: (i) photoelectric emission, which is described in chapter 3, and (ii) *in-situ* reference electrodes. The photoelectric emission method relies upon the availability of a low work function (Gd) surface, however during oxidation the work function of this surface increases and thermal cycling is required to restore the original surface work function. Thus for a rapid but less rigorous check of ϕ_{tip}, V_{cpd} was also measured relative to two *in-situ* reference samples (gold and aluminium) located on a linear transfer arm. The use of various reference electrodes in the Kelvin method, including gold and aluminium, has been described in detail in [17].

4.2.3 Results

A. Tungsten

The polycrystalline tungsten sample was cleaned by several flash-anneal cycles at temperatures ≥ 2000K. The resulting work function of the clean surface was determined to be (4.65 ± 0.10)eV which agrees well with the literature data presented in table 4-1.The dynamic work function change measured upon uptake of molecular oxygen for a selection of temperatures is plotted in Figure 4-6. We can see that, generally, the work function increases with the uptake of oxygen and tends to saturate at higher exposures and that the saturation value of ϕ increases with increasing temperature. The uptake curves at T_S = 300K consist of 2 parts: a rapid initial increase in ϕ for exposures < 100L followed by a slowly increasing part at higher exposures. This second phase does not occur at $T_S \geq$ 800K and saturation of ϕ is already achieved at exposures of ≈100L.

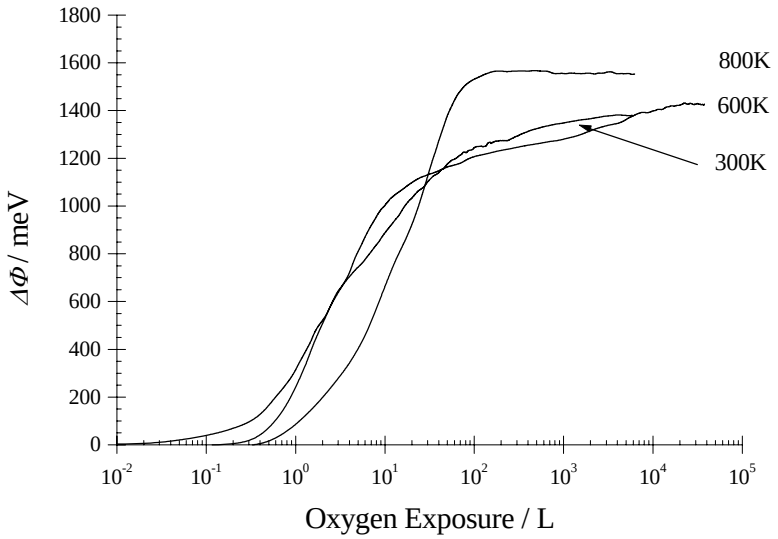

Figure 4-6*. The work function increase during oxidation of W at a selection of different temperatures.*

The saturation work function obtained during oxidation for temperatures from 300K up to 1100K is plotted in Figure 4-7. The curve reveals an approximately linear increase in

$\Delta\phi$ from 1.33eV at T_S = 300K up to 1.67eV at T_S = 1000K, followed by a decrease at higher temperatures where a maximum work function of 6.32eV is observed at 1000K. The work function increase of 1.33eV obtained at 300K is in good agreement with that of ~1.6 eV reported in [18, 19] for the O_2/W(100) system using the retarding potential method.

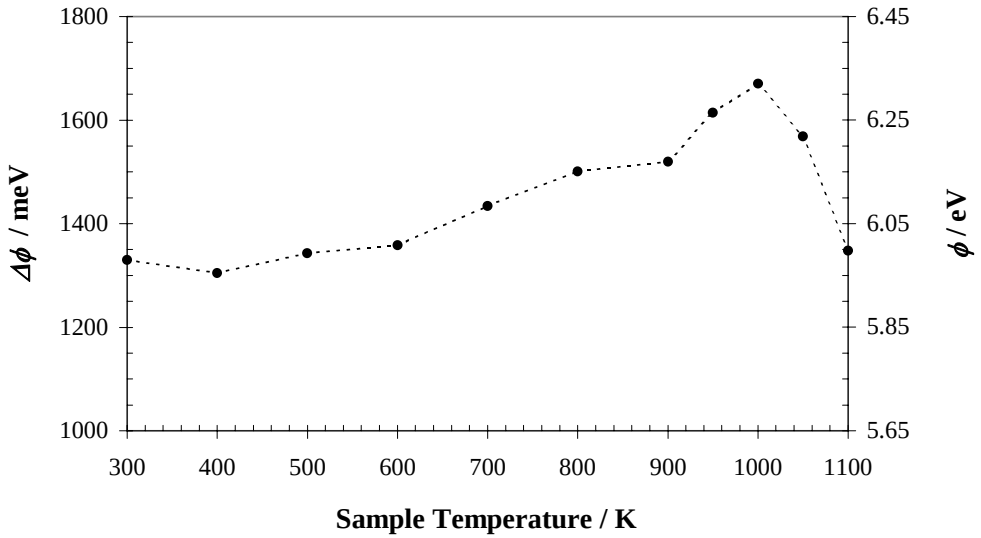

Figure 4-7. *Work function changes during oxidation of polycrystalline tungsten at different temperatures with ϕ = 4.65 eV of the clean surface.*

B. Molybdenum

The polycrystalline molybdenum (Mo) sample produced a work function value of (4.50 ± 0.10) eV after several flash-anneal cleaning cycles. This value agrees, within the experimental error, with the literature value given in table 4-1. Figure 4-8 shows the saturation work function of the oxidised sample surface, i.e. at $p(O_2)$ = 5×10^{-5} Torr, for a series of sample temperatures. The data indicate that the magnitude of $\Delta\phi$ remains almost constant at ~1.7eV up to 900K. A work function peak of ϕ = 6.43eV, i.e. $\Delta\phi$ = 1.87eV, emerges at 1000K. This result is in excellent agreement with the oxidised

Mo wire data published by Zandberg [20], reporting a peak $\Delta\phi$ of ~1.9eV at a temperature of T_S ~ 980K.

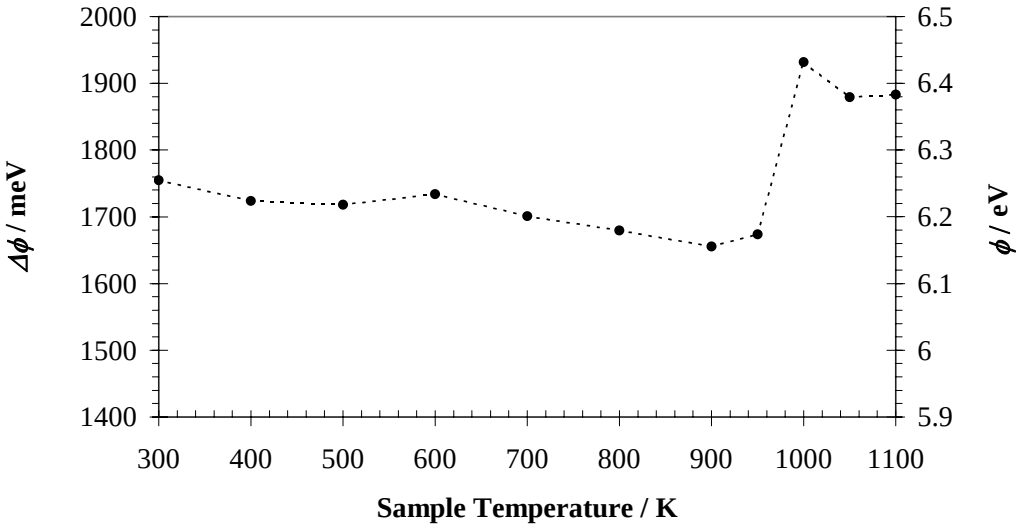

Figure 4-8. *Saturation values of the work function increase of the oxidised polycrystalline Mo surface at different temperatures where the clean surface exhibits a work function of 4.50eV.*

C. Rhenium

As pointed out in section 4.2.1, rhenium is considered as one of the most favourable target materials for the p-HSI application. It was therefore the subject of a more detailed investigation [21].

Clean Surface Work Function

The work function of the polycrystalline Re surface was monitored during a series of flash-anneal cleans. After 6-8 cycles a stable ϕ value of (5.10 ± 0.10) eV was obtained which was attributed to the clean surface. This value could be repeatedly achieved to within 30 meV. Figure 4-9 shows a work function topography performed on the clean surface, the standard deviation in ϕ is nearly 100 meV across the sample surface. The lowest work function area corresponds to that of the highest temperature during

annealing so the ϕ variation observed may be due to differing surface structures or small amounts of contamination.

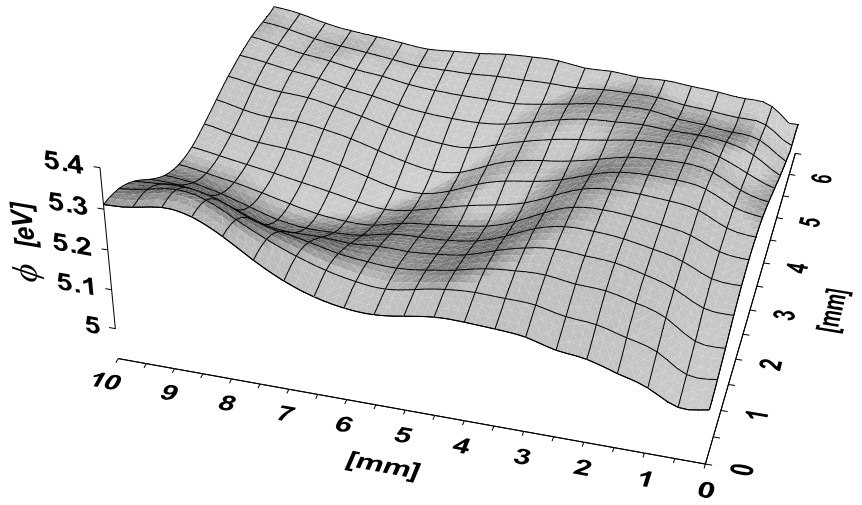

Figure 4-9*. Work function topography of the Re surface after FA cleaning.*

Work Function of the Oxidised Re Surface

Spot profile ϕ and $\Delta\phi$ data during Re oxidation at selected sample temperatures from 300K to 800K are presented in figure 4-10. The adsorption curve at 300K (**a**) clearly shows two adsorption stages, denoted by the arrows A, B and C, with a fairly abrupt transition at approx. 100L. Assuming that no depolarisation occurs we can interpret the initial rapid uptake AB as the formation of the first monolayer on identical highly reactive sites. This is followed by a slower reaction phase involving a group of less energetic sites once all the initial sites are filled. Saturation of all sites is achieved at approx. 2×10^4 L and the oxidised surface is stable to further oxygen exposure. At elevated temperatures, the gradient of the $\Delta\phi$ data with $ln(O_2$ dose) is continuous around point B achieving a total change of 1950meV at 800K. The work function topography of the oxidised Re surface, see figure 4-11, shows a flat ϕ profile indicating a homogeneous oxide coverage.

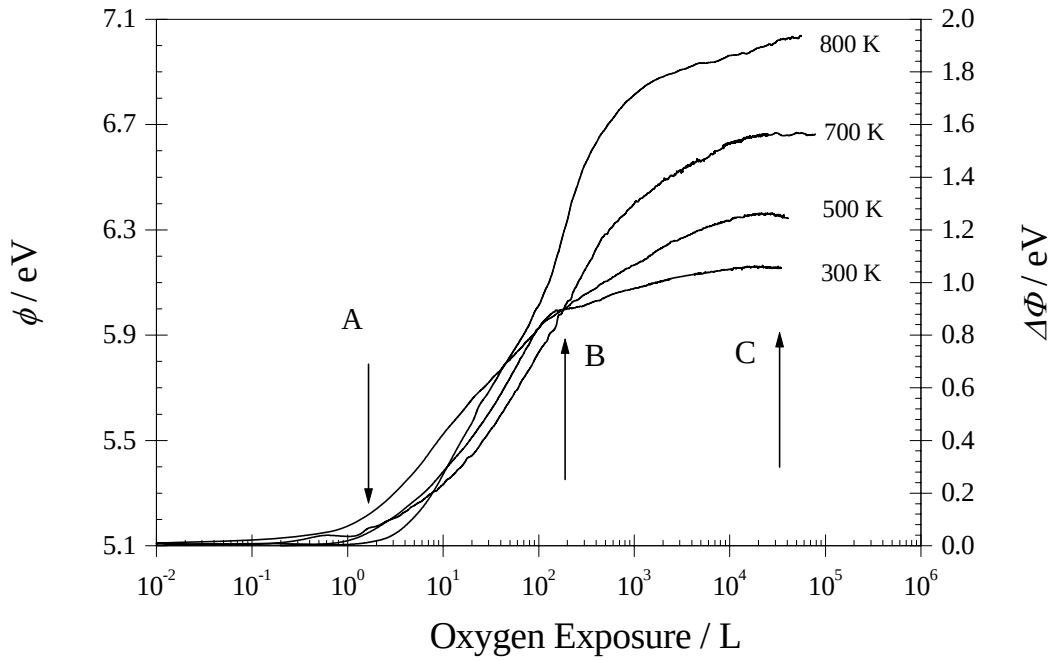

***Figure 4-10**. Work function change during Re oxidation. Curves 'a' – 'd' correspond to substrate temperatures 300, 500, 700 and 800K.*

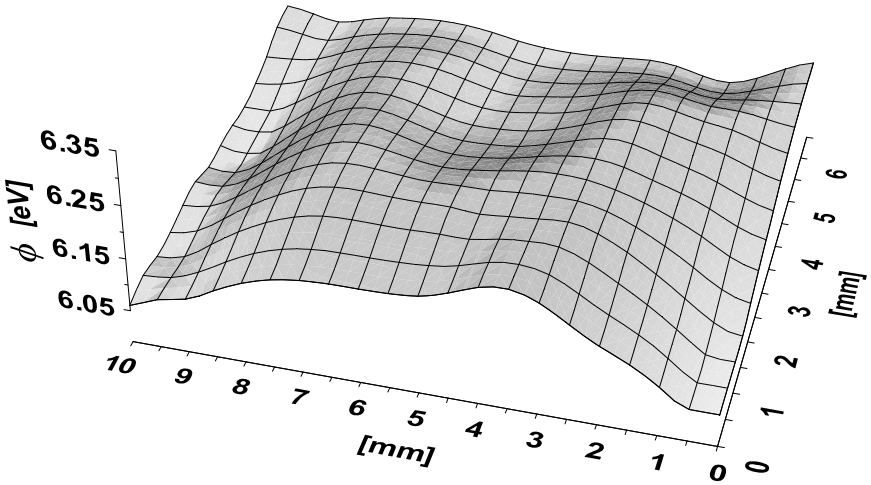

***Figure 4-11**. Work function topography of the oxidised Re surface at 300K.*

The maximum work functions obtained at the various temperatures are plotted in figure 4-12. We find an almost linear relation between ϕ and T_S up to approximately 900K which is given by:

$$\phi = 0.0016\ eVK^{-1} + 5.735\ eV \quad . \qquad 4\text{–}4$$

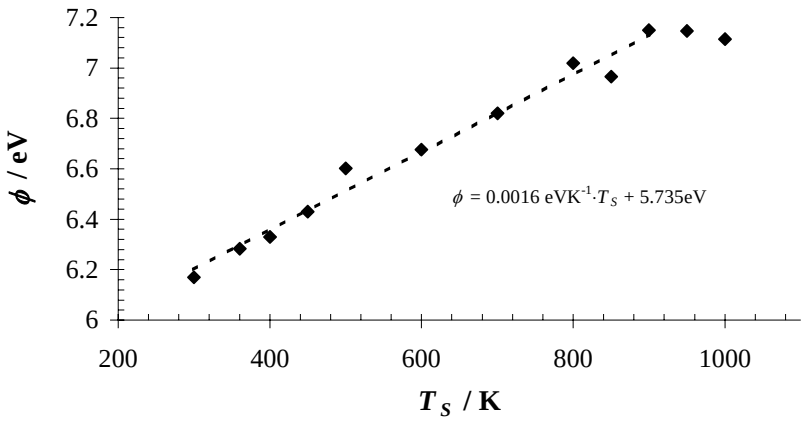

Figure 4-12.*The work function of the oxidised Re surface as a function of substrate temperature T_S where the dotted line is a linear least square fit of the data in the range from 300K to 900K.*

A maximum work function change of 2.05eV can be observed at around 900K which corresponds to an absolute work function of 7.15eV. It is considered that, as the oxidation temperature is raised, more oxygen promotes to on-top sites of the surface without being desorbed, leading to a higher overall net dipole moment and hence a higher work function [22]. At lower temperatures the oxygen penetrates to layers underneath the surface thus resulting in a lower work function.

Effect of Hydrogen Pre-Adsorption at 300 K

In the HSI application the sample gas is typically mixed with molecular hydrogen and then injected through a nozzle to create a supersonic molecular beam. As H_2 forms the bulk of the inlet gas composition and thus will be the largest residual gas component, the interaction of the H_2 on the clean Re surface was investigated. Figure 4-13, curve 'b', shows $\Delta\phi$ data recorded during oxidation of a Re surface that has been pre-exposed to 630L of H_2, which produced a small, i.e. 30meV decrease in ϕ and therefore has only a weak effect. The uptake curve is similar to that of the clean surface, but shifted downwards by some 250meV and the final surface is not stable, indicated by a decreasing ϕ with additional oxygen exposure.

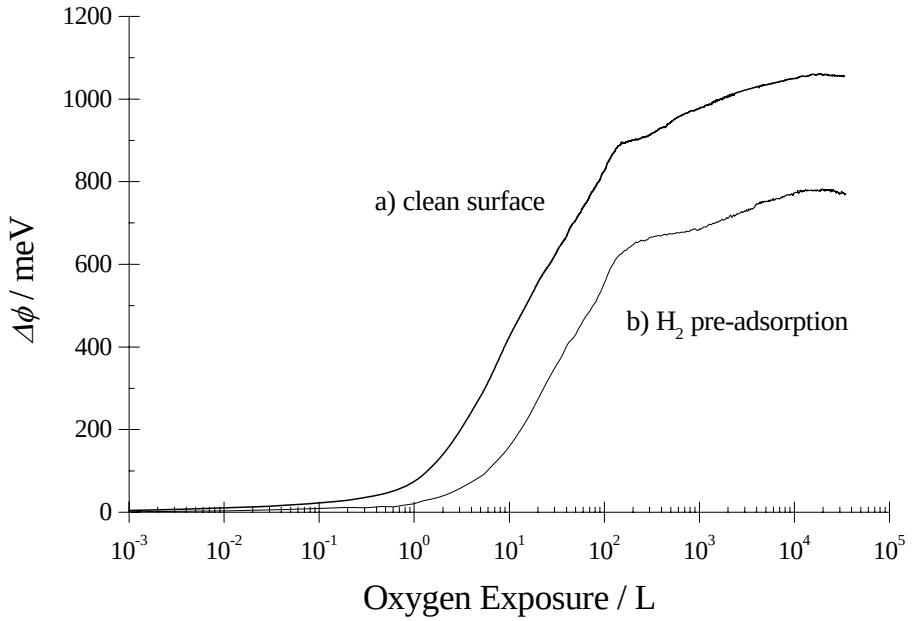

Figure 4-13*. Work function increase during oxidation of (**a**) the clean Re surface and (**b**) after pre-adsorption of 630L H_2 at 300K.*

Comparison between Surface Cleaning Methods

The oxygen uptake curves are very sensitive to the sample preparation and cleaning method applied. Figure 4-14 shows $\Delta\phi$ data for 300K and 700K oxidations using Flash-Anneal (FA) and Sputter-Anneal (SA) cleans as described in section 4.2.2. We note that the SA procedure *includes* a terminating FA. The oxidation experiments were performed at both 300K and 700K to determine whether thermal processing would affect the outcome. The most noticeable aspect, with respect to the HSI application, is that the SA procedure *does not* produce a stable work function with increasing oxygen exposures, whereas FA does. This is almost certainly due to surface roughening by the ion beam which is not wholly annealed out during either the 1200K anneal or the short FA cycling. The temperature variation of the $\Delta\phi_{peak}$ value is similar to the FA surfaces but the oxidation process is obviously more complicated due to the range of reaction sites induced by sputtering. Subsequent to SA cleaning up to 6-10 FA cycles were required to reproduce the clean Re work function value.

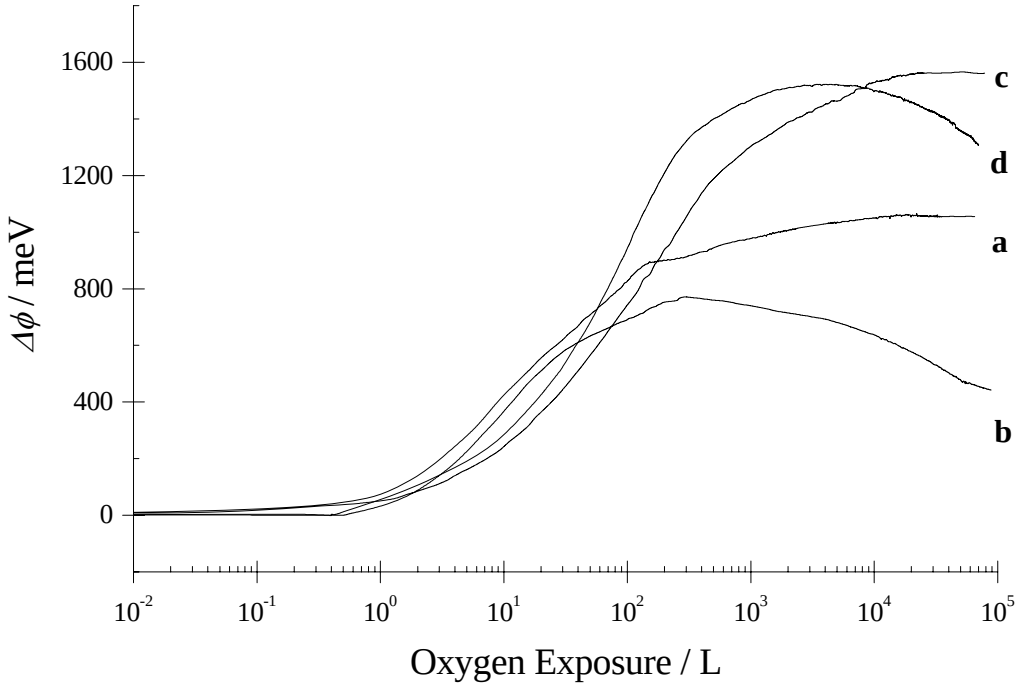

***Figure 4-14**. Effect of the cleaning procedure on the work function change during oxidation: 'a', 'c' after FA clean at 300K and 700K, respectively and 'b', 'd' after SA clean at 300K and 700K, respectively.*

D. Palladium

The clean Pd surface, obtained after several flash-anneal cycles up to 1300K, produced a work function of (5.20 ± 0.10) eV. The saturation work function of the oxidised surface as a function of the sample temperature is illustrated in figure 4-15. The curve shows a fairly constant $\Delta\phi$ of ≈ 750meV in the temperature range up to 650K. However, at higher temperatures the Pd sample exhibits a rather irregular dependence of ϕ upon T_S. At temperatures > 900K the work function decreases down to the value of ϕ of the clean Pd surface at 1000K. This indicates that the sample temperature is sufficiently hot for oxygen to desorb from the surface. The main features of this $\Delta\phi$ vs. T_S plot are in excellent agreement with a work function study by He et al. [9], reporting on the interaction of oxygen with a single crystal Pd(110) surface.

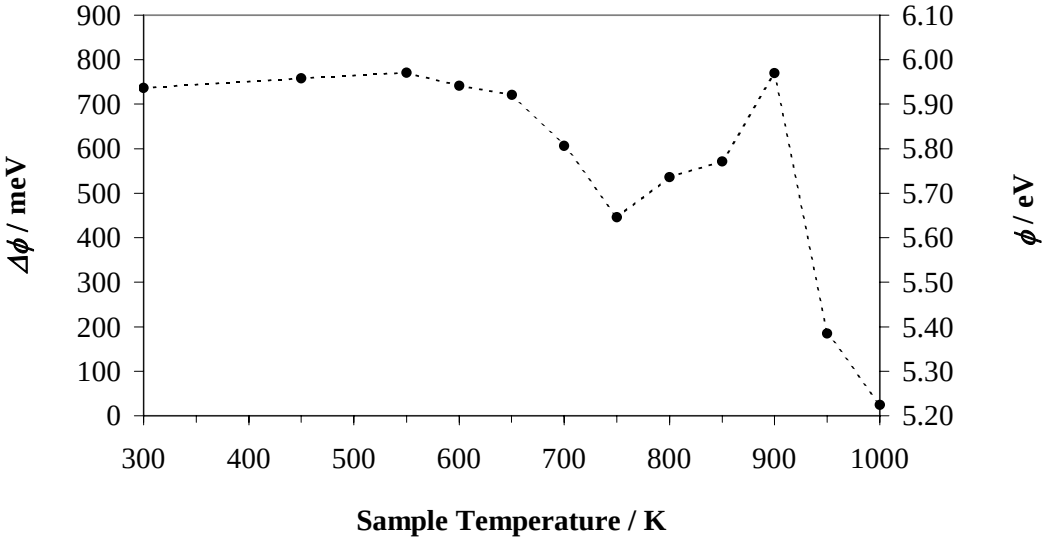

Figure 4-15. *Work function change $\Delta\phi$ as function of the Pd sample temperature with ϕ = 5.2 eV of the clean surface at 300K.*

The investigation also showed a strong dependence of ϕ on the equilibrium oxygen pressure: the formation of the oxide takes place only at the relatively high O_2 pressure used here, i.e. at ~1×10^{-5} Torr, where a stable work function is observed in the range from 300K to 550K. However, with decreasing gas pressure down to ~1×10^{-7} Torr, the work function decreased by ≈200meV at 300K and by ≈450meV at 900K. Subsequent increase in O_2 pressure to ~1×10^{-5} Torr causes a re-oxidation of the surface resulting in the re-establishment of the previous work function value. This effect has been linked to the reversible formation of a subsurface oxygen species [23].

E. Platinum

Polycrystalline platinum (Pt) produced the highest work function value of the clean surface of all the investigated metals at (5.70 ± 0.10) eV. The sample was flashed to temperatures up to 1500K for surface cleaning. Figure 4-16 shows the saturation work function values versus sample temperature of the oxidised Pt surface: a decrease in work function is observed in the lower temperature region between 300K and 500K achieving a minimum $\Delta\phi$ of -900meV at 500K. This is followed by a rapid work function increase at temperatures ≥ 550K, peaking at a $\Delta\phi$ of 650meV at ≈750K. The work function decrease reported here, at $(300 \leq T \leq 500)$K, is in contrast to the behaviour of previous measurements performed on a single crystal surface Pt(111) using both Kelvin Probe [24] and photo-emission [6] techniques, however the peak ϕ values are similar. We conclude that a fairly complex initial oxidation behaviour exists during the lower temperature oxidation on the polycrystalline surface.

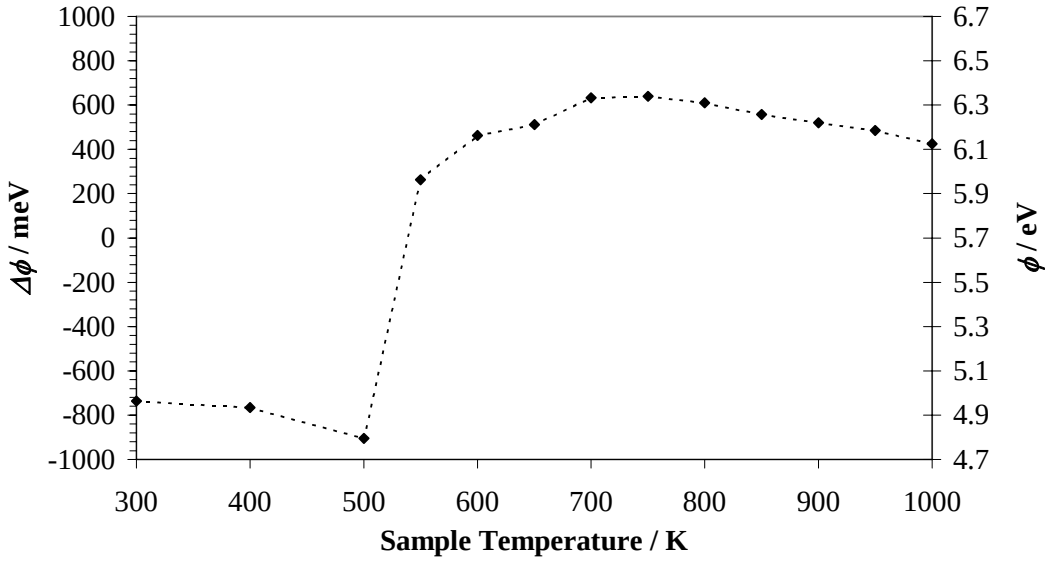

Figure 4-16. *Work function change of oxidised polycrystalline platinum with temperature where the clean Pt surface exhibits a work function of 5.70 eV.*

4.2.4 Summary of Metal Oxide Work Function Data

The maximum work function obtained for each of the investigated oxidised metal surfaces is listed in table 4-6. We find that polycrystalline Re produced upon oxidation the highest surface work function of the materials studied here of (7.15 ± 0.10) eV at a temperature of 800K. Further, Re is only weakly affected by hydrogen, which is used as a carrier gas in HSI and, moreover, the material has a relatively high melting point and is very resistant to thermal cycling. We can therefore conclude that Re is best suited as a target materials for pHSI.

***Table 4-6**: Summary of experimental results of this study: $\Delta\phi$(max) is the maximum work function increase and ϕ(max) the respective absolute value obtained at the substrate temperature T_S and an oxygen pressure of ~1×10^{-5} Torr.*

Metal	**ϕ(clean) / eV**	**$\Delta\phi$(max) / eV**	**ϕ(max) / eV**	**T_S(max) / K**
Re	5.10 ± 0.10	1.95 ± 0.05	7.05 ± 0.10	900
W	4.65 ± 0.10	1.67 ± 0.05	6.32 ± 0.10	1000
Mo	4.50 ± 0.10	1.87 ± 0.05	6.37 ± 0.10	1000
Pt	5.70 ± 0.10	0.65 ± 0.05	6.35 ± 0.10	750
Pd	5.20 ± 0.10	0.77 ± 0.05	5.97 ± 0.10	900

4.3 LOW WORK FUNCTION SURFACES

4.3.1 Discussion

As can be seen from figure 2–2, elements exhibiting low work functions, as required for n-HSI targets, are found mainly in the 1st and 2nd main group of the periodic table which are the alkali and rare earth metals, such as potassium, caesium or calcium. For the choice of materials to be considered as potential n-HSI target materials, the following additional requirements have to be met: (i) melting point above 1000K and stability with thermal cycling, (ii) low vapour pressure and (iii) stability of the work function with contamination. Most of these requirements however are incompatible with the actual properties of the elements pointed out above. The majority of these elements have rather low melting points and are highly reactive, i.e. the work function will rapidly increase when exposed to trace amounts of gases such as oxygen. This therefore imprints severe restrictions on the choice of materials. These considerations led to the selection of the following materials for this study: lanthanum hexaboride, LaB_6, calcium (Ca) and gadolinium (Gd) see table 4-7.

Table 4-7*. Work functions and melting points of the n-HSI test material.*

Material	Melting Point / °C	ϕ / eV	Reference
LaB_6	2210	2.66	[27]
Ca	839	2.87	[25]
Gd	1314	3.1	[26]

LaB_6 is used as an electron emitting material and has therefore been studied intensively [27, 28, 29]. The compound is part of a more general concept investigated by Lafferty [27] where alkali or rare earth metals, denoted by M, are embedded in a matrix of the element boron in the form MB_6. This concept has the advantage of combining the

thermal and chemical stability of the boron framework with the low work function of the metals. LaB_6 was found to have favourable properties with respect to its work function, thermal stability and chemical inertness. Further, the surface of LaB_6 can be re-activated after adsorption of gases via flash-annealing [27]. LaB_6 films can be generated either via cataphoretic coating [28] or via evaporation [30].

Calcium, belonging to the alkaline earth metals, seems to be a good compromise with respect to melting point and work function of the material. Although it readily forms a nitride layer when exposed to air [2], it should be sufficiently stable under UHV conditions and to gases at low pressures ($<1\times10^{-5}$ Torr). Ca films can be produced via evaporation.

Gadolinium is a member of the rare earth metals and, although having a work function of >3eV, has the advantage of a relatively high melting point and is available in form of thin foils. The material can therefore be cleaned when mounted in the vacuum chamber via resistive heating. Further, Gd is found to be relatively stable in air [2] and should therefore exhibit a reasonable stability with respect to its work function.

4.3.2 Experiment

A. Electron Beam Evaporation

The main features of the UHV system used for the low surface work function studies is described in chapter 3. The chamber is further equipped with a 4-pocket electron beam evaporator (Oxford Applied Research), see figure 4-17, that was utilised to generate the low work function surfaces. With this evaporation method the target material in form of rods or powder within a crucible is heated via electron bombardment. The electrons

emitted from a hot filament are accelerated towards the target with a voltage up to 2kV. With a maximum emission current of 55mA the power available to melt the material is 110W. The evaporator comprises 4 such evaporation units or 'pockets', each operated separately. Due to the electron heating current accelerated towards the target the vapour is partly ionised. This effect is used to indicate and measure the evaporation rate.

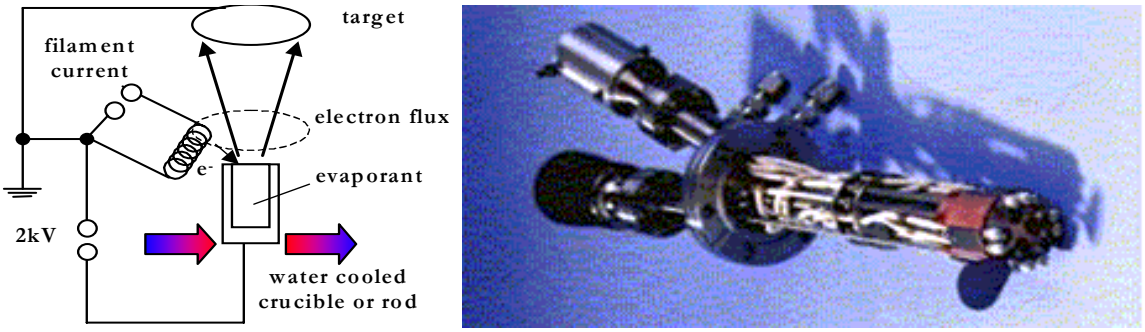

Figure 4-17. *Four pocket e- beam evaporator used to generate low work function films.*

B. Sample Preparation

LaB_6 (purity 99%, ALDRICH) and Ca (99.5%, ALFA) films were generated via e-beam evaporation onto a polycrystalline rhenium foil (25×12×0.025 mm^3, purity 99.99%, ADVENT). The foil was cleaned by repeated flash annealing to temperatures above 2000K as described in 4.2.2. The gadolinium foil (25×12×0.1 mm^3, purity 99.9%, ALFA) was cleaned first mechanically in ambient to remove the oxide film and subsequently in the UHV chamber by repeated resistive heating up to 1200K for several minutes. All samples were mounted onto the UHV sample holder via tantalum pressure contacts.

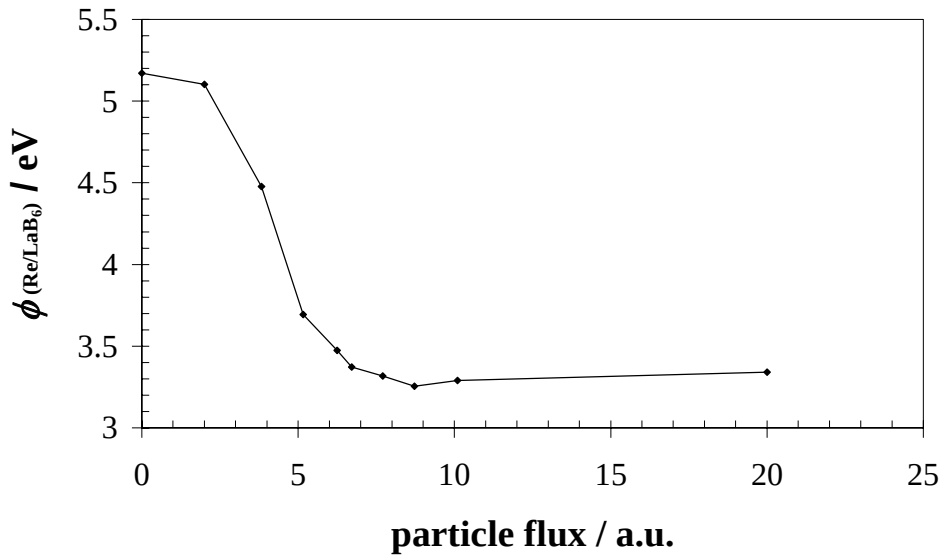

Figure 4-18. *Work function change during evaporation of LaB_6 onto a Re foil held at 300K. The current onto the sample due to the partly ionised molecular beam was used as a measure of the particle flux.*

In order to characterise the LaB_6 evaporation process, the work function change of the Re/LaB_6 system was measured at different stages of the evaporation as shown in figure 4-18. After an initial rapid decrease the work function changes only in small steps with further evaporation, gradually achieving approximately 3.3eV. However, if the surface is 'activated' by flashing it to 1500°C, a further work function decrease to 2.536eV is obtained. The necessity for such an activation procedure might be caused either by contamination or, indeed, a rearrangement of the LaB_X structure since its work function is known to depend strongly on the surface stoichiometry of the compound [29]. No such activation step was necessary for the preparation of the Ca film.

4.3.3 Results

The initial work functions determined for the surfaces, i.e. after the evaporation and activation or thermal cleaning, respectively, are listed in table 4-8. We find, within the measurement error, a good agreement between the work functions determined here and values given in the literature.

Table 4-8. *Experimentally found work functions compared to literature values.*

Material	ϕ(experiment) / eV	ϕ(literature) / eV	Reference
LaB_6	2.536±0.050	2.66	[27]
Ca	2.920 ± 0.050	2.87	[25]
Gd	3.075 ± 0.050	3.1	[26]

The work function increase due to the adsorption of residual gas molecules is shown in figure 4-19. With respect to the LaB_6 surface, we clearly observe 2 adsorption stages. The first one, marked A-B, with an almost constant gradient above 10L and the second one, after approximately 80L, with a lower and rather continuous gradient leading to a work function of 3.65eV after an exposure of 200L.

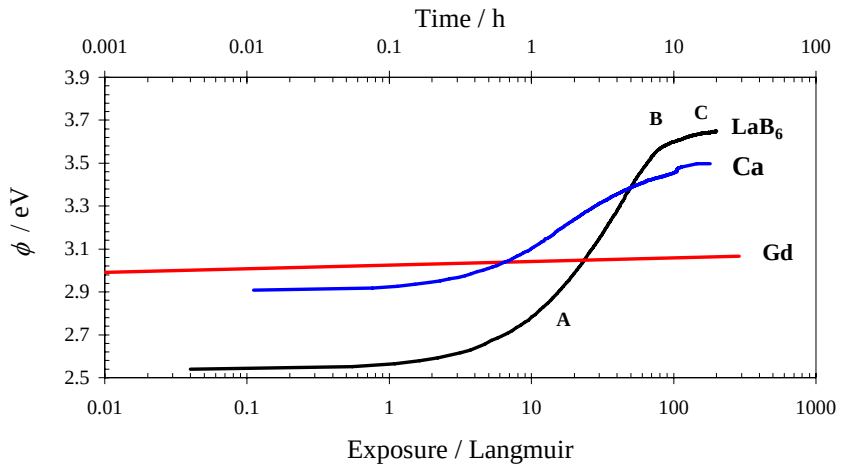

Figure 4-19*. Work function increase due to the adsorption of residual gas molecules at 300K.*

This shows that LaB_6 is rather easily poisoned at 300K by the adsorption of residual gas, the largest component of which is molecular hydrogen, see figure 4-20. In contrast, although having a higher initial work function, ϕ(Gd) increases by only 70meV after 200L exposure. Ca shows a moderate increase in ϕ of 560meV to 3.48eV after the same exposure of 200L.

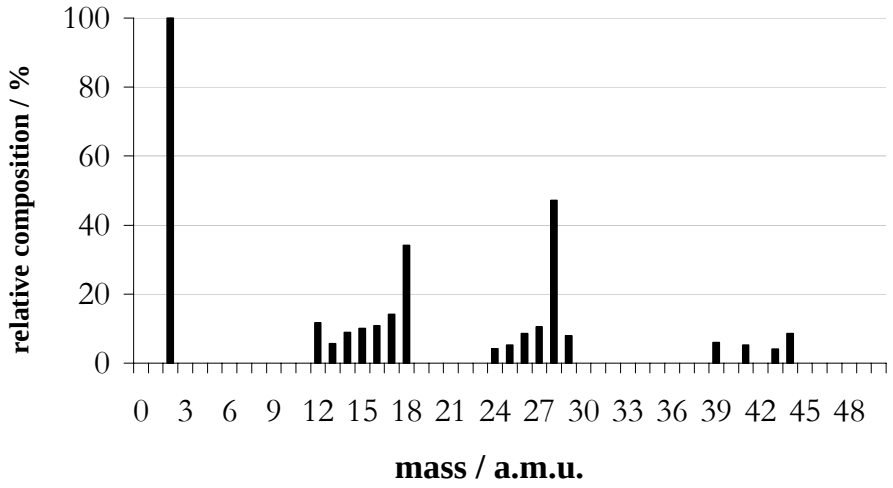

Figure 4-20. *The relative composition of the residual gas envelope at a base pressure of 3.7×10^{-9} Torr.*

The results of this study are summarised in table 4-9. We can conclude that LaB_6 has the lowest work function of the materials studied, however, it exhibits a very high sensitivity to surface contamination at 300K. Gadolinium on the other hand, has a higher initial work function but is only little affected by the adsorption of residual gas molecules.

Table 4-9. *Summary of the study of low work function surfaces.*

Material	**ϕ(initial) / eV**	**ϕ(200L) / eV**	**$\Delta\phi$ / eV**
LaB_6	2.536 ± 0.050	3.560	1.024
Ca	2.920 ± 0.050	3.480	0.560
Gd	3.075 ± 0.050	3.145	0.070

REFERENCES

1. J.C. Rivère in *Solid State Surface Science*, Vol. 1, edited by M. Green (M.Dekker, New York, 1969), p. 198-204.

2. CRC Handbook of Chemistry and Physics, 74th Ed., edited by D.R. Lide (CRC Press, Boca Baton, Fl, 1994).

3. W. Mönch, *Semiconductor Surfaces and Interfaces*, Spinger (1995) ISBN 3-540-58625-3.

4. W.D. Davis, *Environmental Science and Technology* **11**, 587 (1977).

5. E.Y. Zandberg, M.V. Knat'ko, V.I. Paleev, U.K. Rasulev, *Sov. Phy. Tech. Phys.* **29**, 1367 (1984).

6. P.R. Norton, *Surf. Sci.* **47**, 98 (1975).

7. V.P. Ivanov, G.K. Boreskov, V.I. Savchenko, Jr. and W.H. Weinberg, *Surf. Sci.* **61**, 207 (1976).

8. V.V. Gorodetskii, B.E. Nieuwenhuys, *Surf. Sci.* **105**, 299 (1981).

9. J.W. He, U. Memmert, P.R. Norton, *J. Chem. Phys.* **90**, 5088 (1989).

10. A.R. Kortan, P.I. Cohen, R.L. Park, *J.Vac. Sci. Technol.***16**, 541 (1979).

11. T.E. Madey, H.A. Engelhart, D. Menzel, *Surf. Sci.* **48**, 304 (1975).

12. W. Greaves, R.E. Stickney, *Surf. Sci.* **11**, 395 (1968).

13. B.H. Blott, and T.J. Lee, *J. Phys. Edu.* 2, 785 (1969).

14. N.A. Surplice and D.J. D'Arcy, *J. Phys. Edu.* 3, 477 (1970).

15. J. Euler, and R. Ludwig, *Arbeitsmethoden der optischen Pyrometrie* (Verlag G. Braun, Karlsruhe, 1960)

16. W.H. Press, B.P. Flannery, S.A. Teukolsky and W.T. Vetterling, *Numerical Recipes* (Cambridge University Press, 1986).

17. I.D. Baikie and P.J. Estrup, *Rev. Sci. Instrum.* **69**, 3902 (1998).

18. T.E. Maday, *Surf. Sci.* **33**, 355 (1972).

19. E. Bauer, H. Poppa, Y. Viswanath, *Surf. Sci.* **58**, 517 (1976).

20. É.Ya. Zandberg, M.V. Knat'ko, V.I. Paleev, U.K. Rasulev, *Soviet Physics - Technical Physics* **29**, 1367 (1984).

21. I.D. Baikie, U. Petermann, A. Speakman, B. Lägel, K.M. Dirscherl, P.J. Estrup, *J. Appl. Phys.* **88**, 1 (2000).

22. R. Pantel and M. Bujor, *Surf. Sci.* **83**, 228 (1979).

23. S. Ladas, S. Kennou, N. Hartmann, R. Imbihl, *Surf. Sci.* **382**, 49 (1997).

24. G.N. Derry, P.N. Ross, *J. Chem. Phys.* **82**, 2772 (1985).

25. L. Gaudart, R. Riviora, *Appl. Opt.* **10**, 2336 (1971).

26. D.E. Eastman, *Phys. Rev.* **B2**, 1 (1970).

27. J.M. Lafferty, *J. Appl. Phys.* **22**, 299 (1951).

28. L.J. Favreau, *Rev. Sci. Instrum*. **36**, 856 (1965) **38**, 841 (1967).

29. E.K. Storms, B.A. Mueller, *J. Appl. Phys.* **50**, 3691 (1979).

30. B. Lägel, I.D. Baikie, K. Dirscherl and U. Petermann in *Electron-Emissive Materials, Vacuum Microelectronics and Flat-Panel Displays*, edited by K.L. Jensen, W. Mackie, D. Temple, J. Itoh, R. Nemanich, T. Trottier, P. Holloway (Mater. Res. Soc. Proc. **621**, Pittsburgh, PA, 2000) in press.

Chapter 5

Thermal and Hyperthermal Surface Ionisation

5.1 INTRODUCTION

Hyperthermal Surface Ionisation (HSI) is a novel ionisation technique established by Danon and Amirav [1]; its characteristics make it very attractive for mass-spectrometric applications. Analytical and general applications of this technique thus include e.g. the detection of drugs [2] and explosives [3], fast gas chromatography mass spectrometry (GC-MS) [4, 5], as well as ion sources for ion guns and leak detection [2].

However, there is a lack of information about the role and the characteristics of the ionising surface: by using suitable target materials, HSI becomes extremely sensitive and the minimum detection levels are vastly improved. Therefore, a study was commissioned by the UK's Defence and Research Evaluation Agency (DERA) for the characterisation and optimisation of a novel ion source based on HSI. The study presented in chapter 4 is dedicated to the generation and characterisation of high and low work function target surfaces.

In order to evaluate these surfaces with respect to their suitability as HSI targets and to characterise the ionisation process, a specially designed gas inlet system was implemented comprising a gas mixture chamber and a pulsed nozzle gas inlet valve. As part of this ongoing project leading to an optimised HSI mass spectrometer system, we discuss in this chapter the principles underlying thermal and hyperthermal surface ionisation, SI and HSI, respectively. A simple model will be developed to characterise the process of SI and estimate its ionisation efficiency. The principle of HSI and its advantages compared to SI are discussed. Further, the conditions for the generation of

hyperthermal molecular beams and its properties are described. Experimental data are presented demonstrating the generation of positive and negative ions via SI and HSI, respectively.

5.2 THERMAL SURFACE IONISATION

5.2.1 Degree of Ionisation

If a solid surface at absolute temperature T_S is in equilibrium with an elemental gas with ionisation potential I_g, the Saha equation of the system is given by [6]

$$\frac{n_+ n_e}{n_0} = \frac{g_+ g_e}{g_0} \cdot \left(\frac{2\pi mkT}{h^2} \right)^{\frac{3}{2}} \cdot \mathrm{e}^{\frac{-I_g}{kT_S}}, \qquad 5\text{–}1$$

where n_+, n_e and n_0 and g_+, g_e and g_0 are the densities and statistical weights of positive ions, electrons and neutrals, respectively. The mass of the gas molecules is denoted by m; k and h are Boltzmann's and Plank's constant, respectively. For simplicity, reflection coefficients are not considered in the equation above. Equation 5–1 expresses the probability that the gas adsorbed on the solid may vaporise from the surface as neutral molecules or as positively charged ions. Similarly, for molecules desorbing as negative ions, the Saha equation can be given by

$$\frac{n_- n_e}{n_0} = \frac{g_- g_e}{g_0} \cdot \left(\frac{2\pi mkT}{h^2} \right)^{\frac{3}{2}} \cdot \mathrm{e}^{\frac{\chi_g}{kT_S}}, \qquad 5\text{-}2$$

where n_- and g_- is the density and the statistical weight of the negative ion and χ_g the electron affinity of the neutral gas molecule. The electron density n_e at a metal surface with a work function ϕ_S is given by Fowler as [7]

$$n_e = g_e \cdot \left(\frac{2\pi mkT}{h^2} \right)^{\frac{3}{2}} \cdot \mathrm{e}^{\frac{-\phi_S}{kT_S}} . \qquad 5\text{-}3$$

The degree of ionisation $\alpha_{\pm}$ is defined as the ratio of positive (negative) ions to the sum of all other species at the surface, i.e. neutrals and negative (positive) ions:

$$\alpha_{\pm} = \frac{n_{\pm}}{n_0 + n_{\mp}} . \qquad 5\text{-}4$$

Combining equations 5–1 to 5-4, α can be expressed by:

$$\alpha_{+} = \frac{g_{+}}{g_0} \cdot \mathrm{e}^{\frac{\phi_S - I_g}{kT}} \left[1 + \frac{g_{-}}{g_0} \cdot \mathrm{e}^{\frac{\chi_g - \phi_S}{kT_S}} \right]^{-1} \qquad 5\text{-}5$$

for the formation of positive ions and for negative surface ionisation by

$$\alpha_{-} = \frac{g_{-}}{g_0} \cdot \mathrm{e}^{\frac{\chi_g - \phi_S}{kT}} \left[1 + \frac{g_{+}}{g_0} \cdot \mathrm{e}^{\frac{\phi_S - I_g}{kT_S}} \right]^{-1} . \qquad 5\text{-}6$$

From these equations it can be seen that the work function of the surface is a main parameter determining the degree of ionisation of the particles leaving the surface. Indeed, surface ionisation can be used as a method to measure the surface work function, see e.g. §2.4.2. Gases having a low ionisation potential adsorbed on high work function surfaces produce mainly positive ions (p-SI) whereas gases having a high electron affinity adsorbed on low work function surfaces preferably create negative ions (n-SI) as depicted schematically in figure 5-1. Thus, for these cases, the degree of ionisation can be approximated by

$$\alpha_{\pm} = \frac{n_{\pm}}{n_0} . \qquad 5\text{-}7$$

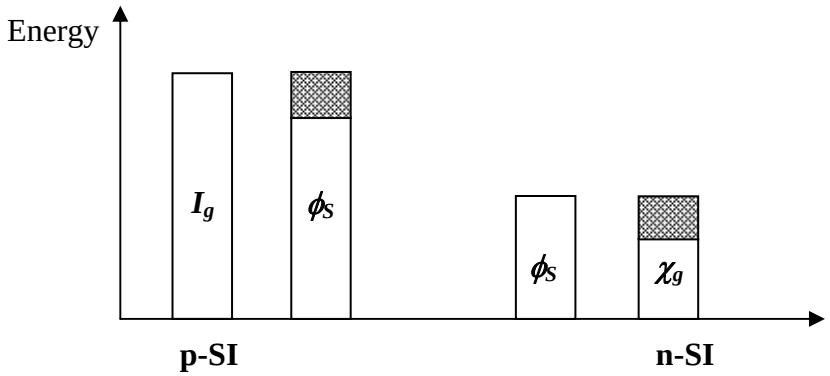

Figure 5-1. *Energetic balances for positive (p-SI) and negative (n-SI) surface ionisation where I_g and χ_g are the ionisation potential and the electron affinity of the gas and ϕ_S is the work function of the ionising surface. The patterned areas symbolise the differences between the respective quantities causing a reduction in the ionisation efficiency.*

Consequently, equations 5-5 and 5-6 reduce to [6]:

$$\alpha_+ = \frac{g_+}{g_0} \cdot \mathrm{e}^{\frac{\phi_S - I_g}{kT_S}} \qquad 5\text{-}8$$

and

$$\alpha_- = \frac{g_-}{g_0} \cdot \mathrm{e}^{\frac{\chi_g - \phi_S}{kT_S}}, \qquad 5\text{-}9$$

respectively. Expressions 5-8 and 5-9 are also termed the Saha-Langmuir equations. Comprising the pre-exponential factors in the above equations into a factor $C_\pm$ we obtain the equations for the surface ionisation given in §2.4.2, i.e.:

$$\alpha_+ = C_+ \cdot \mathrm{e}^{\frac{\phi_S - I_g}{kT_S}} \qquad 5\text{-}10$$

and

$$\alpha_- = C_- \cdot \mathrm{e}^{\frac{\chi_g - \phi_S}{kT_S}}. \qquad 5\text{-}11$$

5.2.2 Ionisation Efficiency

A. Definition of the Ionisation Efficiency

The ionisation efficiency β is defined as the ratio of ions n to the total number of particles N leaving the surface, i.e.

$$\beta_{\pm} = \frac{n_{\pm}}{N_{\pm}}, \qquad 5\text{-}12$$

where $N_{\pm}$ is given by

$$N_{\pm} = n_0 + n_{\pm}, \qquad 5\text{-}13$$

with n_0 denoting the number of neutral atoms and the subscripts '+' and '–' positive and negative ionisation, respectively. Using equation 5-7 we can thus rewrite expression 5-12 as

$$\beta_{\pm} = \left[1 + \frac{1}{\alpha_{\pm}}\right]^{-1}. \qquad 5\text{-}14$$

Inserting equations 5-8 and 5-9 into 5-14, the efficiency for positive surface ionisation can be expressed as

$$\beta_{+} = \left[1 + \frac{g_0}{g_{+}} \cdot \mathrm{e}^{\frac{I_g - \phi_S}{kT_S}}\right]^{-1} \qquad 5\text{-}15$$

and for negative ionisation by

$$\beta_{-} = \left[1 + \frac{g_0}{g_{-}} \cdot \mathrm{e}^{\frac{\phi_S - \chi_g}{kT_S}}\right]^{-1}. \qquad 5\text{-}16$$

Under steady state conditions, the number of particles leaving the target surface is equal to the number of particles hitting that surface. Therefore, β can also be expressed by

$$\beta_{\pm} = \frac{I_{\pm}}{q_{mol} \cdot q}, \qquad 5\text{-}17$$

where $I_{\pm}$ is the current of ions evaporating from the ionising surface, q_{mol} the flux of molecules hitting that surface and q the elementary charge. If the ions produced at the target surface are collected via an electrode close to the surface, the measured ion current I_{coll} can be related to the total ion current I by

$$I_{coll} = \gamma_{coll} I \qquad 5\text{-}18$$

where γ_{coll} denotes the collection efficiency of the measurement system.

B. Molecular Beam Flux

In order to estimate the current of ions generated at the target surface, according to equation 5-17, the flux of molecules, q_{mol}, needs to be known. If the molecules are injected towards the surface through a nozzle having an aperture of area A_{nozzle}, the throughput of molecules through the nozzle is given by

$$q_{mol} = A_{nozzle} \cdot R, \qquad 5\text{-}19$$

where R is the impact rate of molecules onto A_{nozzle}. The impact rate of molecules with molecular mass M at the pressure p_0 and absolute temperature T_0 in the gas inlet system is given by [12]

$$R = p_0 \sqrt{\frac{N_a}{2\pi M k T_0}}, \qquad 5\text{-}20$$

where N_a is Avogadro's number. Thus the flux of molecules through the nozzle is

$$q_{mol} = A_{nozzle} \cdot p_0 \sqrt{\frac{N_a}{2\pi MkT_0}} \,. \qquad 5\text{-}21$$

For example, the flux of molecules of the gas nitrogen dioxide, NO_2, which was used as a model gas for the ionisation experiments, as a function of the gas inlet pressure p_0 is given in figure 5-2. The gas is injected at a temperature of T_0 = 300K through the pulsed nozzle valve (PNV) of the gas inlet system having an aperture diameter of 0.5mm. The molecular mass of NO_2 is 46.01 g·mol^{-1}.

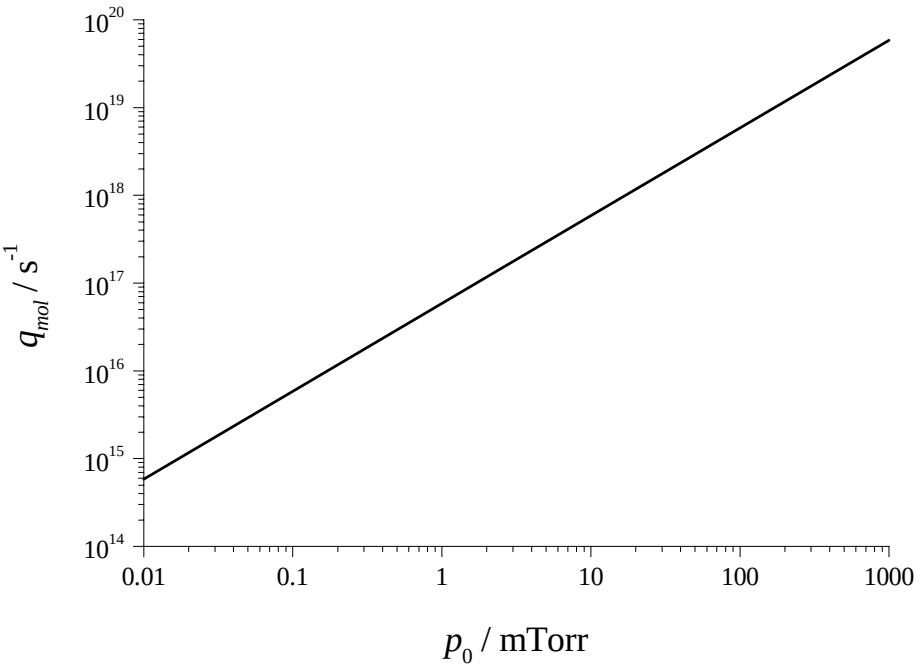

***Figure 5-2**. Flux of NO_2 molecules through the nozzle of the PNV as a function of inlet pressure at 300K.*

C. Simulation of the Ionisation Efficiency and Ion Current for NO_2

As an example we calculate the ionisation efficiency for NO_2 and the resulting ion current using the equations derived above. We assume that the flux of molecules q_{mol} flowing trough the inlet nozzle equals the flux hitting the ionising target surface. For an inlet pressure of $p_0 = 500\text{mTorr}$ at the temperature $T_0 = 300\text{K}$, according to equation 5-21, the flux of molecules hitting that surface is $q_{mol} = 2.9\times10^{19}$ molecules·s^{-1}, see also figure 5-2. For the estimation of the positive surface ionisation we further assume an ionisation potential for NO_2 of $I_g = 9.75\text{eV}$ [8] and a work function of the oxidised Re target surface according to

$$\phi_S = 0.00168\frac{eV}{K}\cdot T_S + 5.735eV \qquad 5\text{-}22$$

for a range of $300\text{K} \le T_S \le 800\text{K}$ and assume 7.15eV for $T_S > 800\text{K}$, see chapter 4. The ionisation efficiency and the resulting ion current under these conditions are plotted as a function of the target surface temperature T_S in Figure 5-3 according to equation 5-15.

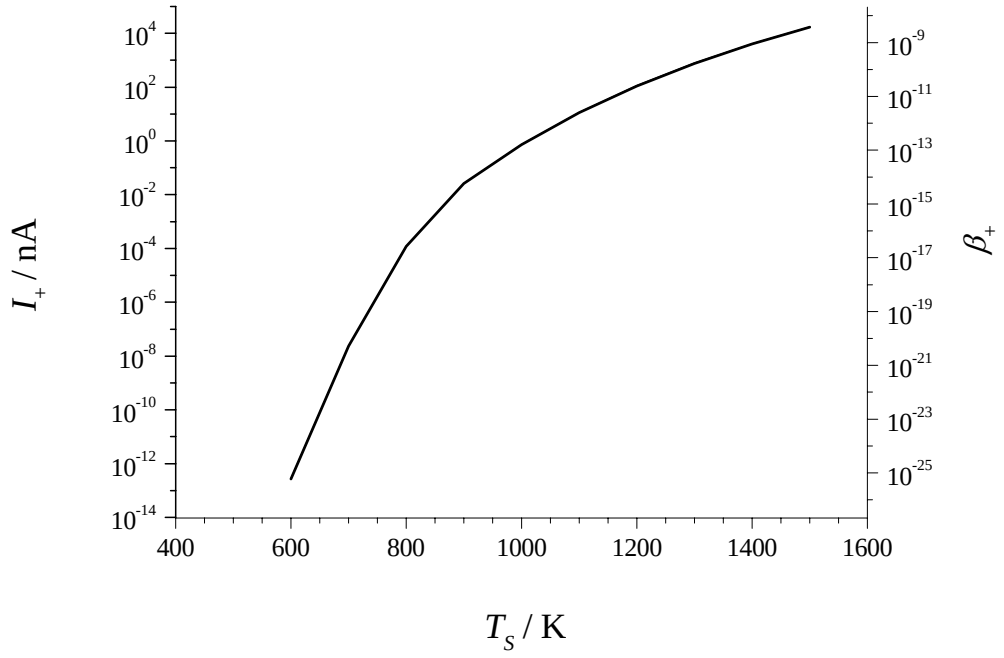

***Figure 5-3**. Current and ionisation efficiency for positive surface ionisation of NO_2 on oxidised Re calculated under the assumptions made above.*

We see that because of the relatively large energetic difference of 2.65eV between the ionisation potential of NO_2 and the Re target work function the ionisation efficiency and the resulting ion current at temperatures below 900K is very low. However, with increasing temperature the work function of the Re surface increases and the exponent in equation 5-15 decreases. Thus, at a target temperature of 1000K and above the ion current is >0.1nA and would therefore be in the measurable range of the ion collector.

For the simulation of negative surface ionisation, plotted in figure 5-4 according to equation 5-16, we assume an electron affinity for NO_2 of χ_g = 2.3eV [9] and a target work function of the LaB_6 surface of 2.54eV, see chapter 4. Since the difference between the electron affinity of NO_2 and the work function of the LaB_6 target surface is now only 0.24eV, the calculated efficiency of the ionisation is considerable higher than for positive surface ionisation. However, in practice the exposure of the LaB_6 surface to the strongly oxidising gas NO_2 increases the work function of the target surface significantly, see chapter 4. Therefore, the ionisation efficiency achieved experimentally can be expected to be lower by several orders of magnitude.

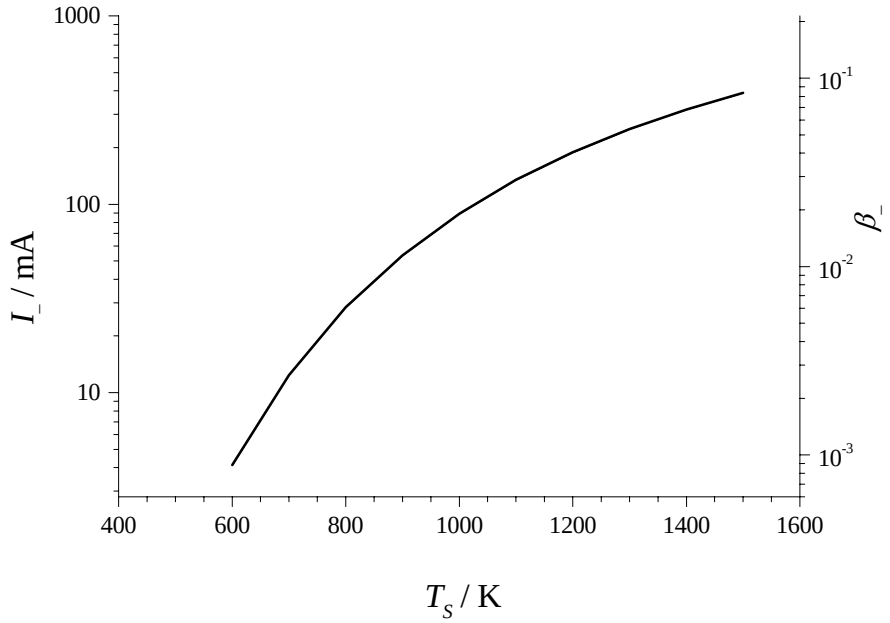

***Figure 5-4**. Current and the ionisation efficiency for negative surface ionisation of NO_2 on LaB_6 calculated under the assumptions made above.*

5.3 HYPERTHERMAL SURFACE IONISATION

5.3.1 Phenomenological Description

Although surface ionisation is a well-known and established phenomenon it is practically restricted to only a few elements, such as alkali metals having a very low ionisation potential I_g or halogens having a high electron affinity χ_g. The ion yield obtained via thermal surface ionisation depends exponentially on the difference between the surface work function ϕ_S and I_g or χ_g and hence becomes negligible if $\phi_S < I_g$ or $\phi_S > \chi_g$. However, experiments have shown that the kinetic energy of the molecule to be ionised can effectively bridge the energy gap between ϕ_S and I_g or χ_g thus making this technique viable to a much broader range of molecules [10]. A molecular beam carrying kinetic energy above the thermal energy of the system is termed 'hyperthermal' and the surface ionisation of such molecules is called hyperthermal surface ionisation (HSI).

The Saha-Langmuir equation giving the ionisation ratio is valid only under steady state conditions. This is however not the case for HSI where the ionisation process is realised under thermal non-equilibrium conditions. Therefore, the principle of this technique will be discussed here qualitatively by means of the potential energy curve diagram commonly used for this purpose.

In HSI the species to be ionised is accelerated in a supersonic molecular beam to energies in the range (1-20)eV towards the target surface. The energy curve of the neutral species when it approaches the surface is shown in figure 5-5 (a). At a large distance *z* from the surface the molecule is weakly attracted by the surface due to the van der Waals force whereas at distances close to the surface a strong repulsive force arises due to the deformation of the electronic orbitals. Curve b shows the potential energy of the negatively ionised species. At a large distance *z* from the surface the two

energy curves, a and b, are separated by the amount $\Delta E = \phi_S - \chi_g$, which equals the energy required to transfer an electron from the Fermi level of the metal surface to the molecule. The energy level of the ion close to the surface is shifted down due to the image force interaction, see e.g. chapter 2, turning into the strong repulsive force even closer to the surface as described above. Therefore, at the distance Z_C to the target surface denoting the crossing point of the two curves, a neutral molecule can be turned into an ion and vice versa via an electron transfer between the molecule and the target surface without requiring additional energy. Z_C is given by [11]

$$Z_C = \frac{q^2}{4(\phi_S - \chi_g)}. \qquad 5\text{-}23$$

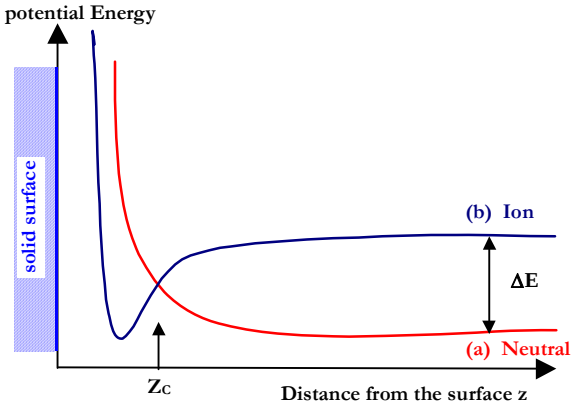

***Figure 5-5**. The potential energy curve picturing the interaction of (a) a neutral molecule and (b) a negative ion with a metal surface.*

The probability for this electron transfer process is discussed e.g. in [11]. According to this model, the kinetic energy of the molecule is required (i) to allow the molecule to approach the surface to a distance closer than Z_c and (ii) to escape the image potential well of the ionised molecule. In analogy, the difference in the energy curves between a neutral molecule and its positively ionised counterpart far away from the surface is $\Delta E = I_g - \phi_S$ and Z_C is given by [11]

$$Z_C = \frac{q^2}{4(I_g - \phi_S)}. \qquad 5\text{-}24\ .$$

5.3.2 Hyperthermal Molecular Beam Generation

A molecular beam is a stream of collision-free molecules which can be obtained e.g. when a gas expands through an orifice from a high pressure into a low pressure region. The mean free path of the molecules in the region of the nozzle determines whether an effusive or a hyperthermal beam will be produced. The mean free path of a molecule λ is given by [12]

$$\lambda = \frac{kT}{\sqrt{2}\pi\sigma^2 p}, \qquad 5\text{-}25$$

where k is Boltzmann's constant, T the absolute temperature, p the gas pressure and σ the molecular diameter, see table 5-1.

Table 5-1*. Collision cross sections for a selection of gases after [13].*

Gas	$\pi\sigma^2 \times 10^{-19}$ / **m**^{2}
He	2.05
H_2	2.69
N_2	4.26
CO_2	5.02

In an effusive beam the molecules have independent dynamic properties and no collisions occur in the region of the nozzle, i.e. $\lambda >> D$, where D is the diameter of the nozzle. A hyperthermal beam is formed when the gas molecules undergo many collisions as they travel through the nozzle, i.e. $\lambda << D$. These collision force the gas molecules mainly into the direction of the expansion z. Therefore, the velocity distribution of the molecules becomes non-isotropic and a large portion of the

translational enthalpy of the gas is converted into kinetic energy in the direction of the expansion E_z [14]. This process is also called aerodynamic acceleration.

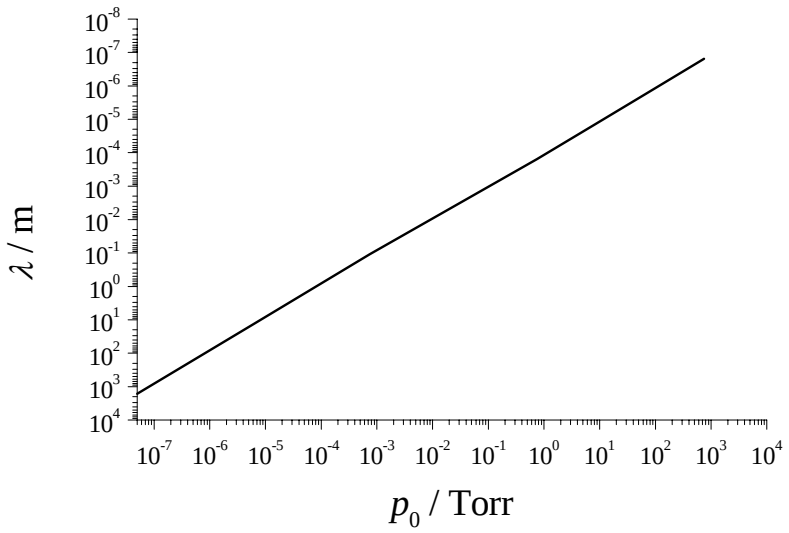

Figure 5-6*. Mean free path of hydrogen molecules at different pressures.*

The maximum or 'terminal' velocity of the molecules in the direction *z*, v_z^{∞}, is therefore given by [14]

$$v_z^{\infty} = \sqrt{\frac{kT_0}{m}\left(\frac{2\gamma}{\gamma - 1}\right)} \qquad 5\text{-}26$$

where T_0 is the temperature of the gas before the expansion. γ, the ratio of the specific heat capacities of the gas, can be expressed in terms of the degrees of freedom f of the gas molecules as

$$\gamma = \frac{f + 2}{f} \qquad 5\text{-}27$$

For a monatomic gas with $f = 3$, the maximum kinetic energy in z is then given by

$$E_z^{\infty} = \frac{5}{2} kT_0 . \qquad .5\text{-}28$$

We see that the kinetic energy of the molecules only depends on the temperature of the gas on the inlet side, see figure 5-7. Thus, E_z^{∞} can be increased by increasing T_0 which

is typically achieved by heating the gas inlet nozzle. A design of such a heatable nozzle as described in [16] is shown in figure 5-8.

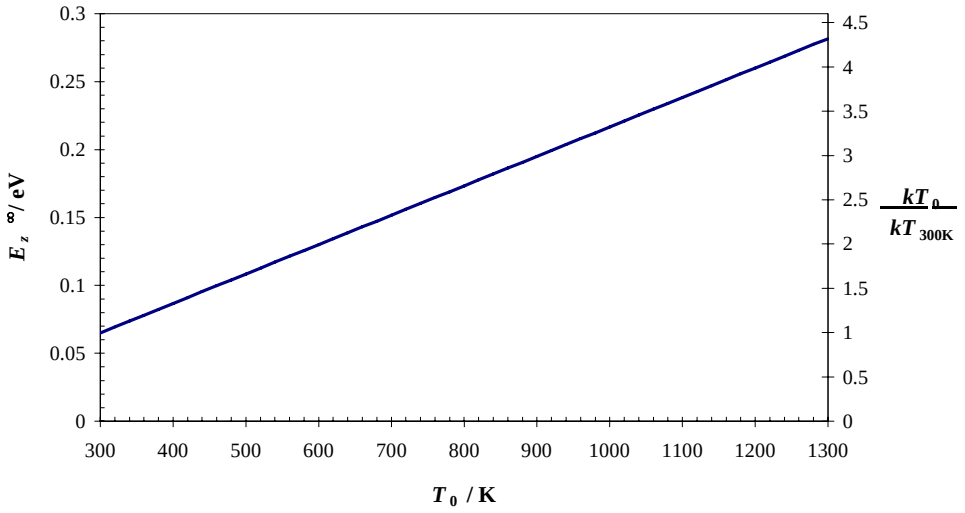

Figure 5-7. *Maximum kinetic energy of a hyperthermal beam in the direction of expansion with the factor kT_0 / kT_{300K} denoting the energy gain by increasing the temperature relative to $T_0 = 300K$.*

Since this process needs numerous collisions between the molecules, the actual velocity v_z asymptotically approaches the terminal velocity v_z^{∞} and reaches approximately 98% of v_z^{∞} at a distance $z = 5 \cdot D$ for a monatomic gas, where D is the nozzle diameter [14]. When the gas expands further into the low pressure region the collision rate drops. At a certain distance from the nozzle the collisions effectively stop and the velocity distribution is 'frozen', i.e. the molecules keep their supersonic velocities in the direction of the expansion.

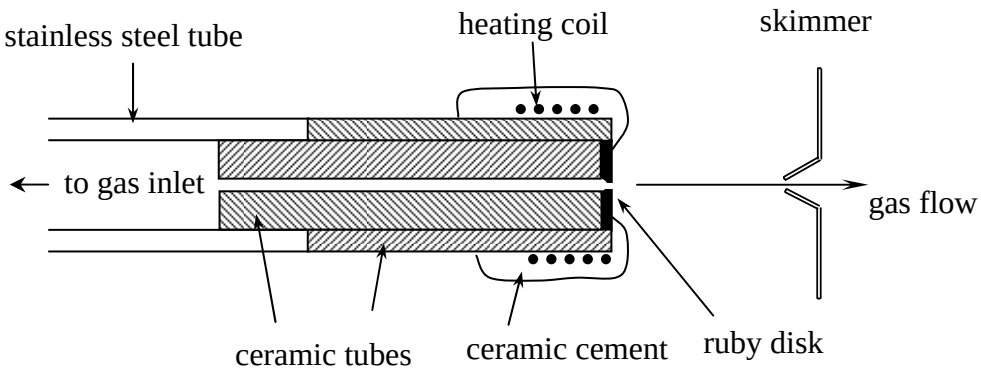

Figure 5-8. *Design of a heatable supersonic nozzle after [16].*

From the discussion above we see that relative high pressures in the nozzle region are necessary to obtain hyperthermal molecular beams. For instance, assuming a nozzle diameter of 0.5mm, to fulfil $\lambda << D$ the pressure p_0 should be >10Torr, see figure 5-6. Therefore, for mass-spectroscopic applications where only trace amounts of certain gases are sampled, the gas to be analysed is diluted in a carrier gas. With respect to the free jet expansion, this has further the advantage that higher kinetic energies of the sample gas can be achieved if the carrier gas has a very low molecular weight M_l such as hydrogen or helium. This is known as the so-called 'seeded' beam technique [15]. The gas molecules to be analysed having a molecular weight $M_h > M_l$ thereby obtain approximately the velocity of the light carrier gas due to the collisions during the expansion. Since the kinetic energy is proportional to the mass of the molecules, an effective energy amplification is achieved which equals the ratio of the mass of the molecules to be analysed to the mass of the carrier gas molecules, M_h / M_l [14, 16]:

$$E_z^{\infty} = \frac{5}{2}\frac{M_h}{M_l}kT_0. \qquad 5\text{-}29$$

Additionally, for polyatomic molecules a relaxation of vibrational and rotational energy into translational energy may occur thus increasing E_z^{∞} by further multiples of $\frac{1}{2}kT_0$, see e.g. [17]. The effect of the gas inlet temperature T_0 on the kinetic energy of hyperthermal gas molecules of mass M_h = 100 a.m.u. is plotted in figure 5-10. We see that considerable kinetic energies can be achieved using both the seeding effect described above and the thermal energy increase. For instance, an increase in T_0 from 300K to a moderate 600K effectively doubles the kinetic energy: E_z^{∞} for a gas with M_h = 100 a.m.u. seeded in He increases from 1.625eV to 3.25eV and, if seeded in H_2, from 3.25eV to 6.5eV.

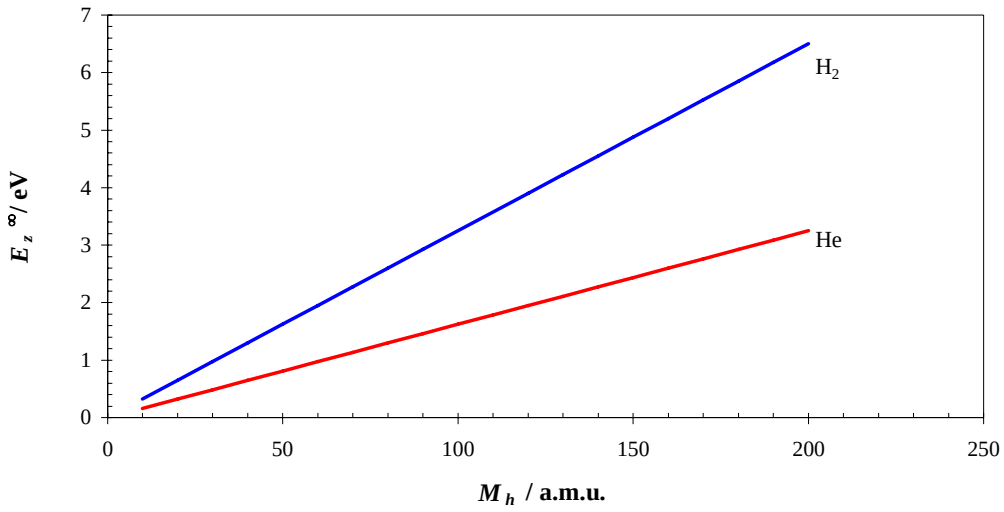

***Figure 5-9**. Maximum kinetic energy of gas molecules in the direction of expansion with mass M_h seeded in H_2 or He at 300K.*

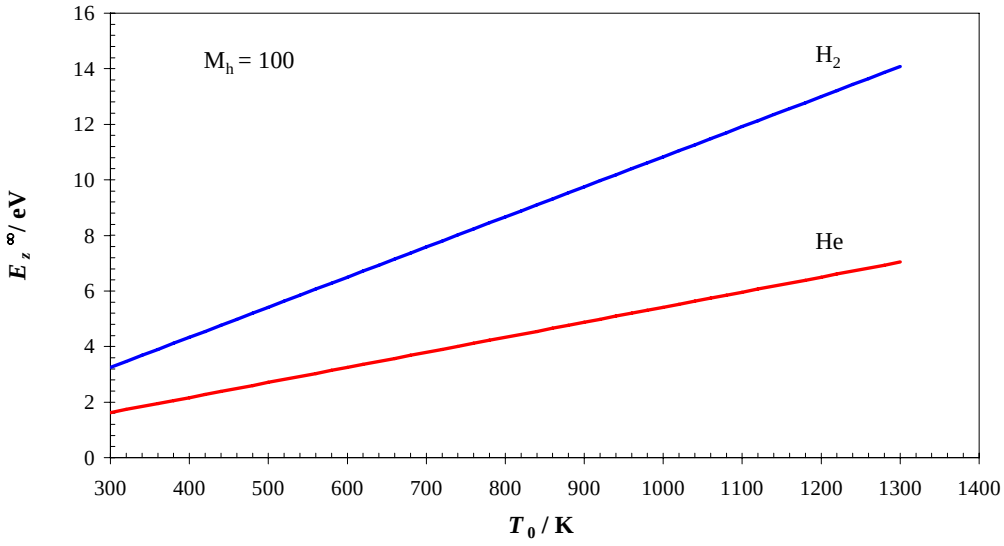

***Figure 5-10**. Effect of the gas inlet temperature on the kinetic energy of gas molecules of mass M_h = 100 a.m.u seeded in H_2 and He, respectively.*

5.4 EXPERIMENT

The main features of the UHV system used for the ionisation studies are described in chapter 3. The chamber is further equipped with a gas inlet and mixing system (GIMS), see figure 5-11, where the gas to be ionised is kept at the required inlet pressure and can be mixed with a carrier gas for hyperthermal beam generation. The gas is injected into the UHV chamber via a pulsed nozzle valve (PNV, GENERAL VACUUM COMPANY, series 99) having a ∅ = 0.5mm orifice. The PNV is externally operated via a programmable controller (IOTA ONE). The pulsed mode of operation ensures that the pressure in the main system remains adequately low. To get the gas outlet of the PNV sufficiently close to the target (10mm) it is mounted onto a 10cm UHV bellows translator.

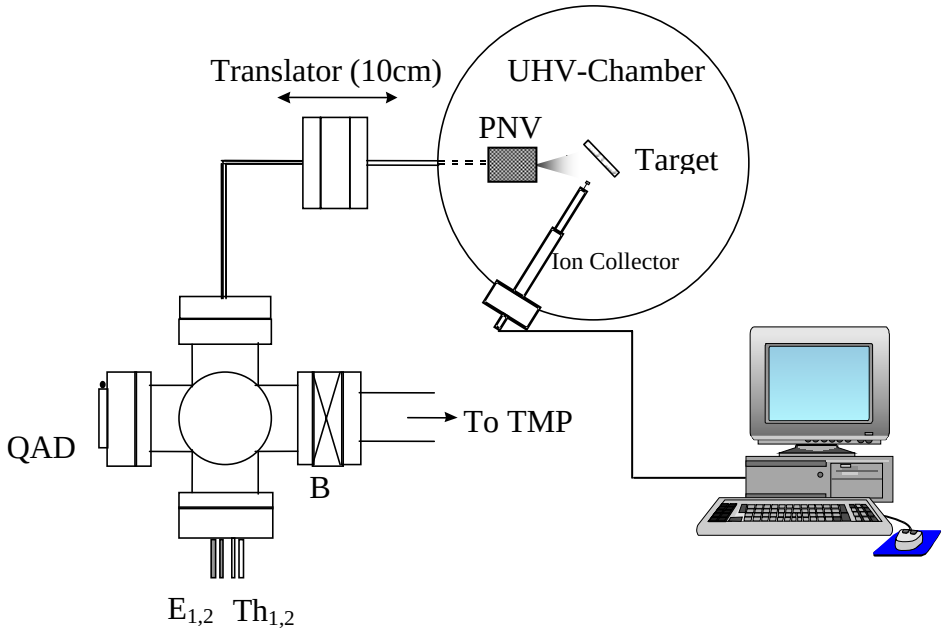

Figure 5-11. *Side Elevation of the GIMS showing the quick assess door (QAD), the butterfly valve (BV) connecting the GIMS to the turbo-molecular pump (TMP) and the pulsed nozzle valve (PNV) located, together with the target and the ion collector, in the UHV chamber. The PNV is mounted on a 10 cm translator allowing a variable orifice to target spacing and retraction of the mechanism during thin film evaporation.* $E_{1,2}$ *and* $Th_{1,2}$ *are electrical feedthroughs for sample heating and thermocouples.*

The Kelvin probe was used as an integral ion collector with a tip diameter of 2.5mm and a tip-to-target surface distance of typically 6mm. The target was held at ground potential and the collector tip at +5V for negative and –5V for positive ion collection. Information about the composition of these ion currents were obtained via the modified quadrupole mass spectrometer (QMS, EDWARDS EQ80F). A sketch of this arrangement is shown in figure 5-12. The target surface is mounted directly in front of the mass separation unit, effectively replacing the original electron impact ionisation cell. In this way only molecules from the residual gas envelope are able to hit the ionising surface and not directly from the molecular beam. However, since the background pressure of the species admitted into the chamber rises during gas inlet, this arrangement is sufficient for the purpose of obtaining mass spectrometric information of the ions created. The ions are extracted from the surface via the voltage V_{ex} applied between the ionising target surface and the QMS entrance slit.

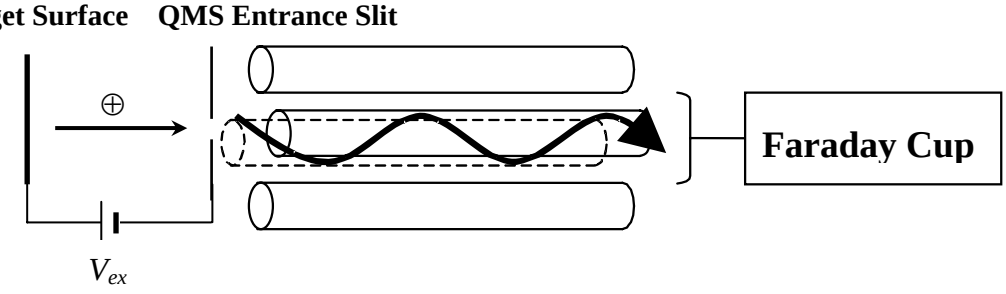

Figure 5-12*. Schematic of the modified QMS unit for surface ionisation experiments. For negative ion detection the sign of V_{ex} will be reversed.*

A polycrystalline Re foil (13mm×25mm×25μm) was used as the target surface. For positive ionisation experiments the foil was oxidised or coated with LaB_6 for negative ionisation experiments. The preparation of the targets is described in detail in chapter 4.

The GIMS is based upon a 6-way cross ($980cm^3$) and is pumped separately by a $65ls^{-1}$ turbo-molecular pump (TMP, EDWARDS EXT70) connected via a butterfly valve

(BV), see figure 5-11. The BV is closed during gas inlet but provides a high pumping efficiency when open and thus ensures a low residual gas pressure (<0.3mTorr) in the GIMS.

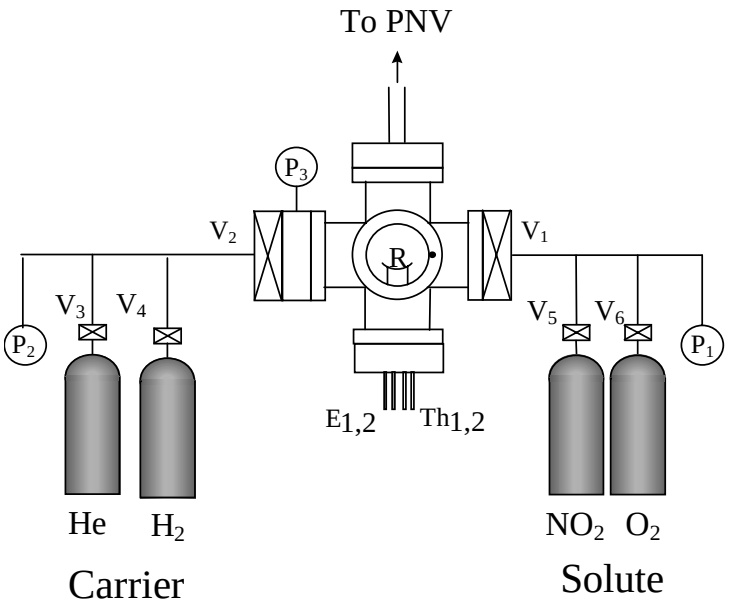

Figure 5-13. *Front elevation of the GIMS showing the 2 gas manifolds holding the carrier and solute gases that are leaked into the 6-way cross mixing chamber via leak valves V_1 and V_2. V_{3-6} are bottle-top on-off valves and P_{1-3} provide the pressure reading ot the different parts of the GIMS. R is a sample reservoir for solid and liquid samples and $E_{1,2}$ and $Th_{1,2}$ are electrical feedthroughs for sample heating and thermocouples.*

The quick access door (QAD) together with a sample reservoir in the GIMS (R) provide rapid interchange of solid or liquid samples that can be vaporised via resistive heating. Solute and carrier gases are let into the GIMS via UHV leak valves V_1 and V_2 from two separate gas manifolds holding the pressurised high purity gas canisters (MESSER GRIESSHEIM, 1l, 12bar, 99.998%), see figure 5-13. O_2 is used for the oxidation of the Re sample and NO_2 as the model gas for the ionisation experiments. Both He and H_2 are available as carrier gases for the generation of hyperthermal molecular beams for HSI experiments. The pressure in the GMIS and the gas manifolds can be monitored via convection gauges (P_{1-3}, TERRANOVA) operating in the range from 0.1mTorr up to

atmospheric pressure. The inlet system is baked out during operation to maintain the partial pressure of H_2O below 10^{-4}Torr.

5.5 RESULTS

5.5.1 Surface Ionisation under Continuous Gas Inlet

A. Collection Efficiency

In order to determine the collection efficiency γ_{coll} of the detection system, the potential V_b of the ion collector, i.e. the Kelvin probe tip, was varied between 5V and –5V. Ions were created by thermal surface ionisation of NO_2 molecules. The experiments were carried out under steady state conditions, i.e. with a constant flux of NO_2 molecules at an inlet pressure of p_0 = 500mTorr and T_0 = 300K. An oxidised Re target was used for p-SI and a LaB_6 surface for n-SI. Both targets were held at a temperature of 1100K. We see that in both cases the ion current rises sharply for collection potentials of <0V for p-SI and >0V for n-SI. The currents saturate at $V_b \lesssim$ -3.5V for p-SI and $V_b \gtrsim$ 4.5V for n-SI. We can thus assume a collection efficiency γ_{coll} for this measurement configuration of approximately 1 for the potentials that were applied to the collector tip of +5V for negative and –5V for positive ion collection.

Comparing the magnitudes of the ion currents measured with the model data plotted in figures 5-3 and 5-4 we find that the positive current measured at 1100K approximately agrees with the calculated data however, the negative ion current is several orders of magnitude less than expected. This indicates that even at elevated temperatures the initially low work function LaB_6 surface can not be kept clean from contamination during the exposure to NO_2 inevitably leading to an increase in ϕ_S and thus a considerable decrease in the ionisation efficiency.

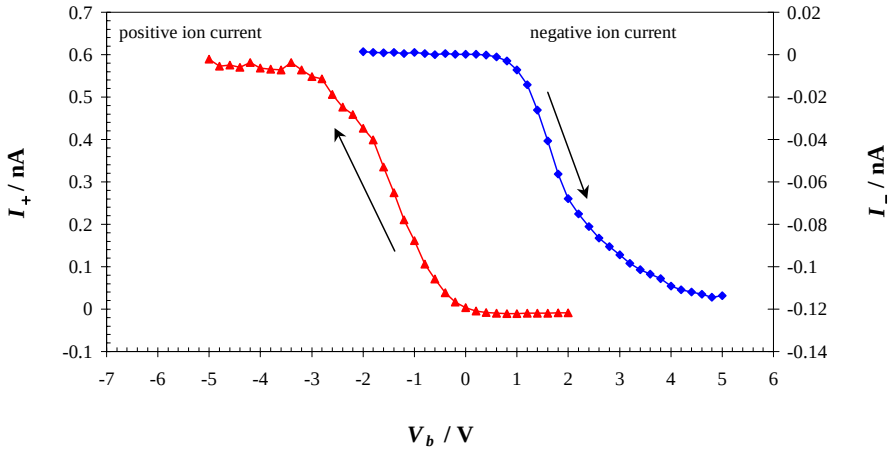

Figure 5-14. *Current-voltage characteristic of the surface ionisation measurement system. The arrows indicate the increase of the respective ion current with the bias potential V_b.*

B. Ion Current Dependence on Inlet Pressure

The ion current produced via surface ionisation in a thermal molecular beam is, according to equations 5-17 and 5-21, proportional to the gas inlet pressure p_0. While the same is true for hyperthermal beams, the actual flux of molecules will be reduced since the conductivity of the orifice decreases for pressures $p_0 > 1$Torr where the gas flow becomes viscous [12]. From figure 5-6 we also see that the transition from a thermal to a hyperthermal molecular beam occurs at a pressure $p_0 \cong 1$Torr for an orifice of $\varnothing = 0.5$mm. The ion current produced in this range of NO_2 inlet pressures on an oxidised Re surface at 1100K is plotted in figure 5-15.

We can clearly recognise 3 different regions in the curve (**A** to **C**). For pressures $p_0 < 0.7$Torr (**A**) and $p_0 > 0.9$Torr (**C**) the curve can be approximated by a linear function as indicated by the linear regression curves, with a transition region in between (**B**). The gradient of the linear curve fit in (**C**) is higher by a factor of approximately 25 compared to that in the lower pressure region (**A**). We can interpret this difference as the transition from a thermal to a hyperthermal molecular beam where the extra kinetic

energy of the molecules in the latter causes the increase in the ionisation efficiency expressed in the gradients of the curve in figure 5-15.

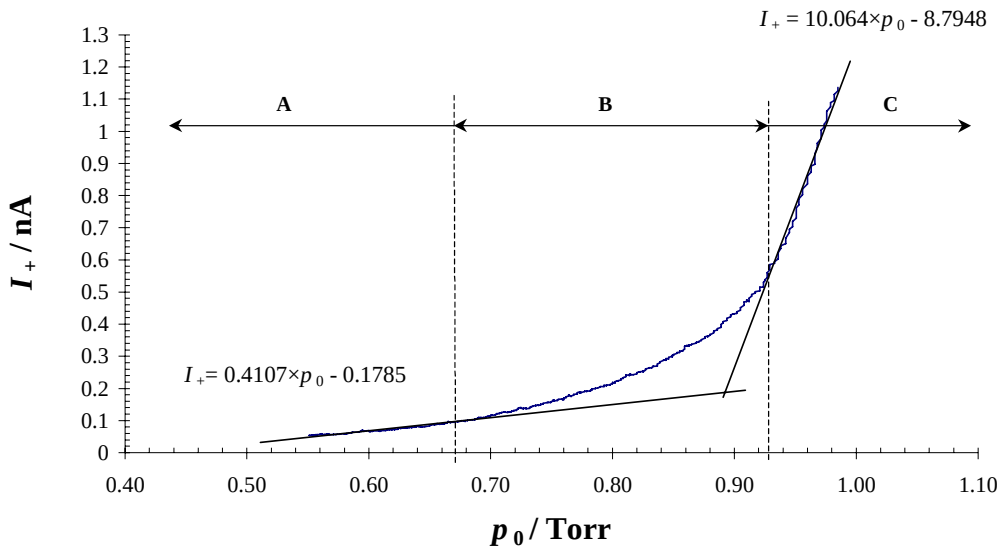

***Figure 5-15**. Positive ion current versus NO_2 gas inlet pressure p_0 on oxidised Re at 1100K.*

We can thus conclude that for thermal SI measurements gas inlet pressures of <0.7Torr are appropriate with this experimental setup while hyperthermal molecular beams can be obtained for p_0 > 0.9Torr.

C. Ion Current Dependence on Target Temperature

The target temperature T_S is another important factor with respect to the efficiency of the ionisation β, see equations 5-15 and 5-16. Therefore, the current of positive ions produced on the oxidised Re target at $p_0 = 500\text{mTorr}$ NO_2 and $T_0 = 300\text{K}$ was measured as a function of T_S as plotted in figure 5-16. We can see that the ion current can be approximated by an exponential dependence on the target temperature. Taking into account the flux of molecules hitting the surface the ionisation efficiency can be calculated according to equation 5-17.

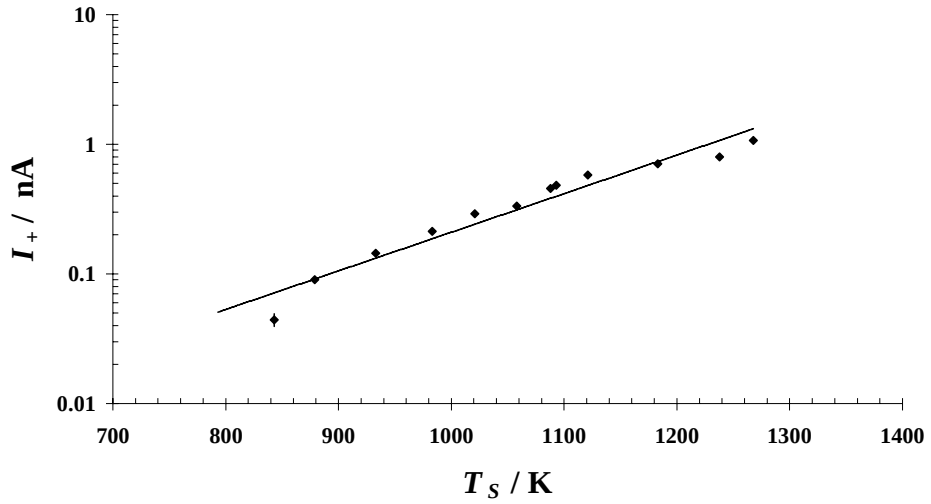

***Figure 5-16**. Positive ion current produced on the oxidised Re target at p_0 = 500mTorr NO_2 and T_0 = 300K as a function of the target temperature.*

For an inlet pressure of p_0 = 500mTorr at the temperature T_0 = 300K, according to equation 5-21, the flux of molecules hitting that surface is $q_{mol} = 2.9\times10^{19}$molecules·s^{-1}, see also figure 5-2. The ionisation efficiency β_+ determined for the dataset shown in figure 5-16 is plotted in figure 5-17. We see that β_+ indeed depends exponentially on $1/kT$. However, comparing these data with the calculated data according to equation 5-15 we find that the experimental data do not agree with the model developed in section 5.2 that is usually given in the literature [6].

If $I_g > \phi_S$, equation 5-15 can be approximated by

$$\beta_+ \approx \frac{g_+}{g_0} \cdot \mathrm{e}^{\frac{\phi_S - I_g}{kT}} . \qquad 5\text{-}30$$

The parameters of a least square fit of the experimental data via equation 5-30 are shown in figure 5-17. This might be due to other temperature dependent factors that affect the ionisation efficiency and which are not considered in the simple model for β. A discussion of this problem is e.g. given in [6]. Another reason might be the fragmentation of NO_2 that is observed in p-SI, see below.

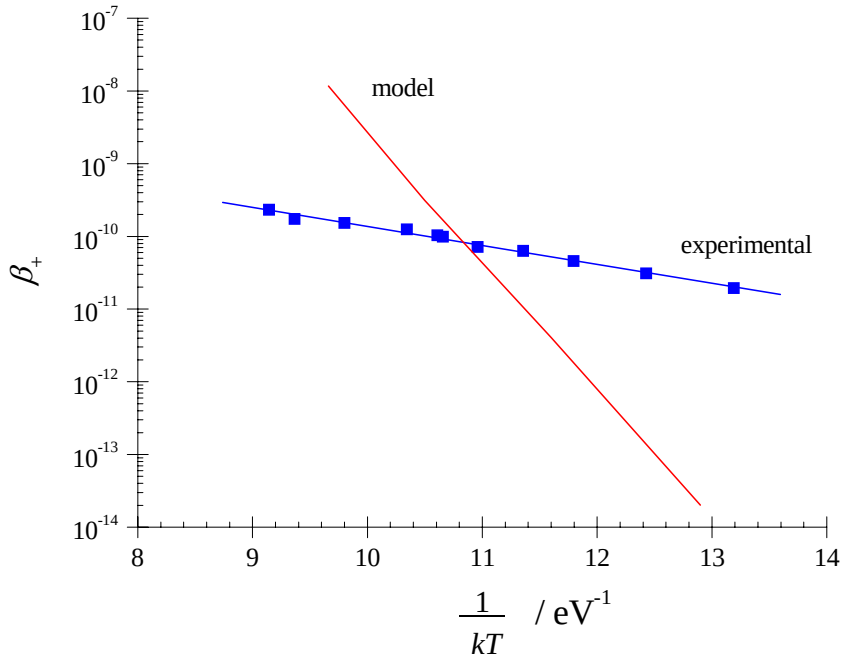

Figure 5-17*. Temperature dependence of the ionisation efficiency of positive surface ionisation of NO_2. The plot further shows a least square fit of the experimental data according to equation 5-30 and, for comparison, calculated data via equation 5-15.*

D. Surface Ionisation Mass Spectra

The experimental data presented in the previous sections show integral ions currents produced via thermal surface ionisation of NO_2 as a function of various parameters. Information about the composition of these ion currents were obtained via the modified quadrupole mass spectrometer (QMS) as described in section A. A mass spectrum of positive ions produced on an oxidised Re target surface at $T_S = 1600K$ is shown in figure 5-18. The inlet pressure of NO_2 was $p_0 = 1Torr$ and temperature $T_0 = 300K$. The background pressure in the chamber rose up to 4×10^{-4}Torr during gas inlet.

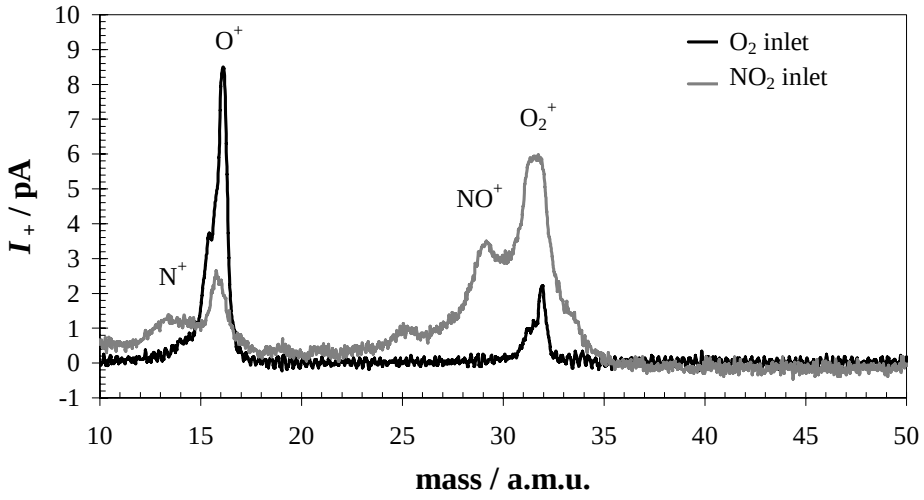

***Figure 5-18**. Mass spectra obtained via p- SI of O_2 and NO_2 gas molecules on oxidised Re at 1600K.*

We see that in the case of positive surface ionisation, the NO_2 molecules fragment mainly into O_2^+, NO^+, O^+ and a small fraction of N^+ ions. For comparison, the SI mass spectrum obtained from molecular oxygen at p_0 = 1Torr is plotted in figure 5-18 as well. We note that the ratios of the peak heights are dynamic at the start of the gas inlet, particularly that of O_2^+/O^+ and thus the spectrum shown here is a quasi-equilibrium between the different products of the dissociation of the molecules at the hot surface.

The mass spectrum of NO_2 at p_0 = 1Torr and T_0 = 300K obtained via negative SI on LaB_6 at 1200K is shown in figure 5-19. The main peak of the spectrum is at mass 48 which corresponds with the molecular mass of NO_2. The apparent peak at a mass of approximately 47 is an artefact of the measurement system indicating that the ion extraction voltage was chosen slightly too high [18]. Thus we can conclude that for negative SI of NO_2 no fragmentation occurs.

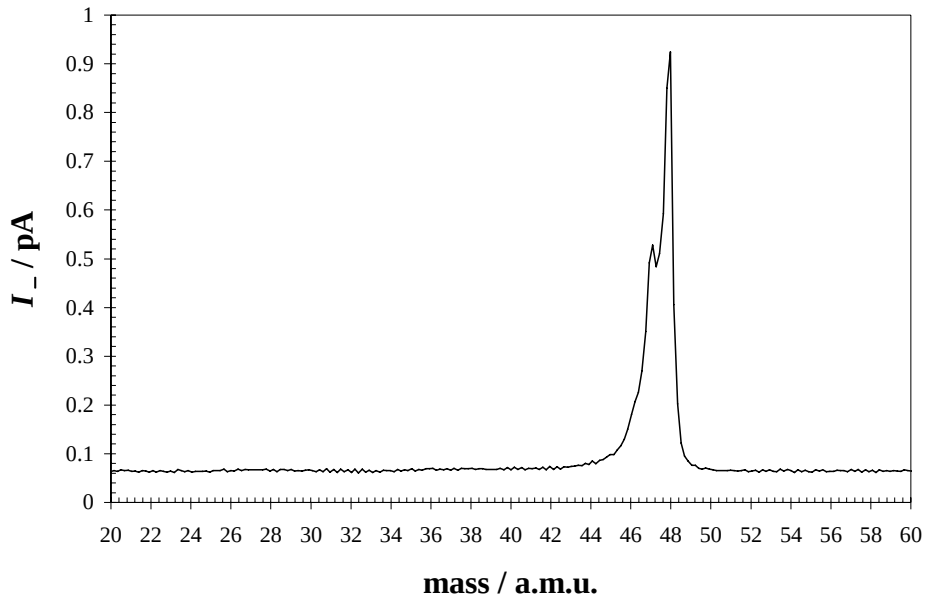

***Figure 5-19**. Mass spectrum obtained via n-SI of NO_2 gas molecules on LaB_6 at 1200K.*

5.5.2 Surface Ionisation under Pulsed Gas Inlet

In order to obtain a hyperthermal molecular beam the stagnation pressure should be $p_0 > 1$Torr or higher for seeded molecular beams. However, due to the significant pressure increase in the UHV chamber under these conditions ($>10^{-4}$Torr), HSI experiments have to be carried out in pulsed inlet mode. Ion current pulses produced on LaB_6 at various surface temperatures with $p_0 = 500$mTorr NO_2 seeded in 1000Torr He are plotted in figure 5-20. The duration of the gas pulse is 500ms in all cases. We note the peak in the current produced at $T_S = 1160$K at around 100ms, levelling at a distinctly lower current for $t > 300$ms. We can interpret this by an increase in the LaB_6 work function upon exposure to the NO_2 gas molecules which therefore decreases the ionisation efficiency. After the termination of the gas pulse NO_2 molecules evaporate from the surface and hence lowering its work function explaining the increase in the ion current just after the gas pulse.

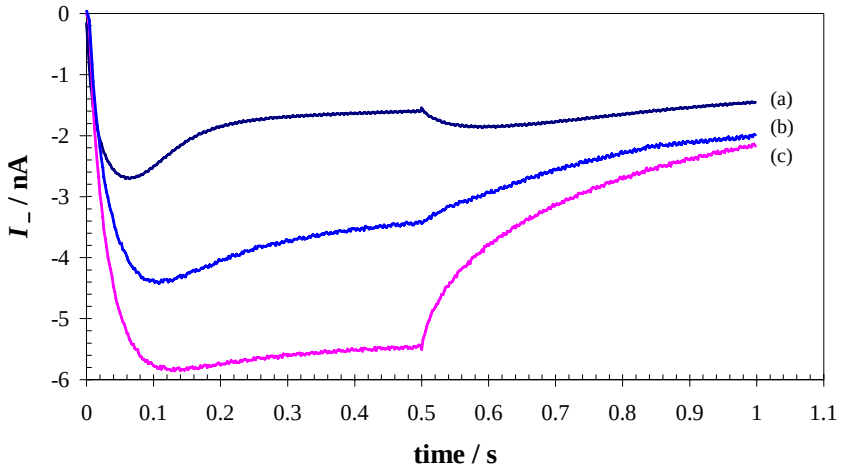

***Figure 5-20**. Ion currents from 0.5s pulses of NO_2 at 0.5Torr seeded in 1000Torr He on LaB_6 at (a) 1160K, (b) 1220K and (c) 1300K.*

At higher surface temperatures this behaviour is less visible due to the higher currents during the gas pulse. The continuation of the current for a considerable time after the pulse is caused by thermal SI of NO_2 molecules adsorbed at the surface and from the residual gas. Figure 5-21 shows a comparison of gas pulses under thermal and hyperthermal conditions, respectively. The maximum kinetic energy of the NO_2 molecules seeded in He at 300K is 0.75eV. We note an increase in the ionisation efficiency by a factor of approximately 2 slightly increasing with He stagnation pressure.

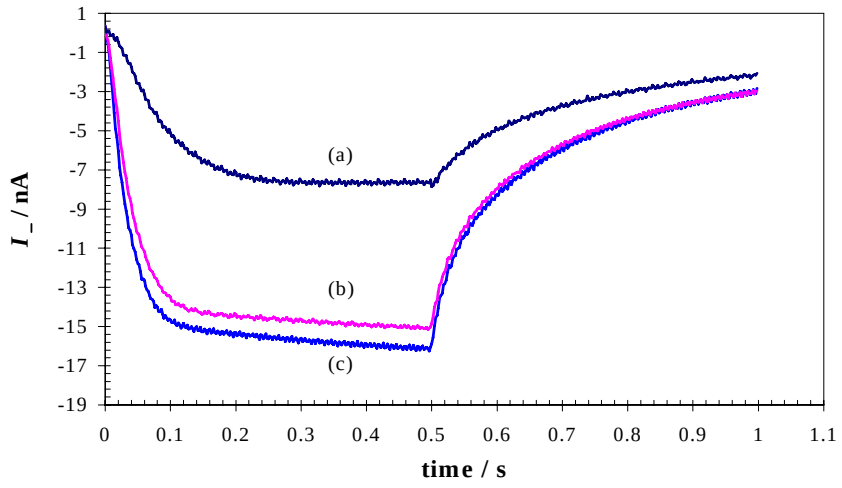

***Figure 5-21**. Ion currents from 0.5s pulses of 0.5Torr NO_2 on LaB_6 at 1200K where (a) is a thermal beam and (b) and (c) seeded in 10Torr and 50Torr He, respectively.*

5.6 CONCLUSIONS

The model derived for thermal surface ionisation shows that the ionisation efficiency depends exponentially on the factor $\Delta E/kT$, where ΔE is the energetic difference between the work function of the target surface and the ionisation potential or electron affinity for p-SI and n-SI, respectively. Although experimental data of NO_2 positively ionised on oxidised Re follow the exponential relationship, the experimental parameters fitted to the equation of the ionisation efficiency do not agree with the model. Possible explanations are the fragmentation of NO_2 observed in p-SI or, indeed, the use of a too simplistic model.

The ion current measured as a function of the NO_2 inlet pressure shows a change in the gradient of the curve between 0.7Torr and 0.9Torr using an inlet nozzle of diameter 0.5mm. This effect can be interpreted as the transition between thermal and hyperthermal surface ionisation increasing the ionisation efficiency by a factor of approximately 25. The model derived for the generation of hyperthermal molecular beams shows that 'seeding' effectively amplifies the kinetic energy of the molecules by a factor of M_h/M_l which can be further increased by heating the inlet nozzle.

Mass spectrometric data of p-SI show a fragmentation of NO_2 into mainly O_2^+, NO^+ and O^+ whereas n-SI produces a single peak at mass 48 which can be identified as NO_2^-. Negative SI and HSI data indicate a considerable increase in the work function of the LaB_6 target surface upon exposure to NO_2 even at elevated temperatures causing a substantial decrease in the ionisation efficiency.

REFERENCES

1. A. Amirav and A. Danon, , *J. Chem. Phys.* **87**, 4708 (1987).

2. S. Dagan, A. Amirav and T. Fujii, *Int. J. Mass Spectrom. Ion Processes* **151**, 159 (1995).

3. U. Petermann, I.D. Baikie, B. Lägel and K.M. Dirscherl in *Materials Science of Novel Oxide-Based Electronics*, edited by D.S. Ginley, D.M. Newns, H. Kawazoe, A.B. Kozyrev, J.D. Perkins (Mater. Res. Soc. Proc. **623**, Pittsburgh, PA, 2000) in press.

4. A. Danon, and A. Amirav, *Int. J. Mass Spectrom. Ion Processes* **96**, 139 (1990).

5. T. Sharhar, S.Dagan, and A. Amirav, *J. Am. Soc.Mass Spectrom.* **9**, 628 (1998).

6. J.C. Rivère, in *Solid State Surface Science*, Vol. 1, edited by M. Green (M.Dekker, New York, 1969), pp. 180-204.

7. R.H. Fowler, *Statistical Mechanics* (Cambridge, New York, 1929) pp. 267-268.

8. Dibeler, Walker, *Advan. Mass Spectrom.* **4**, 767 (1967).

9. Lifshitz, Hughes, *Chem. Phys. Lett.* **7**, 469 (1970).

10. A. Amirav, *Org. Mass. Spectrom.* **26**, 1 (1991).

11. S. Holloway, *J. Vac. Sci. Tech.* **A5**, 476 (1987).

12. L. Ward, J.P. Bunn, *Introduction to the theory and practice of high vacuum technology* (Butterworth, London 1967).

13. P.A Redhead, J.P. Hobson, E.V. Kornelsen, *The Physical Basis f Ultrahigh Vacuum*, edited by L. Holland (Chapman & Hall, London, 1968).

14. D.R. Miller, Free Jet Sources in *Atomic and Molecular Beam Methods*, edited by G. Scoles (Oxford University Press, New York, 1988), pp. 14-53.

15. H. Pauly, High-Energy Beam Sources in *Atomic and Molecular Beam Methods*, edited by G. Scoles (Oxford University Press, New York, 1988), pp. 134-137.

16. H. Kishi, F. Fujii, *J. Chem. Phys.* **99**, 11153 (1995).

17. P.M. Mayer, T. Baer, *Int. J. Mass Spectrom. Ion Processes* **156**, 133 (1996).

18. D. Bassi, Ionization Detectors II: Mass Selection and Ion Detection in *Atomic and Molecular Beam Methods*, edited by G. Scoles (Oxford University Press, New York, 1988), pp. 180-192.

Chapter 6

Detection of Defects and Impurities in Semiconductors

6.1 INTRODUCTION

The detection of defects and impurities, notably iron, in semiconductors, is of tremendous practical importance and a major concern in current wafer-scale semiconductor processing. Even minute amounts of impurities can alter the electrical characteristics of semiconductor devices considerably [1]. Therefore, reliable detection methods are required, not only for in-process monitoring of wafers but also to investigate the behaviour of impurities in semiconductors and their impact on device performance.

Semiconductor characterisation techniques based on the phenomenon of the surface photovoltage (SPV) have been proven extremely useful since its first studies by Brattain and Bardeen in the early 1950's [2]. The extensive range of experimental tools utilising the SPV in very different ways has been shown only recently in a comprehensive review of the surface photovoltage and its applications [3]. In this chapter we investigate the application of SPV measurements for the contactless detection of chemical contamination on semiconductor surfaces via (i) the saturation photovoltage measurement using the Kelvin probe [4, 5] and (ii) the frequency dependence of the SPV, termed the ac-SPV method [6]. Both techniques are based on the determination of the semiconductor surface potential and thus the charge density at the surface which is indicative of potential chemical contamination.

6.2 SEMICONDUCTOR SURFACE PHYSICS

6.2.1 Surface Charge

If we consider a cleaved surface of a semiconductor crystal unsaturated valence electrons of the surface atoms, also termed ‘dangling’ bonds, give rise to additional energy levels where the position of some of these states may be in the bandgap of the semiconductor E_g. This is also the case if atoms or molecules are attached to these bonds since the binding energy to foreign atoms is different from that of the native atoms in the bulk. We note that these states can be formed in a layer of a few atoms at the surface which is e.g. the case of the Dimer-Adatom Stacking fault (DAS) structure of the Si(111) reconstruction [7].

The occupation of these surface states is governed by the Fermi-Dirac distribution function, i.e. it depends on their energetic position in the band gap E_t with respect to the Fermi-level E_F [8, p.380]:

$$F_{SD} = \frac{1}{1 + g \cdot \mathrm{e}^{\frac{E_F - E_t}{kT}}} \qquad 6\text{-}1$$

$$F_{SA} = \frac{1}{1 + \frac{1}{g} \cdot \mathrm{e}^{\frac{E_t - E_F}{kT}}} \qquad 6\text{-}2$$

where F_{SD} and F_{SA} are the distribution functions for donor and acceptor states and g is the ground state degeneracy which is 2 for a donor and 4 for an acceptor. Consequently, surface states may be positively or negatively charged, constituting a plane of charge at the surface of the semiconductor. Contributions to the total surface charge Q_{SS} may also arise from charges in a surface oxide layer typical components of which are (1) interface

trapped charge Q_{it}, (2) oxide fixed charge Q_f, (3) oxide mobile charge Q_m and (4) oxide trapped charge Q_{ot} [8]. A characteristic energy band diagram of a Si surface having a thermally grown oxide layer is shown in figure 6-1.

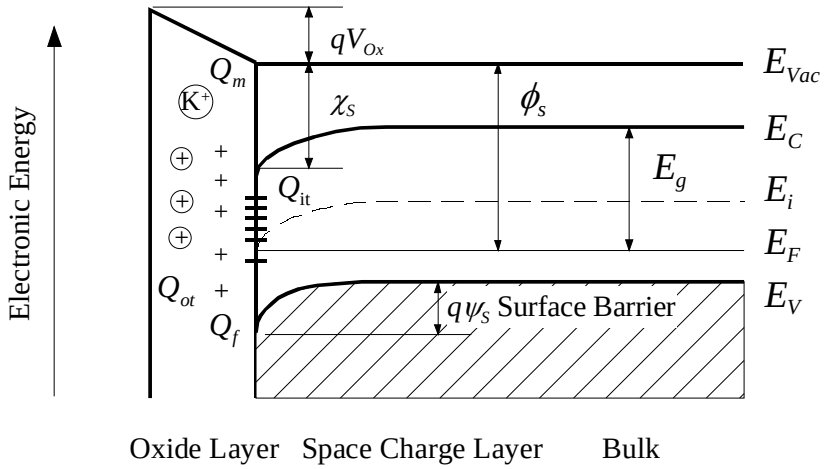

Figure 6-1. *Electronic energy level diagram of a semiconductor surface showing the work function ϕ_S, the electron affinity χ_S and the oxide barrier qV_{Ox} with q being the elementary charge. The surface space charge layer with surface potential $q\psi_S$ is induced by the total surface charge $Q_{SS} = Q_{it} + Q_f + Q_{Ot} + Q_m$. E_F denotes the Fermi energy level, E_i the intrinsic Fermi level and E_C and E_V the energy at the bottom of the conduction band and the top of the valence band, respectively.*

6.2.2 Surface Space Charge and Band Bending

Under thermal equilibrium conditions, the surface charge must be compensated by an equal and opposite space charge Q_{SC} in the semiconductor: $Q_{SS} = -Q_{SC}$. Due to the relatively low carrier concentration in semiconductors, compared to e.g. metals, the electrical field from the surface charges penetrates into the bulk thus creating a space charge at the surface with a position dependent electric field $E(z)$ in that region. This electrical field thus causes a potential difference $\psi(z)$ with respect to the bulk and hence a bending of the energy bands at the surface. In the following section we derive an expression to describe the surface band bending $q\psi_S$, where ψ_S is termed the surface potential, as a function of the surface space charge Q_{SC}.

The equilibrium electron and hole concentration in the bulk of a non-degenerate semiconductor, n_0 and p_0, can be described using the Boltzmann statistic by [8]:

$$n_0 = N_C \cdot \mathrm{e}^{-\frac{E_C - E_F}{kT}} \qquad 6\text{-}3$$

$$p_0 = N_V \cdot \mathrm{e}^{-\frac{E_F - E_V}{kT}} \qquad 6\text{-}4$$

where N_C and N_V are the effective density of states in the conduction and valence band, T is the absolute temperature and k is Boltzmann's constant. For an intrinsic semiconductor the Fermi level is denoted as the intrinsic Fermi level E_i, which lies approximately in the middle of the bandgap E_g [8]:

$$E_i = \frac{E_C + E_V}{2} + \frac{kT}{2} \cdot \ln\left(\frac{N_V}{N_C}\right) \qquad 6\text{-}5$$

and hence $p_0 = n_0 = n_i$, where n_i is the intrinsic carrier density. For this case equations 6-3 and 6-4 can be written as:

$$n_0 = n_i = N_C \cdot \mathrm{e}^{-\frac{E_C - E_i}{kT}} \qquad 6\text{-}6$$

$$p_0 = n_i = N_V \cdot \mathrm{e}^{-\frac{E_i - E_V}{kT}} \qquad 6\text{-}7$$

The bulk Fermi level for an extrinsic semiconductor with $|N_A - N_D| >> n_i$ is given for p-type doping, i.e. $N_A >> N_D$, assuming that all acceptors are ionised ($p_0 \cong N_A$), by [8]

$$E_F - E_i = kT \cdot \ln\left(\frac{N_A}{n_i}\right) . \qquad 6\text{-}8$$

Using the above equations the carrier densities can now be expressed via the difference between the actual and the intrinsic Fermi level as

$$n_0 = n_i \cdot \mathrm{e}^{\frac{E_F - E_i}{kT}} \qquad 6\text{-}9$$

$$p_0 = n_i \cdot \mathrm{e}^{\frac{E_i - E_F}{kT}} . \qquad 6\text{-}10$$

We now define the potentials describing the band bending according to Figure 6-2:

$$q\psi_B = E_F - E_{iB} \qquad 6\text{-}11$$

$$q\psi(x) = E_{iB} - E_i(x), \qquad 6\text{-}12$$

where E_{iB} is the intrinsic Fermi level in the bulk. The potential $\psi(x)$ at $x = 0$ is thus the surface potential ψ_S:

$$\psi_S = \psi(x = 0) . \qquad 6\text{-}13$$

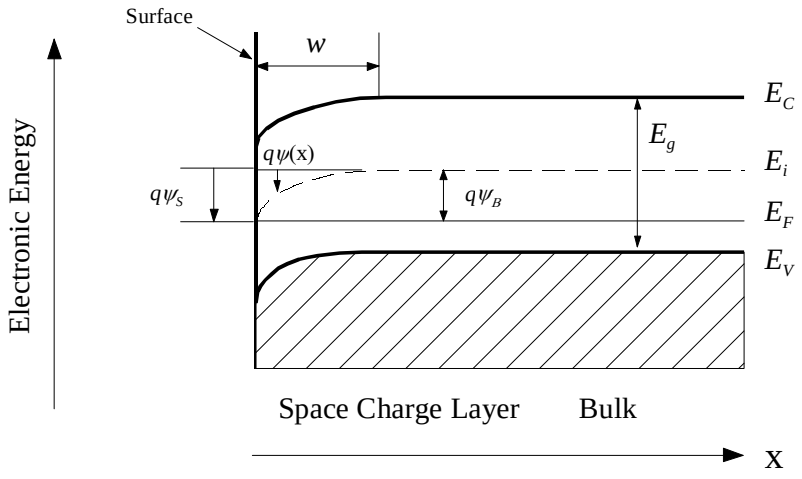

***Figure 6-2**. Electronic energy level diagram showing the potential defining the band bending $\psi(x)$ and the surface potential ψ_S at $x = 0$, which is positive in the direction shown, as well as the width of the space charge layer w.*

The difference between the intrinsic and the Fermi level can be expressed, using equation 6-12, by

$$E_F - E_i(x) = E_F - E_{iB} + q\psi(x). \qquad 6\text{-}14$$

Defining

$$\beta \equiv \frac{q}{kT} \qquad 6\text{-}15$$

and substituting 6-14 into 6-9 and 6-10 the position dependent carrier concentration in the space charge region (SCR) can be given by

$$n(x) = n_0 \cdot \mathrm{e}^{\beta\psi(x)} \qquad 6\text{-}16$$

$$p(x) = p_0 \cdot \mathrm{e}^{-\beta\psi(x)}. \qquad 6\text{-}17$$

We can now obtain the electrical field penetrating the semiconductor by solving Poisson's equation which is given by:

$$\frac{d^2\psi}{dx^2} = -\frac{\rho(x)}{\varepsilon_S} \qquad 6\text{-}18$$

where ε_S is the permittivity of the semiconductor and $\rho(x)$ the charge density in the SCR consisting of the fixed ionised donor and acceptor density N_D and N_A, respectively, as well as mobile holes and electrons:

$$\rho(x) = q\big(N_D - N_A + p(x) - n(x)\big). \qquad 6\text{-}19$$

The condition of charge neutrality in the bulk requires that

$$N_D - N_A = p_0 - n_0 \qquad 6\text{-}20$$

and thus, with equations 6-16 and 6-17:

$$p(x) - n(x) = p_0 \cdot \mathrm{e}^{-\beta\psi} - n_0 \cdot \mathrm{e}^{\beta\psi} \qquad \textit{6-21}$$

Therefore, using equations 6-19 to 6-21, Poisson's equation can be written as:

$$\frac{\mathrm{d}^2\psi}{\mathrm{d}x^2} = -\frac{q}{\varepsilon_S}\left[p_0\left(\mathrm{e}^{-\beta\psi} - 1\right) - n_0\left(\mathrm{e}^{\beta\psi} - 1\right)\right]. \qquad \textit{6-22}$$

With the definition of the electric field $E \equiv -\frac{\mathrm{d}\psi}{\mathrm{d}x}$ and multiplying equation 6-22 by $\mathrm{d}\psi$ the left hand side of 6-22 can be integrated from the bulk towards the surface:

$$\frac{d^2\psi}{dx^2} = \int_0^E E(x)dE = \frac{1}{2}E^2 \ . \qquad \textit{6-23}$$

Integration of the right hand side of 6-22, i.e. $-\frac{q}{\varepsilon_S} \cdot \int_0^{\psi}\left[\left(p_0 \cdot \mathrm{e}^{-\beta\psi} - 1\right) - \left(n_0 \cdot \mathrm{e}^{\beta\psi} - 1\right)\right] d\psi$, yields:

$$-\frac{q}{\varepsilon_S}\left[\frac{-p_0 \cdot \mathrm{e}^{-\beta\psi} + p_0\beta\psi + \cdot n_0 \cdot \mathrm{e}^{\beta\psi} - n_0\beta\psi}{\beta} + \frac{p_0 + n_0}{\beta}\right]. \qquad \textit{6-24}$$

For p-type semiconductors where $p_0 >> n_0$ expression 6-24 can be written as

$$\frac{2}{\beta^2} \cdot \frac{qp_0\beta}{\varepsilon_S}\left[\left(\mathrm{e}^{-\beta\psi} + \beta\psi - 1\right) + \frac{n_0}{p_0}\left(\mathrm{e}^{\beta\psi} - \beta\psi - 1\right)\right] \qquad \textit{6-25}$$

Introducing further the abbreviations

$$L_{Dp} = \sqrt{\frac{\varepsilon_S}{qp_0\beta}} \qquad \textit{6-26}$$

and

$$F_p(\beta,\psi,n_0,p_0)=\left[\left(e^{-\beta\psi}+\beta\psi-1\right)+\frac{n_0}{p_0}\left(e^{\beta\psi}-\beta\psi-1\right)\right]^{\frac{1}{2}} \qquad 6\text{-}27$$

where L_{Dp} is the extrinsic Debye length for holes and F_p is called the space charge factor. The respective expressions for n-type semiconductors are:

$$L_{Dn}=\sqrt{\frac{\varepsilon_S}{qn_0\beta}} \qquad 6\text{-}28$$

and

$$F_n(\beta,\psi,n_0,p_0)=\left[\frac{p_0}{n_0}\left(e^{-\beta\psi}+\beta\psi-1\right)+\left(e^{\beta\psi}-\beta\psi-1\right)\right]^{\frac{1}{2}} \qquad 6\text{-}29$$

Hence the electric field is

$$E=\pm\frac{\sqrt{2}}{\beta L_D}\cdot F(\beta,\psi,n_0,p_0) \qquad 6\text{-}30$$

with a positive sign for $\psi>0$ and negative sign for $\psi<0$. The electrical field at the surface is thus given by

$$E_S=\pm\frac{\sqrt{2}}{\beta L_D}\cdot F(\beta,\psi_S,n_0,p_0) \qquad 6\text{-}31$$

Applying Gauss's law the space charge per unit area, Q_{SC}, required to produce E_S is

$$Q_{SC}=-\varepsilon_S E_S=\mp\frac{\sqrt{2}\varepsilon_S}{\beta L_D}\cdot F(\beta,\psi_S,n_0,p_0). \qquad 6\text{-}32$$

The variation of the space charge density as a function of the surface potential is plotted in figure 6-3 for a p-type Si sample at 300K with a doping density of $N_A = 7\times10^{14}$ cm^{-3}. The Fermi level for this semiconductor is, using equation 6-8, at $E_{iB} - E_F = 0.284$eV from the intrinsic Fermi level in the bulk and hence ψ_B equals 0.284V.

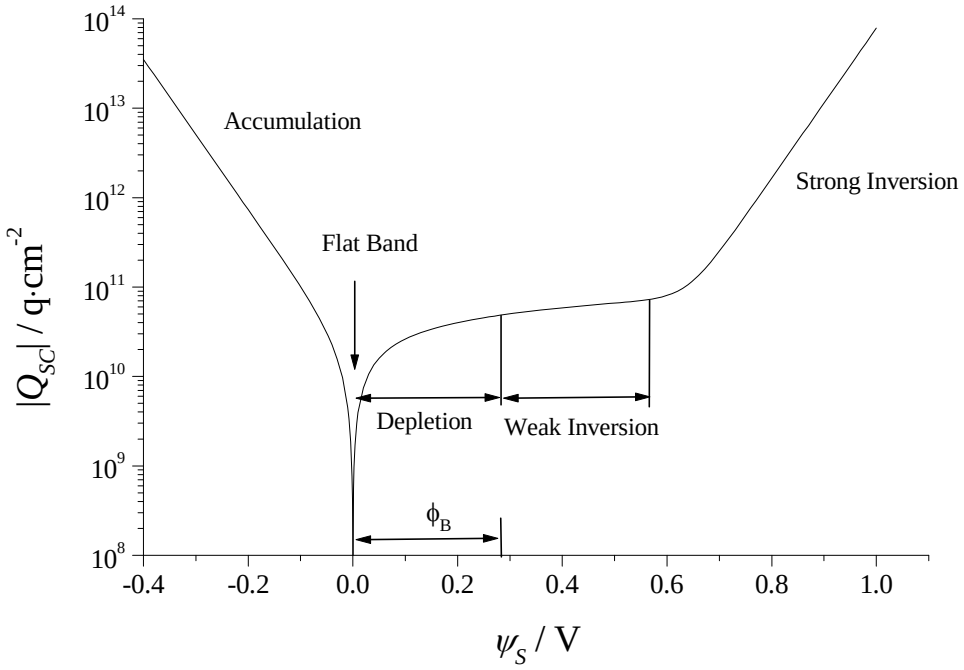

***Figure 6-3**. Variation of the space charge density Q_{SC} as a function of the surface potential ψ_S for p-type silicon at 300K with doping density $N_A = 7\times10^{14}$ cm^{-3}.*

We can distinguish five possible cases of surface layers as indicated in figure 6-3: accumulation, flat band, depletion and weak and strong inversion. We will consider these cases by means of the example p–type semiconductor.

(i) $\psi_S < 0$: Q_{SC} is positive and an upwards band-bending results in an increasing density of holes producing an accumulation layer. The function F_p is dominated by the first term in equation 6-27 and hence $Q_{SC} \sim e^{-\frac{\beta\psi_S}{2}}$.

(ii) $\psi_S = 0$: No space charge and thus no band bending, i.e. the bands are flat and hence the carrier concentration remains constant up to the surface.

(iii) $\psi_B > \psi_S > 0$: Q_{SC} is negative causing a downwards band-bending less than ψ_B that results in the depletion of the surface layer of holes. The function F_p is now dominated by the second term of 6-27 and hence $Q_{SC} \sim \sqrt{\psi_S}$. This indicates that the charges in the SCR are governed by the fixed acceptors.

(iv) $2\psi_B > \psi_S > \psi_B$: as the negative space charge density and hence the band-bending increases, the conduction band crosses the Fermi-level creating an electron density which surpasses the hole bulk density thereby producing an inversion layer.

(v) $\psi_S > 2\psi_B$: in the strong inversion region the concentration of electrons increases in a thin inversion layer at the surface effectively screening the semiconductor from further penetration of the electrical field. This leaves the width of the space charge layer constant at a maximum value w_{max}. The increase in electron concentration is now dominated by the fourth term in 6-27, i.e. $Q_{SC} \sim e^{\frac{\beta\psi_S}{2}}$.

The width of the space charge layer for the depletion and weak inversion case can be given as a function of the surface potential by [8]

$$w = \sqrt{\frac{2\psi_S \varepsilon_S}{qN_A}} \quad . \qquad \textit{6-33}$$

The maximum width of the space charge layer is achieved at the transition of the layer into strong inversion, i.e. for $\psi_S(\text{inv}) \geq 2\psi_B$, and is, using equations 6-8 and 6-11, given by:

$$w_{\max} = \sqrt{\frac{2\psi_S(\text{inv})\varepsilon_S}{qN_A}} = \sqrt{\frac{4\varepsilon_S \cdot \ln(N_A/n_i)}{q\beta N_A}} \quad . \qquad \textit{6-34}$$

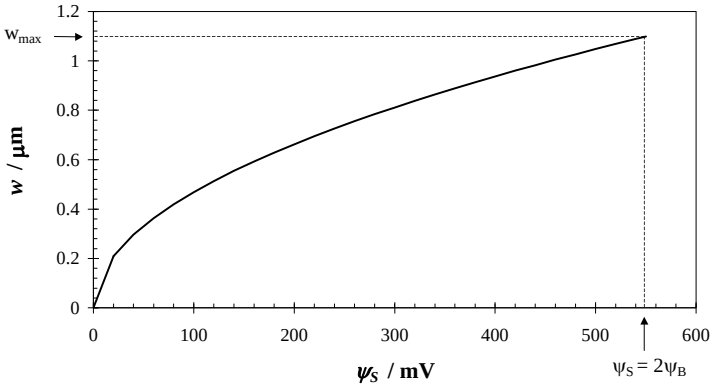

***Figure 6-4**. Depletion layer width as a function of the surface potential for p-type silicon at 300K with doping density $N_A = 7\times10^{14}$ cm^{-3}.*

6.2.3 Surface Photovoltage

The surface photovoltage (SPV) is a change in the surface potential of a semiconductor in the dark and under illumination and is measured as a voltage between the surface and the bulk of the illuminated specimen. Two mechanisms have been suggested to induce this voltage:

(i) Photo-excited excess carriers injected via super-bandgap illumination tend to screen the surface charge thus reducing the space charge width and band bending [9]. We note that these carriers can not produce a net charge in the SCR but rather a redistribution of charge and hence, associated with this, a change in the surface potential.

(ii) injected excess carriers may also modify the surface charge via a change in the surface state population through carrier trapping [10] or by direct excitation of carriers from or to surface states via sub-bandgap illumination thus changing the surface potential. The latter mechanism is e.g. utilised in Surface Photovoltage Spectroscopy, SPS [11].

Since charge redistribution is the main mechanism causing the SPV under super-bandgap illumination, which was used here, we restrict our analysis to mainly this case.

The analysis of this mechanism outlined in the following section is based on the model developed by Johnson [9] and is often referred to as the charge redistribution model.

6.2.4 SPV as a Function of Excess Carrier Density

The excess carrier densities, Δn and Δp, are defined as the difference between the carrier densities under illumination, n_{ill} and p_{ill}, and the bulk carrier concentrations in thermal equilibrium, n_0 and p_0:

$$n_{ill} = n_0 + \Delta n \qquad 6\text{-}35$$

$$p_{ill} = p_0 + \Delta p \qquad 6\text{-}36$$

Analogous to equations 6-16 and 6-17 the position dependent carrier density under illumination can be expressed as:

$$n_{ill}(x) = \left(n_0 + \Delta n\right) \cdot \mathrm{e}^{\beta\psi_{ill}(x)} \qquad 6\text{-}37$$

$$p_{ill}(x) = \left(p_0 + \Delta p\right) \cdot \mathrm{e}^{-\beta\psi_{ill}(x)} \ , \qquad 6\text{-}38$$

where ψ_{ill} is the surface potential under illumination. Therefore, Poisson's equation for the space charge under illumination is given by:

$$\frac{\mathrm{d}^2\psi_{ill}}{\mathrm{d}x^2} = -\frac{q}{\varepsilon_S}\left[p_0\left(\mathrm{e}^{-\beta\psi_{ill}} - 1\right) - n_0\left(\mathrm{e}^{\beta\psi_{ill}} - 1\right) + \Delta p \cdot \mathrm{e}^{-\beta\psi_{ill}} - \Delta n \cdot \mathrm{e}^{\beta\psi_{ill}}\right] \qquad 6\text{-}39$$

Integration of the first two terms yield, analogous to expressions 6-27 and 6-29, the space charge factor under illumination:

$$F_{p,ill}(\beta,\psi_{ill},n_0,p_0)=\left[\left(e^{-\beta\psi_{ill}}+\beta\psi_{ill}-1\right)+\frac{n_0}{p_0}\left(e^{\beta\psi_{ill}}-\beta\psi_{ill}-1\right)\right]^{\frac{1}{2}} \qquad 6\text{-}40$$

$$F_{n,ill}(\beta,\psi_{ill},n_0,p_0)=\left[\frac{p_0}{n_0}\left(e^{-\beta\psi_{ill}}+\beta\psi_{ill}-1\right)+\left(e^{\beta\psi_{ill}}-\beta\psi_{ill}-1\right)\right]^{\frac{1}{2}} \qquad 6\text{-}41$$

while the third term, accounting for the injected carriers with $\Delta n = \Delta p$, gives:

$$-\frac{q\Delta p}{\varepsilon\beta_S}\left[e^{-\beta\psi_{ill}}+e^{\beta\psi_{ill}}-2\right]. \qquad 6\text{-}42$$

Thus the excess carrier space charge factor can be written as

$$F_{\Delta p,\,ill}=-\frac{q\Delta p}{p_0}\left[e^{-\beta\psi_{ill}}+e^{\beta\psi_{ill}}-2\right]^{\frac{1}{2}} \qquad 6\text{-}43$$

$$F_{\Delta n,\,ill}=-\frac{q\Delta p}{n_0}\left[e^{-\beta\psi_{ill}}+e^{\beta\psi_{ill}}-2\right]^{\frac{1}{2}} \qquad 6\text{-}44$$

and hence the electrical field at the surface as

$$E_S=\pm\frac{\sqrt{2}}{\beta\cdot L_D}\cdot\sqrt{F_{S,\,ill}^2+F_{\Delta p,\,ill}^2} \qquad 6\text{-}45$$

Analogous to equation 6-32, the space charge density under illumination is given by

$$Q_{SC,\,ill}=\mp\frac{\sqrt{2}\varepsilon_S}{\beta L_D}\cdot\sqrt{F_{S,\,ill}^2+F_{\Delta p,\,ill}^2}\ . \qquad 6\text{-}46$$

Charge neutrality requires that $Q_{SS} + Q_{SC} = 0$ in darkness as well as under illumination. With the assumption made above that the charges in the surface states remain unchanged, then the space charge per unit area in darkness, Q_{SC}, must equal that under illumination, $Q_{SC,\,ill}$:

$$Q_{SC} = Q_{SC,ill} \qquad \textit{6-47}$$

and therefore

$$F_S(\psi_S)^2 = F_S(\psi_{S,ill})^2 + F_{\Delta p,ill}(\psi_{S,ill})^2 \qquad \textit{6-48}$$

Comparing the left and the right-hand side of equation 6-48, we see that the surface potential under illumination must be less than in darkness since $F_S \geq 0$, i.e.

$$\Delta\psi = \psi_{S,ill} - \psi_S \qquad \textit{6-49}$$

where $\Delta\psi$ is the surface photovoltage. Since equation 6-48 can not be explicitly solved for $\Delta\psi$, we solve 6-48 for the excess carrier density Δp and plot the solution as a function of the carrier injection level η, where η is given for a p-type semiconductor by

$$\eta = \frac{\Delta p}{p_0} \qquad \textit{6-50}$$

and Δp, with equations 6-43 and 6-48:

$$\Delta p = \frac{F_S(\psi_S)^2 - F_{\Delta S,ill}(\psi_{S,ill})^2}{\frac{1}{p_0}\left(e^{-\beta\psi_{S,ill}} + e^{\beta\psi_{S,ill}} - 2\right)} \; . \qquad \textit{6-51}$$

The solution of 6-51 is plotted in figure 6-5 for p-type Si at 300K with a doping density of $N_A = 7\times10^{14}$ cm^{-3} for different surface potentials. We can distinguish 3 main features in the graphs in figure 6-5: an approximately linear increase in $\Delta\psi$ for $\Delta\psi$<10meV, followed by a logarithmic increase in $\Delta\psi$ with injection level and finally asymptotically approaches the value of the surface potential ψ_0 [9, 12].

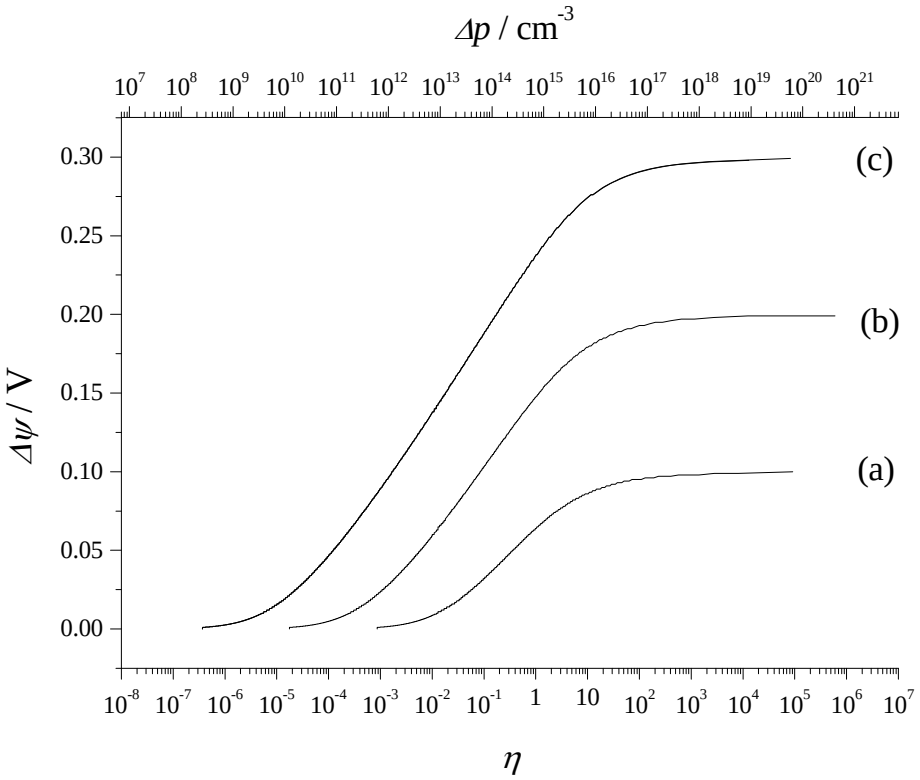

***Figure 6-5**. Surface photovoltage as a function of carrier injection level according to equation 6-51 for p-type silicon at 300K and a doping density of $N_A = 7\times10^{14}$ cm^{-3}. The SPV is plotted for surface potentials ψ_S of (a) 0.1V, (b) 0.2V and (c) 0.3V corresponding to depletion and weak inversion space charge layers.*

The region of linear increase of $\Delta\psi$ with Δp can be utilised for the measurement of minority carrier lifetimes [13, 14] whereas the measurement of the saturation photovoltage offers the possibility to determine the surface potential and hence the surface charge [4, 15]. Both parameters are not only valuable indicators of possible defects or impurities in the semiconductor surface region but also significantly affect the performance of semiconductor based electronic devices [16, 17].

6.2.5 Measurement of the SPV

Measurement of the SPV is accomplished by placing a conducting and typically semitransparent electrode at a distance *d* above the surface of the specimen using a contact on the back side of the sample to complete the circuit. Since the electrode is

capacitively coupled to the sample surface the light signal illuminating the sample is typically pulsed or modulated with a sinusoidal waveform inducing an ac-SPV signal.

Further, since the electron affinity χ_S is a constant, a change in the surface potential causes also a change in the contact potential difference. Therefore the surface photovoltage can be measured by the Kelvin probe with its inherited high accuracy ($\leq$ 1mV). The Kelvin method is also the only technique to measure the SPV in a non-contact mode under constant illumination, i.e. with a dc-light signal. In the following section we discuss the measurement of the surface photovoltage using the Kelvin probe and the application of this technique to determine the charge and thus chemical contamination on a semiconductor surface.

6.3 THE SATURATION SPV MEASUREMENT

6.3.1 Experiment

Figure 6-6 shows the experimental setup using of the Kelvin probe to measure the surface photovoltage of a semiconducting specimen. The measurement system is situated in a dark box where the sample is shielded from background illumination and electromagnetic interference. We can further assume that the backside of the sample is not exposed to any illumination and thus no photovoltage is induced there.

A 3mW laser diode was used as the light source for the Kelvin probe SPV experiments. The laser diode has a centre wavelength of 670nm which equals a photon energy of 1.85eV. Since this is higher than the bandgap energy of silicon of 1.2eV electrons from the valence band will be promoted directly to the conduction band.

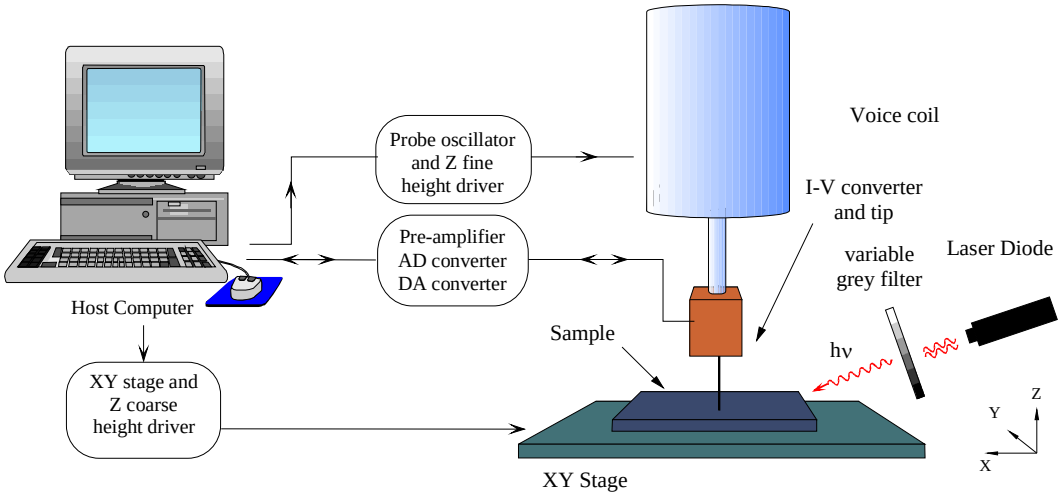

***Figure 6-6**. Sketch of the scanning Kelvin probe showing the laser diode light source illuminating the sample mounted onto the scanning stage, the probe head assembly and the probe control peripherals.*

The neutral density filter allows a variation of the photonflux Φ of the laser diode in the range of (7×10^{15}…3×10^{17}) photons·s^{-1}·cm^{-2} where a flux of 8×10^{17} photons·s^{-1}·cm^{-2} is obtained without a filter. The photon flux emitted from the laser diode was measured with a photodiode (BPX65) as shown in the circuit diagram in figure 6-7 using a low impedance I-V converter to ensure linearity between the photon flux and the output signal V_{out} [18].

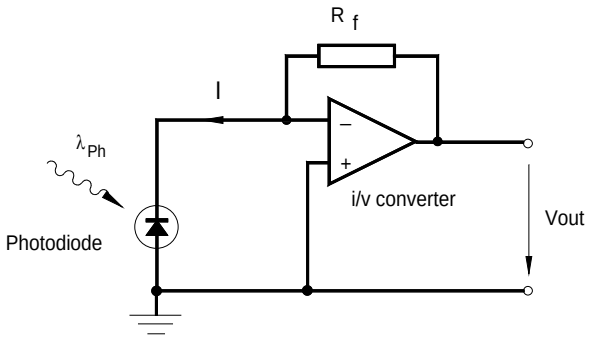

***Figure 6-7**. Measurement circuit for the light source characterisation where the incident light of wavelength λ_{Ph} induces the photocurrent I that is converted to the output voltage V_{out} via the operational amplifier with the feed-back resistance R_f.*

The surface photovoltage was measured on a series of p-type Si(100) wafers that were prepared by IMEC (Leuven, Belgium). The wafers are boron doped with $N_A = 7\times10^{14}$ cm^{-3} and have undergone different treatments as summarised in table 6-1. Appropriate wafer cleaning procedures are a key issue in semiconductor processing to remove particles and contamination from the wafer surface where metal contamination is a major concern, residual iron probably the most insidious impurity [1]. The effect of iron contamination was tested on these wafers, labelled A, B, C and D, which received a general RCA cleaning procedure and a single SC1 cleaning step followed by H_2O rinse and dry. The RCA-cleaning sequence consists of 3 major steps: an SC1 solution (1:1:5 $NH_4OH:H_2O_2:H_2O$), diluted HF (50:1 H_2O:HF) and SC2 (1:1:6 $HCl:H_2O_2:H_2O$), see e.g. [19]. The SC1 cleaning applied to wafer B and D was spiked with iron resulting in a surface Fe concentration of typically $\leq 10^{12}$ atoms/cm^2. Wafer C and D received a gate oxidation (30 min at 900°C) resulting in an oxide thickness of approximately 15nm, whereas wafer A and B both exhibit native oxides.

Table 6-1. *Overview of the treatments received by the different wafers.*

Wafer	General RCA Cleaning Procedure	SC1 (Clean)	SC1 (Fe contaminated)	Native Oxide	Gate Oxide (≈ 15 nm)
A	×	×		×	
B	×		×	×	
C	×	×			×
D	×		×		×

The surface photovoltage is measured with the Kelvin probe as the difference in the CPD in darkness and under illumination. The work function values are given with respect to a reference gold surface with an assumed work function of 5.1eV [20]. The surface charge was calculated from the saturation SPV value via equation 6-32.

6.3.2 Results

The variation of the SPV with photon flux measured on wafer C is shown in figure 6-8. We find that for a flux of photons of $>10^{16}$ $cm^{-2}s^{-1}$ the gradient of the curve becomes small enough that a saturation of the SPV can be assumed within approximately 10% of the final value. This result however also shows that in order to achieve a true saturation very high illumination intensities are required, i.e. a photon flux in the order of 10^{18} to 10^{19} $cm^{-2}s^{-1}$.

Examples of work function topographies and surface charge distributions are shown in figure 6-9 and 6–10 for the Si wafers A and B. We note that the iron contaminated wafer exhibits a higher work function than the clean wafer A. Further, the surface charge scans reveal a distinctly different charge pattern of the iron contaminated wafer B compared to the clean wafer A. The contamination causes the very inhomogeneous, partly negative surface charge.

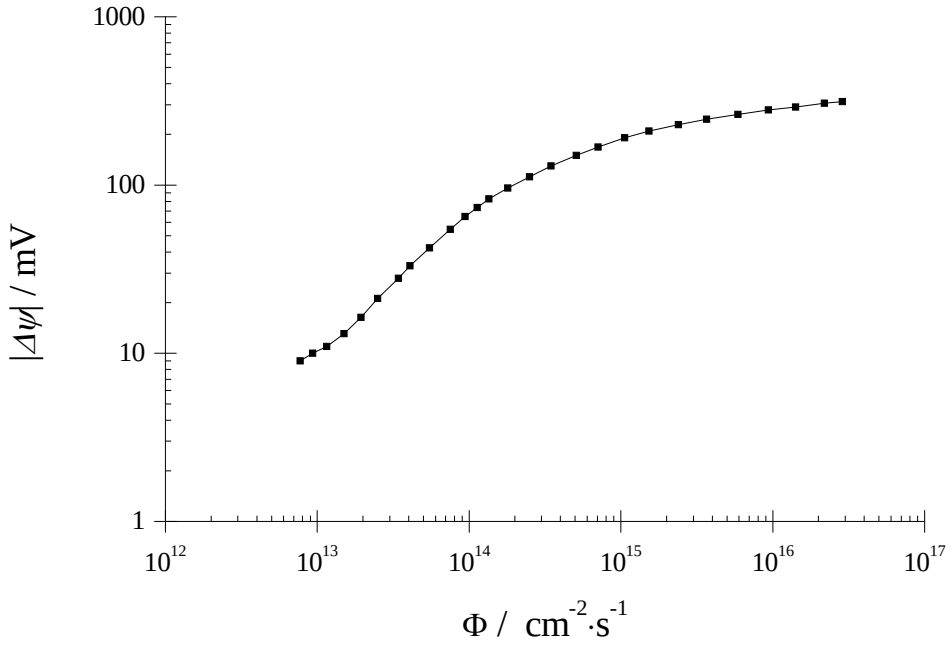

***Figure 6-8**. The surface photovoltage as a function of the incident photon flux measured on Si wafer C.*

The results of the wafer scans are summarised in figure 6-11, where the surface charge is given in elementary charge per unit area. We find that the thermally oxidised wafers (C and D) generally have a higher positive surface charge than the wafers having a native oxide layer (A and B).

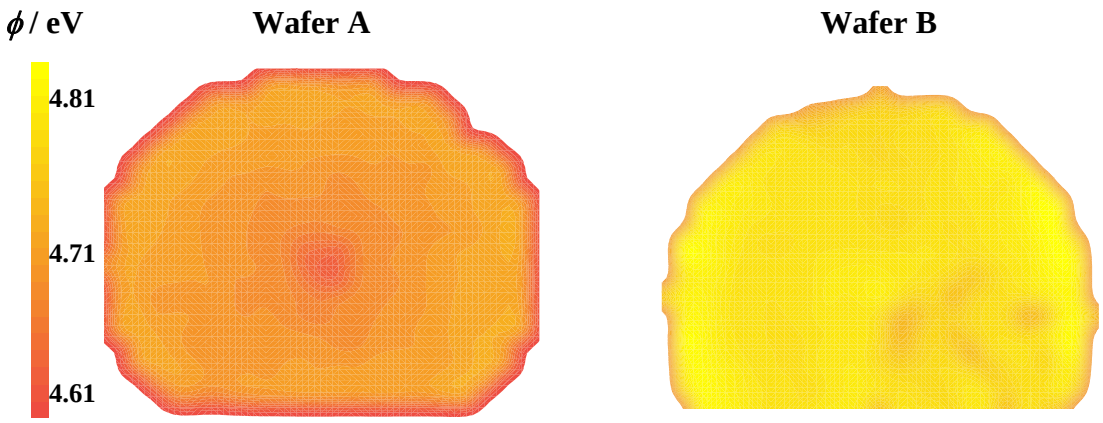

***Figure 6-9**. Work function scans of the clean (A) and Fe contaminated (B) Si wafer. Note that a sector of the wafers has been removed for chemical analysis.*

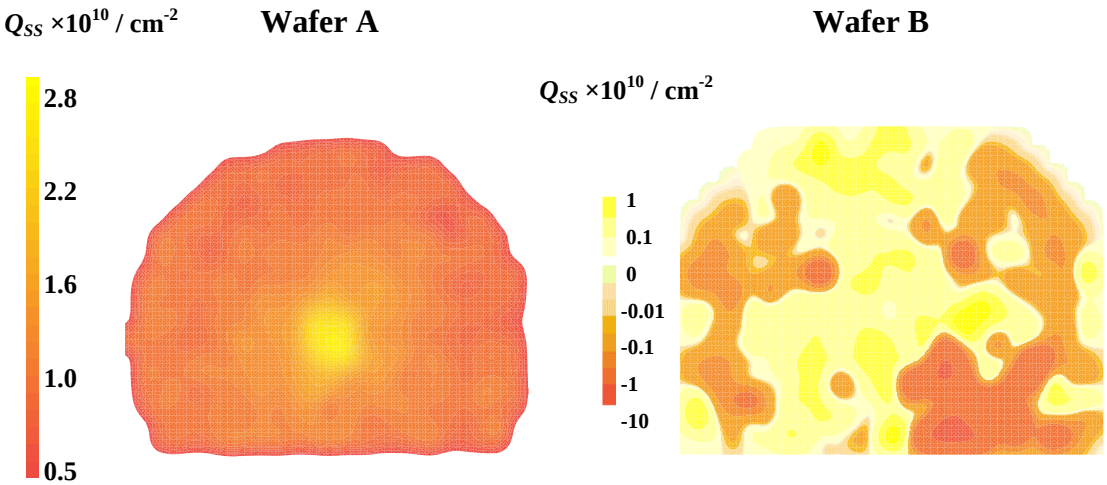

***Figure 6-10**. Surface charge scans of the clean (A) and Fe contaminated (B) Si wafer. The dark areas of wafer B correspond to a negative charge indicating the iron surface contamination.*

However, the iron contamination reduces the surface charge by an average of 3.4×10^{10} cm^{-2} for wafer B compared to A and by an average of 0.84×10^{10} cm^{-2} for wafer D compared to C. The observed effect of a decrease in total surface charge due to surface Fe contamination on p-type Si is similar to that reported in [21]. The standard deviations of the surface charge scans are $\pm 0.6\times10^{10}$ cm^{-2} for wafer A and $\pm 0.3\times10^{10}$ cm^{-2} for wafer C and D, thus indicating a fairly homogeneous charge distribution. In contrast, the iron contamination on wafer B causes a very inhomogeneous surface charge distribution with a standard deviation of $\sigma = \pm 9.9\times10^{10}$ cm^{-2}.

We further note that the change in surface charge due to the iron contamination obtained by SPV measurement corresponds to a change in the measured dark work function. An increase in the positive surface charge increases the surface potential ψ_S, see figure 6-3. Since the electron affinity of the semiconductor is a constant, this results in a decrease in its work function. Thus Kelvin probe CPD measurements are indicative for surface contamination provided that the contaminant contributes to the total surface charge.

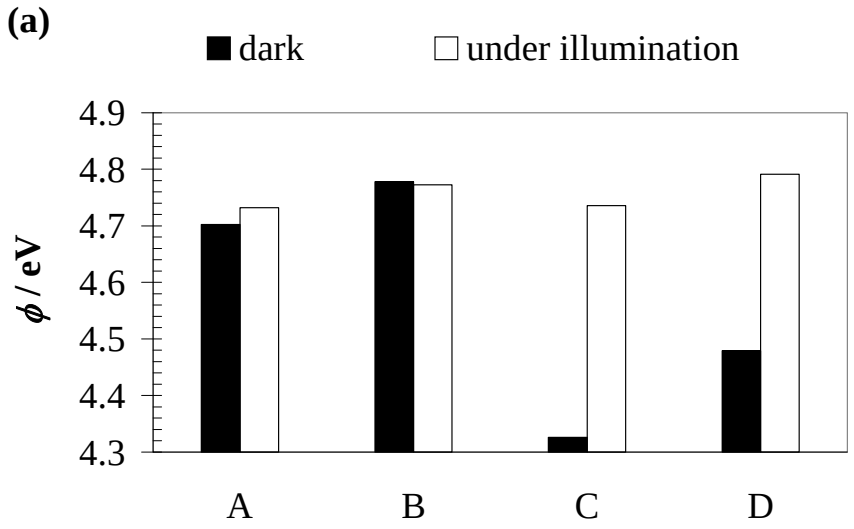

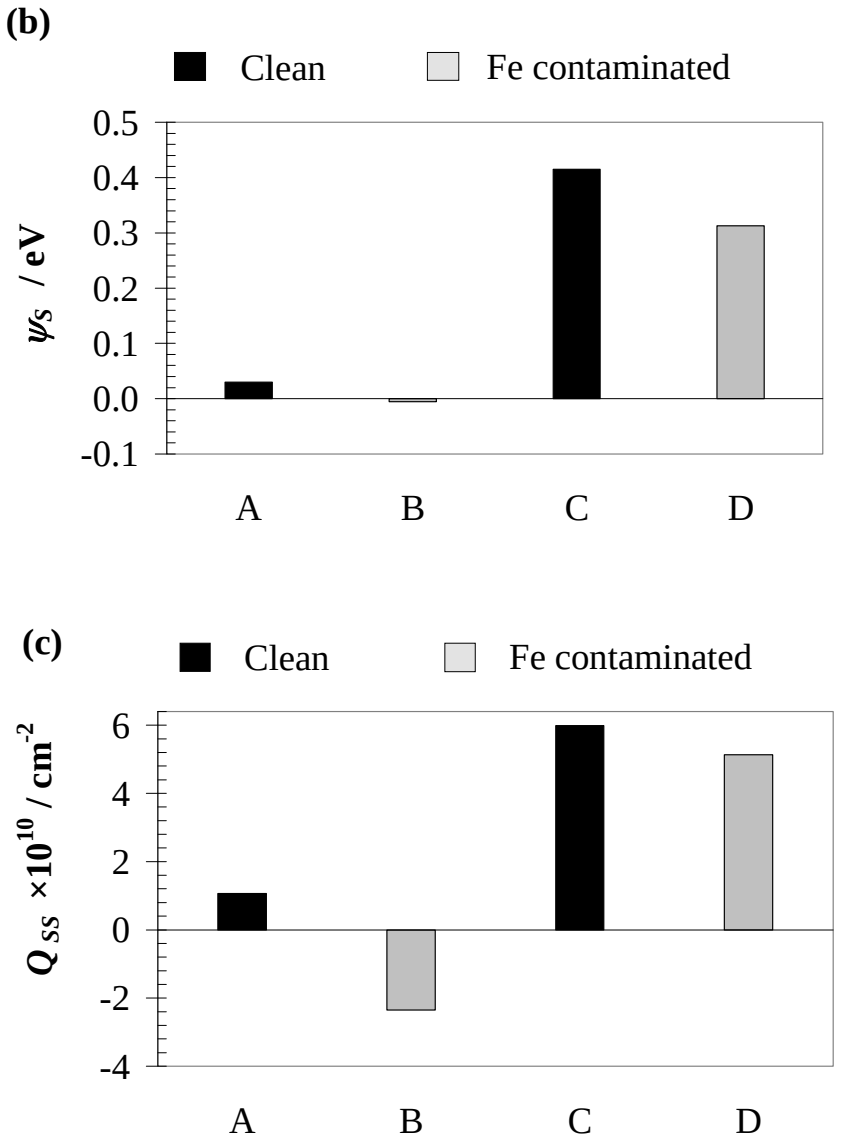

***Figure 6-11**. Summary of the wafer scans giving average values for (a) work function (dark, illumination), (b) surface potential and (c) surface charge.*

6.3.3 Discussion

The results obtained from the SPV measurements on the differently treated Si wafers agree, in general, with those published in the literature as pointed out above. However, there are important limitations to this method that should be considered; a comprehensive analysis of the technique and its restrictions is e.g. given in [12].

First, in order to conclude that the measured SPV indeed equals the surface potential, we have to ensure that photo-saturation really is achieved. As seen from figure 6-5, the injection level required for SPV saturation for a typical depletion layer is approximately 100 to 1000. This however may require very high illumination intensities especially in semiconductors with low carrier lifetimes such as, generally, direct semiconductors. For example, the SPV versus photon flux curve in figure 6-8 shows that saturation is not completely attained but can be assumed within approximately 10%.

Secondly, for the analysis of the surface photovoltage it was assumed that the surface charge remains constant upon carrier injection. However, as pointed out in section 6.2.3, a change in surface potential can be induced by both a redistribution of carriers or a change in the surface state population through carrier trapping. In practice, both effects contribute to $\Delta\psi$ where the magnitude and sign of the change in surface charge depends strongly on the ratio of the surface state hole and electron capture coefficients. The effect of a change in the surface charge on the SPV versus η curve is mainly to change the slope of the curve, see e.g. [9, 12] which, in effect, prevents the extraction of surface parameters from the slope of the curve.

Lastly, we have implicitly assumed that the voltage measured upon illumination arises solely from the change in band bending, i.e. the surface photovoltage given in equation 6-49. However, due to the Dember effect [22] a potential drop across the bulk can occur which may have a significant effect onto the SPV versus η curve for high injection levels [12]. The Dember voltage ψ_D arises from the different diffusion coefficients of electrons and holes in semiconductors: electrons tend to diffuse faster than holes giving rise to an internal electrical field and thus ψ_D which therefore is of positive sign irrespective of the type of the semiconductor doping. Thus for a p-type semiconductor

with a depletion or inversion type surface layer, i.e. $\psi_S > 0$, the Dember voltage causes a decrease in the SPV versus η curve or even an inversion of its gradient. For n-type materials in depletion on the other hand, ψ_D is of the same sign as $\Delta\psi$ and may thus prevent the SPV versus η curve from saturating. Therefore, if ψ_D is not negligible compared to $\Delta\psi$ and ψ_D is not known, the surface potential ψ_S cannot be obtained with this method.

We can therefore conclude that, although the technique is relatively easy to implement, it is subject to a variety of problems and even misinterpretations and is not applicable in all cases; a review of possible solutions to circumvent these problems is given in [12]. Therefore, a second method was tested, see section 6.4, where ψ_S is extracted from the frequency dependence of the surface photovoltage.

6.4 THE AC–SPV MEASUREMENT

6.4.1 Outline

Another approach using the surface photovoltage to obtain parameters of the semiconductor surface has been established by Munakata [6]. The method is based on the frequency dependence of the surface photovoltage, shortly termed the ac-SPV method. We briefly outline the theory of the ac-SPV and discuss 2 different approaches for its measurement via: (i) a high input impedance amplifier and (ii) the Kelvin probe input stage. Examples of ac-SPV measurements and the resulting surface potential and surface charge calculated from the derived ac-SPV equations are given.

6.4.2 Semiconductor Surface Impedance

The basic electrical circuit of a semiconductor surface is shown in figure 6-12 where the surface conductance g_S and the capacitance c_S are components of the surface impedance z_S, which is thus given by

$$z_S = \frac{1}{g_S + j \cdot 2\pi f \cdot c_S} \qquad 6\text{-}52$$

where f is the modulation frequency of the light illuminating the semiconductor surface and thereby inducing the photocurrent density J_{ph}. The use of the lower-case symbols for g and c implies that the quantity is given in the respective dimension per unit area.

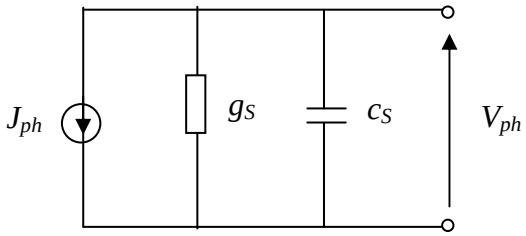

***Figure 6-12**. Basic electric circuit of a semiconductor surface under photo excited carrier injection.*

The photons of the illuminating light beam are absorbed in the semiconductor thereby creating electron hole pairs if $E_{ph} > E_g$, where E_{ph} is the energy of the photon at wavelength λ_{ph}. The carriers created in the SCR are immediately separated due to the electric field thus reducing the surface potential and inducing V_{ph}. These carriers however are lost through various mechanisms, i.e. recombination, diffusion and trapping, and are re-supplied by J_{ph}. Carrier storage and annihilation mechanisms can be described by various capacitances and conductances that compose the surface impedance z_S. The photovoltage V_{ph} is related to the surface impedance by

$$V_{ph} = z_S \cdot J_{ph} \ . \qquad 6\text{-}53$$

We note that V_{ph} is linearly proportional to J_{ph} only for voltages less than the equivalent thermal voltage, i.e. $V_{ph} < kT/q$ which is ≈26mV at 300K [6].

We discuss in the following the components of this circuit and derive the equations that relate the surface potential ψ_S of the semiconductor to the measured ac-photovoltage $V_{ph.}$ We will restrict the analysis to a p-type semiconductor in depletion or weak inversion which corresponds to the parameters of the p-type Si(100) wafer samples described in section 6.3. A complete analysis of the ac-SPV is given by Munakata in [6] for strong inversion, in [23] for depletion or weak inversion and in [24] for accumulation layers.

A. Photocurrent

The current induced in the semiconductor is related to the incident photonflux Φ by

$$J_{Ph} = q \cdot \Phi(1-\Theta) \cdot \gamma \qquad \textit{6-54}$$

where Θ is the reflection coefficient and the factor γ accounts for the fact that carriers may be induced in both the SCR and the bulk of the semiconductor. Whereas carriers created in the SCR supply J_{ph} directly, electron hole pairs in the bulk have to diffuse to the SCR in order to contribute to J_{ph} where they partly recombine before reaching the edge of the SCR. The factor γ thus depends on the light absorption coefficient α, the width of the space charge layer w and the diffusion length of the minority carriers, i.e. electrons, L_n, and is given by [8]

$$\gamma = 1 - \frac{e^{-\alpha w}}{\alpha L_n + 1} \; . \qquad \textit{6-55}$$

The diffusion length L_n is related to the minority carrier lifetime τ_n and the diffusion coefficient D_n for electrons via

$$L_n = \sqrt{D_n \cdot \tau_n} \ . \qquad \textit{6-56}$$

The absorption coefficient for silicon can be calculated using the semi-empirical equation given in [25]:

$$\alpha(\lambda) = \left(84.732/\lambda - 76.417\right)^2 \qquad \textit{6-57}$$

with the units for α in cm^{-1} and for λ_{ph} in μm. A graphical representation of expression 6-57 is plotted in figure 6-13. We see that for a wavelength of e.g. 650nm, the penetration depth α^{-1} is 3.4μm. For comparison, the width of the SCR of p-type silicon at 300K with doping density $N_A = 7\times10^{14}$ cm^{-3} for a surface potential of 420mV is e.g. ~0.89μm, see figure 6-4. The coefficient γ resulting from equation 6-55 is plotted in figure 6-14 for different wavelengths. We see that for typical carrier lifetimes in silicon of 10μs to 1ms γ can be approximated by 1 for light of $\lambda_{ph} \leq 650$nm and only plays a role if light in the infrared region is used.

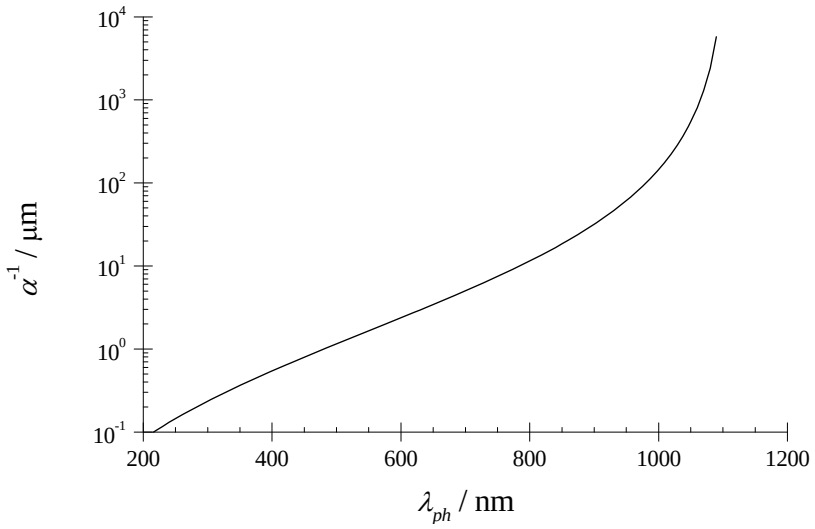

Figure 6-13*. Penetration depth of light in Si according to equation 6-57.*

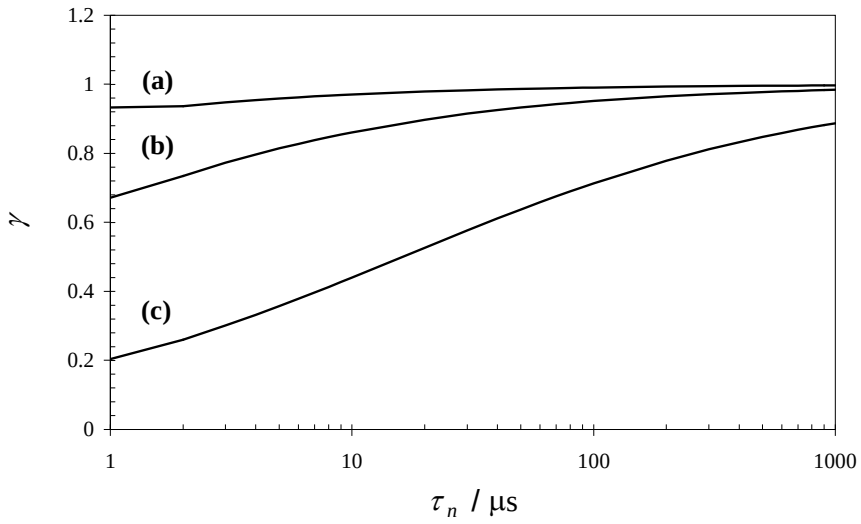

Figure 6-14*. Photocurrent coefficient γ for p-type silicon at 300K with doping density $N_A = 7\times10^{14}$ cm^{-3} as a function of the minority carrier lifetime and wavelength of the incident light: (a) 650nm, (b) 900nm and (c) 1000nm.*

B. Depletion Layer Effect

The capacitance of the space charge layer in depletion or weak inversion, c_{dp}, is given by

$$c_{dp} = \frac{\varepsilon_S}{w}, \qquad 6\text{-}58$$

where ε_S is the permittivity of the semiconductor and w the width of the SCR which is given in equation 6-33. This capacitance is the dominating one for the depletion and weak inversion layer impedance. The carrier loss in the depletion layer is due to recombination of carriers and is expressed by the depletion layer conductance [6]

$$g_{dp} = \frac{1}{2}\cdot\frac{q\beta\cdot n_i w}{\tau_w}\int_0^1 \frac{di}{\cosh\left[\beta\psi_s(1-i)^2 - \beta E_F\right]+1} \qquad 6\text{-}59$$

where τ_w is the minority carrier lifetime in the depletion layer. However, since there are only few mobile carriers in the depletion layer, the loss of carriers through volume recombination and thus g_{dp} in the SCR is normally negligible.

C. Diffusion of Minority Carriers

Due to the carrier concentration gradient in the SCR, i.e. $n_S > n_0$ in a depleted p-type semiconductor, minority carriers diffuse from the surface to the bulk. This current is supported by the lowering of the surface potential. The diffusion current of minority carriers towards the bulk is, together with the recombination current, keeping pace with the minority carrier drift current towards the surface that is supplied by the photocurrent J_{ph}. The minority carrier diffusion capacitance, c_{mn}, and conductance, g_{mn}, are given by [8]

$$c_{mn} = \frac{q\beta L_n n_i}{2} \cdot \mathrm{e}^{-\beta E_F} \qquad 6\text{-}60$$

$$g_{mn} = q\beta v_n n_i \cdot \mathrm{e}^{-\beta E_F} \qquad 6\text{-}61$$

where v_n is the minority carrier diffusion velocity:

$$v_n = \frac{D_n}{L_n} \ . \qquad 6\text{-}62$$

D. Majority Carriers Conductance

To formulate the conductance for the majority carriers we have to consider the various majority carrier currents in the SCR. The concentration gradient of the majority carriers causes a diffusion current from the bulk towards the surface that is enhanced by the lowering of the surface barrier. Opposed to this current is the flow of majority carriers

towards the bulk due to the electrical field in the depleted SCR. Both currents must be equal in equilibrium. However, a net current towards the surface, J_{mj}, occurs with J_{ph} which induces V_{ph}. We can therefore formulate the majority carrier conductance as

$$g_{mj} = \frac{J_{mj}}{V_{ph}} \quad . \qquad \textit{6-63}$$

The majority carrier current derived by Munakata, g_{mj} can be written as [23]

$$g_{mj} = qp_S\mu_p \cdot \mathrm{e}^{\frac{-E_S}{E_0}} \cdot \frac{1-\mathrm{e}^{-\beta\psi_S}+\frac{n_0}{p_0}\left(\mathrm{e}^{\beta\psi_S}-1\right)}{\sqrt{2}L_{Dp}F_p(\beta,\psi_S,n_0,p_0)} \qquad \text{6-64.}$$

where μ_p is the mobility of holes and the hole concentration at the surface, p_S, is given by equation 6-17 if ψ is set to the surface potential ψ_S. The electric field at the surface, E_S, is given via equation 6-30 and E_0 is a characteristic field intensity defined by:

$$E_0 = \frac{v_{pdm}}{\mu_p} \qquad \textit{6-65}$$

where v_{pdm} is the saturated maximum hole drift velocity which is for Si at 300K $v_{pdm} = 5.34\times10^4$ ms^{-1} [26]. In the depletion and weak inversion region g_{mj} is the main conductance and decreases almost exponentially with ψ_S [23]. It is therefore too low to have any effect on the conductance in the strong inversion layer.

E. Interface Trapping Effects

Due to the change in the surface potential upon illumination the Fermi-level at the surface is shifted with respect to its position within the bandgap. This affects the occupancy of states at the interface that are within a few *kT* from the Fermi-level, see section 6.2.1, thus causing an exchange of charge of these states with the valence and

the conduction band, respectively. These charge transitions are associated with a typical time constant τ_{it} which depends, for p-type semiconductors in depletion or weak inversion, on the concentration of holes at the surface since the capture of majority carriers is the rate limiting step in this process [27]. This time constant is given by:

$$\tau_{it} = \frac{1}{v_t \cdot \sigma_p \cdot p_S} \qquad 6\text{-}66$$

where v_t is the average thermal velocity equal to 10^7 cm·s^{-1}, σ_p is the capture cross section of the states for holes which is for Si(100) about 2.2×10^{-16} cm^2 [8, p.386]. The interface trap capacitance, c_{it}, and conductance, g_{it}, are given by [27]

$$c_{it} = \frac{q^2 D_{it}}{2\pi f \cdot \tau_{it}} \cdot \tan^{-1}\left(2\pi f \cdot \tau_{it}\right) \qquad 6\text{-}67$$

$$g_{it} = \frac{1}{2}\frac{q^2 D_{it}}{\tau_{it}} \cdot \ln\left[1+\left(2\pi f \cdot \tau_{it}\right)^2\right] \qquad 6\text{-}68$$

where D_{it} is the interface trap density. Whereas c_{it} decreases with f and is normally negligible at higher frequencies compared to c_{dp}, it may affect the ac-SPV in the frequency region below 1kHz depending on the magnitude of D_{it}.

F. Carrier Recombination Through Interface States

Interface states can also act as recombination centres for carriers in the same way as defects in the bulk. This is associated with a loss of carriers and hence can be presented as a surface recombination conductance g_{Sr} which is given as [28]:

$$g_{Sr} = q\beta \cdot s_f \cdot n_i \qquad 6\text{-}69$$

where s_f is the surface recombination velocity. According to the Shockley-Read-Hall (SRH) statistic [9, 29], the surface recombination depends on the actual concentration of carriers at the surface. Hence, s_f is related to the original surface velocity s_0 by

$$s_f = s_0 \cdot \frac{n_i}{n_S + p_S + 2n_i} \qquad 6\text{-}70$$

where s_0 is given by

$$s_0 = \sigma v_{th} \pi D_{it}\, q/\beta \ . \qquad 6\text{-}71$$

We see that s_f will be at a maximum when the term $(n_S + p_S)$ is at a minimum, which occurs at $\psi_S = \psi_B$, i.e. at the transition from a depletion to a weak inversion layer. In light depletion and strong inversion p_s or n_S are >> n_i and therefore g_{sr} can be neglected as long as D_{it} and hence s_0 is not too high.

F. Simulation of Surface Impedance Components

In order to estimate the effect of each component on the surface impedance we compare their magnitude for a set of assumed parameters. The semiconductor should be, as before, of p-type Si(100) with $N_A = 7\times10^{14}$ cm^{-3} and exhibiting a weak inversion layer with $\psi_S = 420$mV. The minority carrier lifetime is assumed to be 100μs for both bulk and SCR interface and the interface trap density should be $D_{it} = 1\times10^{16}$eV^{-1}m^{-2}.

We see from figure 6-15 that c_{dp} >> c_{mn} in the depletion and weak inversion region and hence the minority carrier diffusion capacitance can be generally neglected. As pointed out before, c_{it} is decreasing with frequency and therefore the depletion layer capacitance c_{dp} is dominating at higher frequencies, see figure 6-16. However, in the lower

frequency region the interface trap capacitance may contribute to the surface impedance depending on the magnitude of D_{it}.

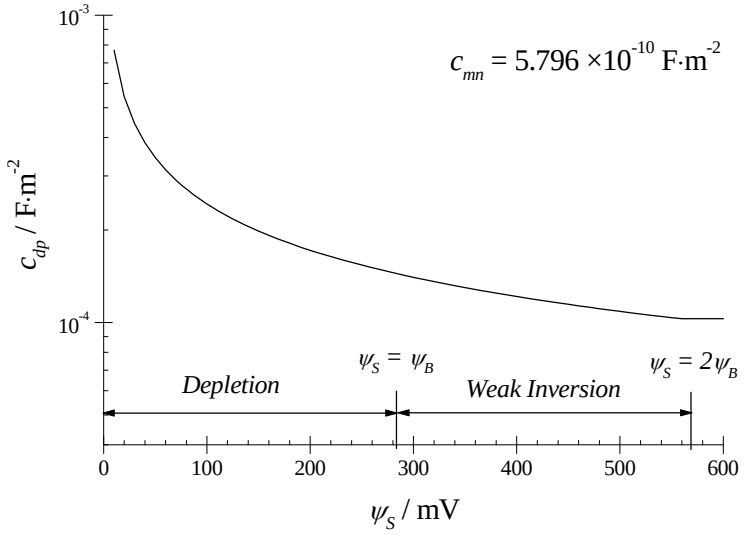

***Figure 6-15**. Depletion layer capacitance as a function of the surface potential. Also shown is, for comparison, the minority carrier diffusion capacitance c_{mn}.*

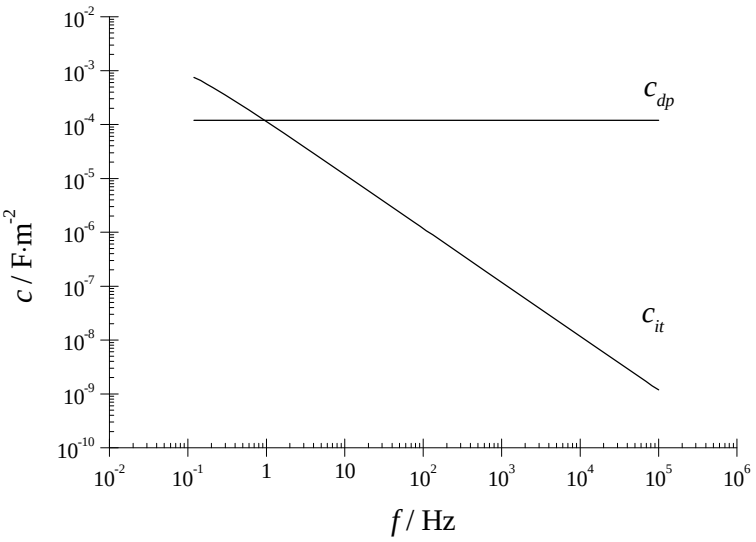

***Figure 6-16**. The depletion layer capacitance in comparison to the frequency dependent interface trap capacitance under the assumptions made above.*

The various contributions to the surface conductance are plotted in figures 6-17 and 6-18. We see that the conductances g_{mn}, g_{dp} and g_{it} can normally be neglected. The majority carrier conductance decreases exponentially with the surface potential but is

the dominating one in depletion and weak inversion. The surface recombination conductance g_{sr} has a maximum at $\psi_S = \psi_B$ and may contribute to the surface impedance only for very high trap densities D_{it}.

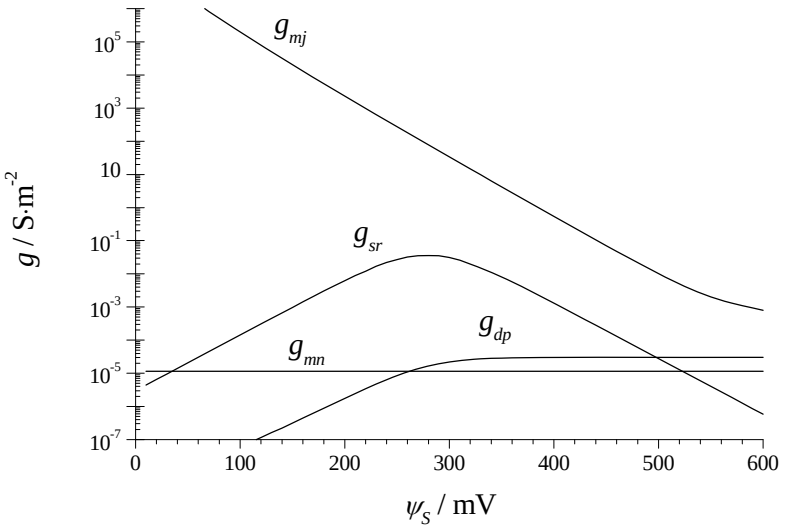

***Figure 6-17**. The contribution of the various conductances in the depletion and weak inversion region as a function of the surface potential.*

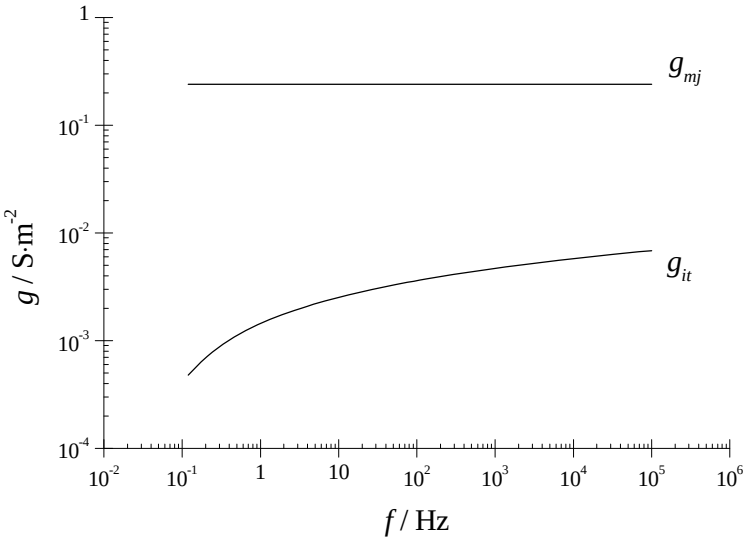

***Figure 6-18**. The majority carrier conductance g_{mj} in comparison to the frequency dependent interface trap conductance g_{it} under the assumptions made above.*

G. Determination of the Surface Potential

From the discussion above we have seen that in the depletion and weak inversion region the surface impedance z_S is likely to be determined by the majority carrier conductance g_{mj} and the depletion layer capacitance c_{dp}. Equation 6-52 can therefore be approximated by

$$z_S = \frac{1}{g_{mj} + j \cdot 2\pi f \cdot c_{dp}} \quad . \qquad 6\text{-}72$$

The surface photovoltage induced by a photonflux of 1×10^{12} $cm^{-2}s^{-1}$ with a reflection coefficient of 0.3 is plotted in figure 6-19. We see that in the low frequency region, i.e. <30Hz, the surface impedance is governed by the conductance g_{mj} whereas for frequencies >1kHz z_S is governed by the imaginary part in equation 6-72. Therefore, the majority carrier conductance and the depletion layer capacitance can be obtained from the frequency dependence of V_{ph} and hence the surface potential via equations 6-64 and 6-58, respectively.

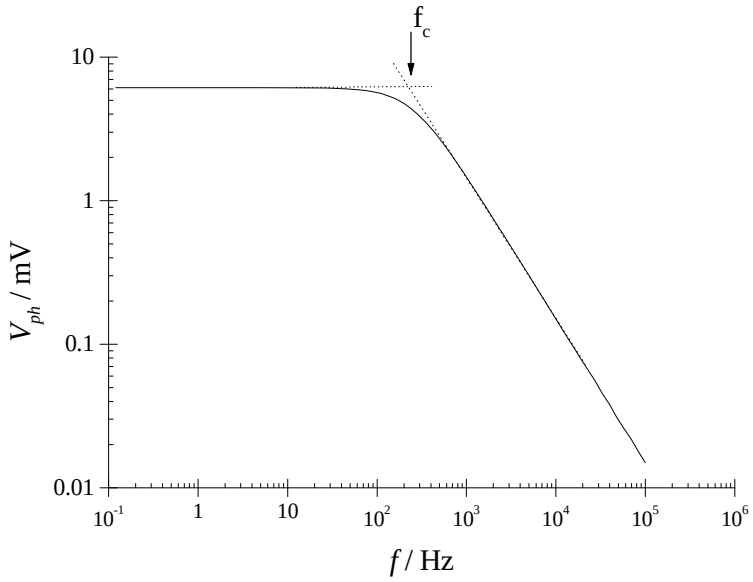

Figure 6-19*. Frequency dependence of the surface photovoltage with f_c denoting the cutoff frequency.*

However, the technique outlined above hinges on the precise knowledge of the photocurrent which depends not only on the photonflux Φ but also on the reflection coefficient Θ of the surface and the factor γ, which are often not known exactly. A more elegant method was proposed by Munakata [30] using the cutoff frequency f_c, as indicated in figure 6-19, to determine the surface potential ψ_S.

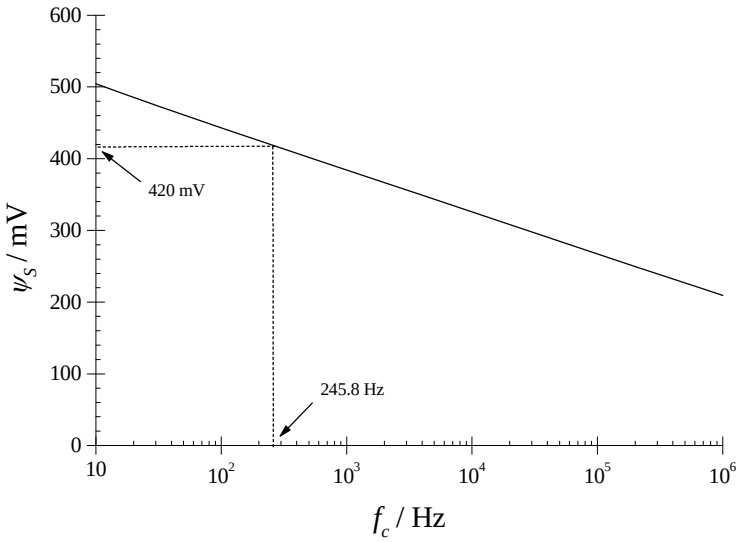

***Figure 6-20**. The surface potential ψ_S as a function of the cutoff frequency of the surface photovoltage.*

If the surface impedance is solely governed by the majority carrier conductance and depletion layer capacitance as expressed in equation 6-72 then the cutoff frequency of the transfer function is given as [30]

$$f_c = \frac{1}{2\pi}\frac{g_{mj}}{c_{dp}} \quad . \qquad \textit{6-73}$$

Since both g_{mj} and c_{dp} are uniquely determined by ψ_S, the surface potential can be obtained by numerically or graphically solving equation 6-73. The graphical solution of this relation is shown in figure 6-20. We find that the cutoff frequency f_c of 245.8Hz from figure 6-19 corresponds to the initially assumed surface potential of ψ_S = 420mV.

6.4.3 Experiment

A. Setup

The experimental setup that was used to measure the ac-SPV is shown schematically in figure 6-21. The semiconductor sample is illuminated by a sine wave modulated light emitting diode (LED) of wavelength λ_{ph} = 626nm through a neutral density filter, a semitransparent conducting probe and a mica spacer of thickness 100µm. The probe has a conducting indium tin oxide (ITO) layer on a glass substrate which has an area of S_{Probe} = 15mm × 12mm = 180mm^2 The light beam from the LED is focused onto an area S_0 = 19.6mm^2 at the sample surface. The SPV signal picked up by the probe is fed into a variable input stage. Two different designs were tested: a low impedance I-V converter equivalent to the input stage of the Kelvin probe and a very high impedance amplifier. Both designs will be described in detail below. The amplitude and phase of the SPV signal is finally read at the lock-in amplifier (LIA, EG&G Model 5101). Parts of the p-type Si(100) wafers C and D that are described in section 6.3.1 were used as samples.

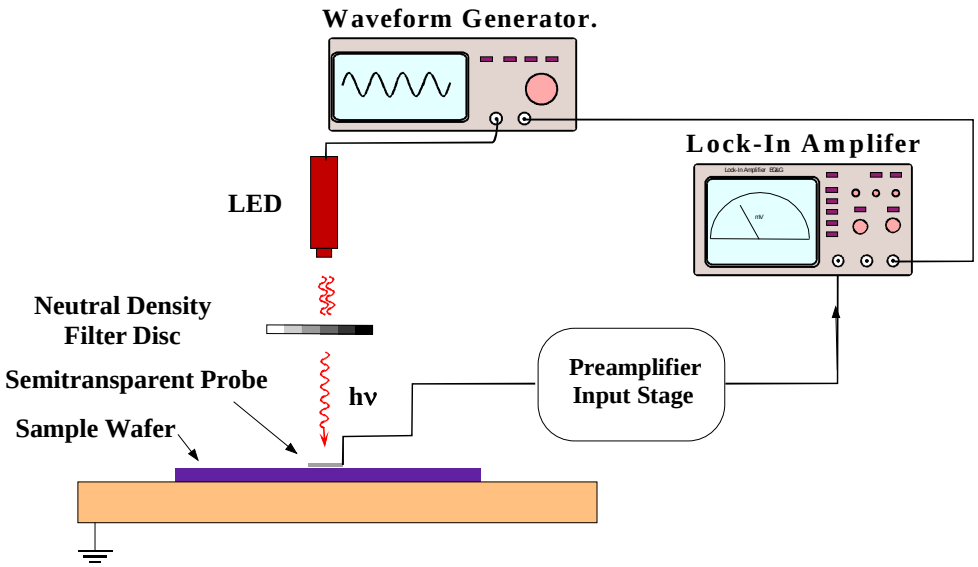

***Figure 6-21**. Schematic of the ac-SPV measurement setup.*

B. Equivalent Circuit for the ac-SPV Measurement

The equivalent electrical circuit for the measurement of the ac-surface photovoltage is shown in figure 6-22. The subscript '0' refers to the parameters for the voltage generating area S_0 which we assume to be equal to the illuminated area [6]. Thus C_0 is the capacitance between the probe and the wafer surface for his area, where the relative permittivity of the mica spacer is $\varepsilon_r \approx 6$. Z_0 is the respective wafer impedance, composed of the surface impedance, oxide layer capacitance and wafer resistance.

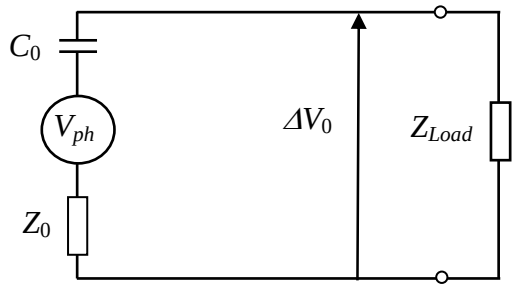

***Figure 6-22**. Equivalent electrical circuit for the ac-SPV measurement.*

A further capacitance should be included in the circuit if the back side of the wafer is capacitively coupled to the sample holder. However, this coupling capacitance is normally much higher compared to the other series capacitances in the circuit and thus can be neglected. Further, since the probe coupling capacitance is very small compared to the wafer impedance due to the relatively large spacing between probe and the wafer surface, i.e. 100μm compared to an approximately 1μm depletion layer, Z_0 is normally negligible compared to C_0.

In order to obtain the correct amplitude of the photovoltage from the measurement, we introduce the voltage transfer function $H_0(\omega)$ which is defined as the ratio of the output to the input voltage:

$$H_0(\omega) = \frac{\Delta V_0}{V_{ph}} \ . \qquad 6\text{-}74$$

Taking further into account the inequality of the probe and photovoltage generating area S and S_0, we can relate the experimentally obtained transfer function $H(\omega)$ to $H_0(\omega)$:

$$\frac{H(\omega)}{H_0(\omega)} = \frac{S_{Probe}}{S_0} \ , \qquad 6\text{-}75$$

where the ratio of the surface areas in the above equation is 9.2 for this setup. Thus the photovoltage can be obtained via

$$V_{ph} = H(\omega) \cdot \Delta V_0 \cdot \frac{S_0}{S_{Probe}} \ . \qquad 6\text{-}76$$

The amplitude of the transfer function can be obtained analytically by considering the reduced circuit shown in figure 6-23. We see that this circuit effectively acts as a voltage divider:

$$H(\omega) = \frac{Z_{Load}}{Z_{Source} + Z_{Load}} \qquad 6\text{-}77$$

where the source impedance reduces to the reactance of an ideal capacitor:

$$Z_{Source} = X_C = \frac{1}{j\omega C_{Probe}} \ . \qquad 6\text{-}78$$

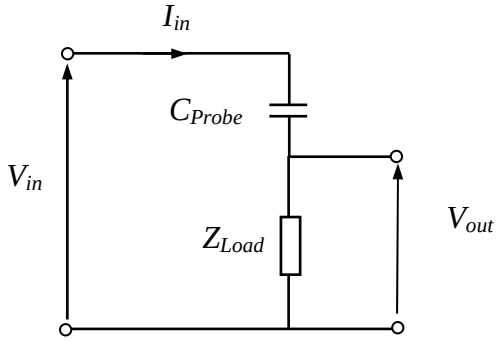

Figure 6-23*. Reduced equivalent electrical circuit of the ac-SPV setup to determine the voltage transfer function H(ω).*

We discuss in the following the transfer function $H(\omega)$ of the measurement circuit for two different configurations, i.e. with a very low and a very high load impedance Z_{Load}.

C. Low Impedance Input Stage

We will first derive the transfer function of the low impedance amplifier which is in fact equivalent to the I-V converter input stage of the Kelvin probe, see chapter 2. The input stage is based on an operational amplifier (op-amp) as shown in figure 6-24. In this configuration, the inverting input of the op-amp is at virtual ground potential, i.e. its input impedance is virtually zero: $Z_{load} \approx 0$ [18]. Consequently, the current I_{in} can be approximated by the short circuit current of the circuit:

$$I_{in} = \frac{V_{in}}{Z_{Source}} \ . \qquad 6\text{-}79$$

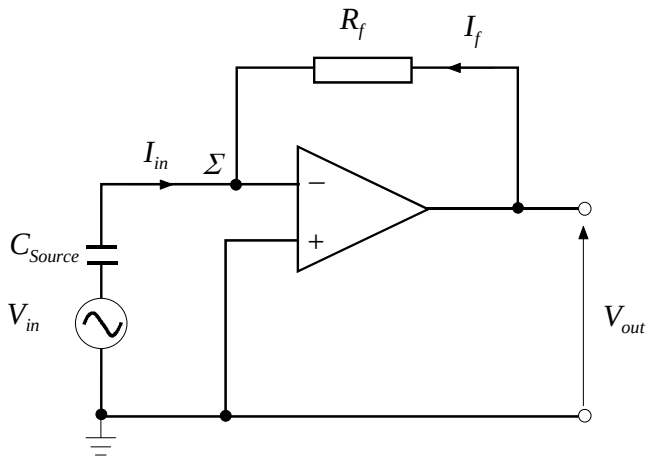

Figure 6-24*. Schematic of the low impedance ac-SPV measurement circuit which is equivalent to the Kelvin probe input stage.*

Since the input of an ideal operational amplifier draws no current, the sum of all currents at the summing point Σ of the I-V converter must be zero, i.e.:

$$I_{in} - I_f = 0 \qquad 6\text{-}80$$

where I_f is the feedback current. With the relation for the feedback resistance R_f

$$R_f = \frac{V_{out}}{I_f} \qquad 6\text{-}81$$

and equations 6-79 and 6-80, the ratio of the output to input voltage, and thus $H(\omega)$ can be given by

$$H(\omega) = \frac{V_{out}}{V_{in}} = \frac{R_f}{Z_{Source}} \qquad 6\text{-}82$$

and with equation 6-78 as

$$H(\omega) = R_f C_{Probe} \cdot j\omega \ . \qquad 6\text{-}83$$

where

$$\left|H(\omega)\right| = R_f C_{Probe} \cdot \omega \qquad 6\text{-}84$$

is the amplitude of the transfer function. From the expression above it can be seen that the function is proportional to the frequency of the signal. The factor $2\pi R_f \cdot C_{Probe}$ is the slope of the curve of $H(\omega)$ versus f. The imaginary constant j expresses a phaseshift of 90° between the output and input signal.

The op-amp OP-42 (Analog Devices) was used in this setup with a feedback resistance of $10^7\Omega$. The capacitance of the probe with the parameters given above is approximately 0.1nF. Thus the factor $2\pi R_f \cdot C_{Probe}$ is equal to 6×10^{-3}s. The transfer function determined for this setup with a sinusoidal input voltage is plotted in figure 6-25. We see from the equation of the power-type least square fit given for the linear region of the curve that $|H(\omega)|$ is indeed proportional to f where the slope of the curve is 1×10^{-3}s which is comparable with the estimated factor. The difference might be due to air gaps in the probe-sample arrangement thus reducing its capacitance.

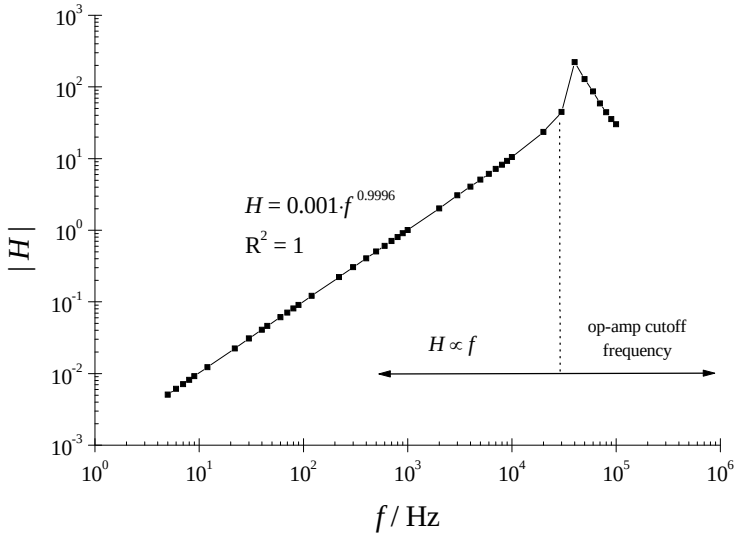

Figure 6-25 *. Experimental voltage transfer function of the ac-SPV measurement circuit using the low impedance amplifier input stage.*

Considering the usable frequency range of this circuit we see that the utilisation of this input stage at low frequencies, i.e. for f □ 50Hz and input voltages of typically [10mV might be restricted since the transfer function and hence the amplitude of the output voltage is very low. On the other hand, since the ac-SPV is typically proportional to f^{-1} for f ⁄ 100Hz, the decreasing input voltage is effectively compensated by the increasing transfer function which thus improves the signal detection at higher frequencies and its signal to noise ratio. The high frequency limit of this circuit is set by the bandwidth of the op-amp. Due to the high amplification, in this case of $10^7 V \cdot A^{-1}$, the upper cutoff frequency is rather low, i.e. ≈30kHz as indicated in figure 6-25. However, since this circuit is equivalent to the input stage of the Kelvin probe it offers the possibility of implementing the ac-SPV measurement mode thus diversifying the application range of the probe.

D. High Impedance Input Stage

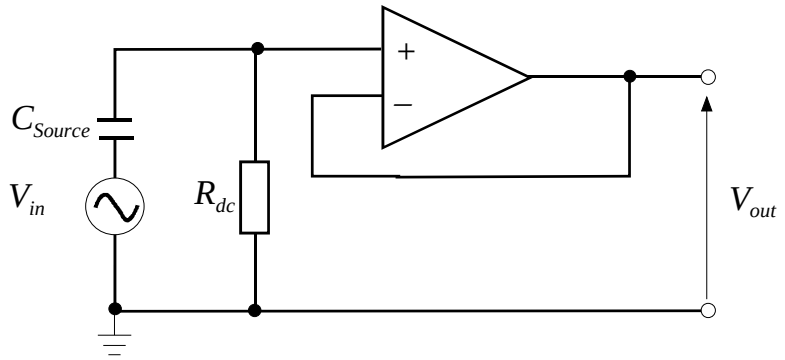

***Figure 6-26**. High input impedance unity gain buffer amplifier where R_{dc} = 10GΩ provides a dc-current path to compensate for the non-zero input current of the op-amp.*

In the second configuration a unity gain buffer op-amp with a high impedance JFET input (MAXIM, MAX4005) having a bandwidth of 950MHz was used as the input stage. The resistor R_{dc} = 10GΩ provides the return path for the dc-current to ground to compensate the input current of 10pA of the MAX4005 buffer amplifier since the input is capacitively coupled. To obtain the transfer function of this amplifier we thus take the input impedance Z_{Load} into account which is given by a parallel combination of the R_{Load} and C_{Load} :

$$Z_{Load} = \left[\frac{1}{R_{Load}} + \frac{1}{(j\omega C_{Load})^{-1}} \right]^{-1} \qquad 6\text{-}85$$

We can assume that R_{Load} is dominated by the resistor R_{dc}. With equations 6-78 and 6-85 the ratio of Z_{Source} and Z_{Load} can be expressed by

$$\frac{Z_{Source}}{Z_{Load}} = \frac{C_{Load}}{C_{Source}} + \frac{1}{j\omega \cdot C_{Source} R_{Load}} \ . \qquad 6\text{-}86$$

Substituting expression 6-86 into 6-77 the amplitude of the transfer function is given by

$$|H(\omega)| = \left[\left(\frac{C_{Load}}{C_{Source}} + 1 \right)^2 + \left(\frac{1}{\omega \cdot C_{Source} R_{Load}} \right)^2 \right]^{-\frac{1}{2}} \qquad 6\text{-}87$$

A plot of the above equation versus frequency is shown in figure 6-27 using values of C_{Source} = 100pF, C_{Load} = 10pF and 100MΩ and 10GΩ for R_{dc}. We see that in the low frequency region the transfer function is governed by the second, frequency dependent part in equation 6-87. The low cutoff frequency at the –3dB point, $f_{c,low}$, can thus be obtained via

$$f_{c,low} = \frac{1}{2\pi C_{Source} R_{Load}} \qquad 6\text{-}88$$

Therefore, in order to obtain a low frequency cutoff, the values for C_{Source} and R_{Load} should be as high as possible. We can e.g. clearly observe the effect of the load resistance in figure 6-27, which is equal to R_{dc}. At a value of R_{dc} = 100MΩ the low cutoff frequency is at ~14Hz whereas with R_{dc} = 10GΩ f_c is at ~0.14Hz.

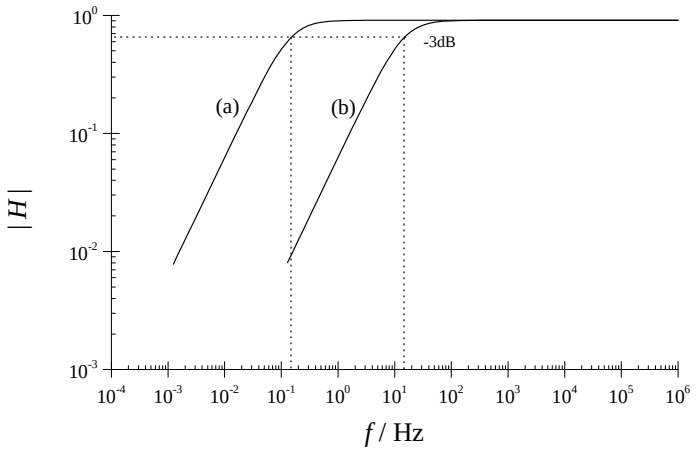

***Figure 6-27**. Low frequency cutoff of the voltage transfer function for load resistor values of (a) 10GΩ and (b) 100MΩ and capacitor values of C_{Source} = 100pF and C_{Load} = 10pF.*

Above the cutoff frequency the transfer function is independent of frequency and only a function of the ratio of C_{Load} to C_{Source}. Thus a high source and a low load capacitance are preferable to obtain a high transfer function in this frequency region. We see that e.g. if $C_{Load} = C_{Source}$, $|H(\omega)|$ equals 0.5. It should also be noted that, although not shown in the circuit diagram in figure 6-26, the cable connection from the probe to the amplifier input is an integral part of the circuit with its own resistance and capacitance. Although the resistance is normally negligible, the cable capacitance is in parallel to the amplifier input capacitance C_{Load} and hence must be added to its value. Therefore, this connection should be kept as short as possible.

The high frequency response of the circuit is then only limited by the bandwidth of the buffer op-amp, which is 950MHz for the MAX4005, and any subsequent voltage or lock-in amplifier. The experimentally obtained transfer function of this input stage and, for comparison, of the low impedance is plotted in figure 6-28. We can see that the transfer function is essentially flat in the measurable frequency range of the EG&G 5101 LIA, i.e. from 5Hz to 100kHz with a value of $|H|$ of approximately 0.2. We can thus conclude that the transfer function of the buffer amplifier input stage strongly depends on its input impedance. While in the low frequency region the high impedance input seems the better choice, for frequencies above around 300Hz the I-V converter configuration exhibits, within the usable bandwidth, the higher value of $|H|$.

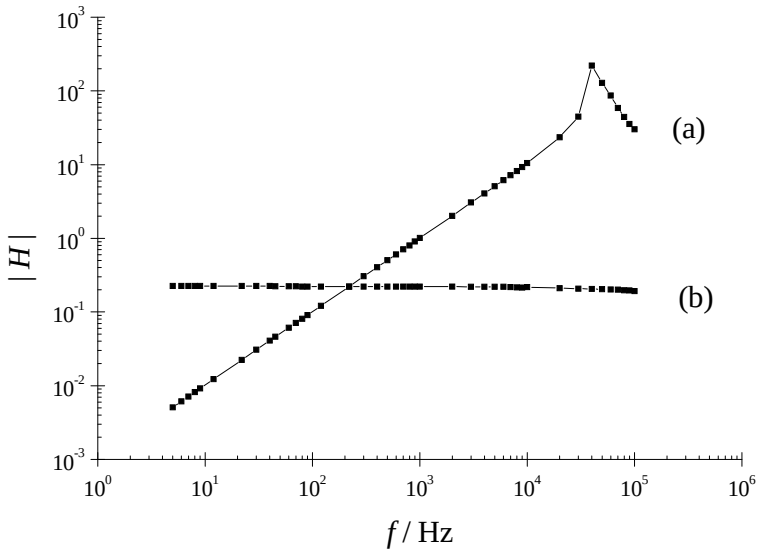

Figure 6-28*. Voltage transfer functions of both the (a) low and (b) high input impedance amplifier stages.*

6.4.4 Results

The ac-photovoltage measured as a function of the illumination intensity is plotted in figure 6-29. We find an almost linear increase in V_{ph} at low intensities turning into saturation for $\Phi / 10^{15} \mathrm{cm}^{-2}\mathrm{s}^{-1}$. This behaviour is similar to the SPV increase measured under constant illumination with the Kelvin probe. A more detailed plot of the photovoltage in the low illumination intensity region is shown in figure 6-30 for modulation frequencies of 10Hz and 2kHz. These correspond to the frequency regions where the surface impedance is governed by the conductance and reactance, respectively. We see that the linear relationship of the V_{ph} with Φ holds well up to 10mV for both cases but deviations from linearity are clearly observed for photovoltages above 20mV.

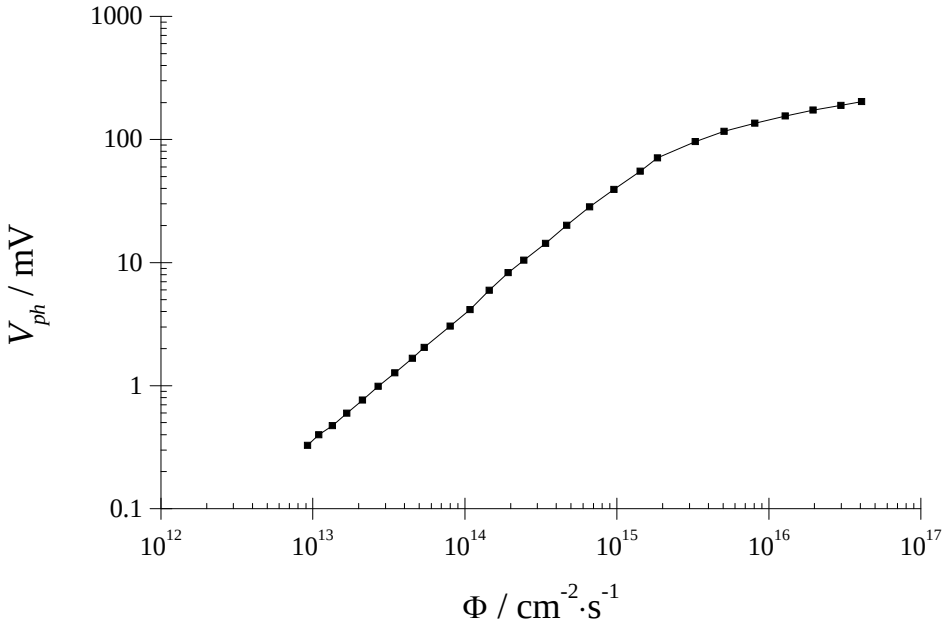

***Figure 6-29**. Photovoltage increase with illumination intensity measured with the high input impedance input stage on sample C where the light signal is modulated with a sinusoidal waveform of f = 2kHz.*

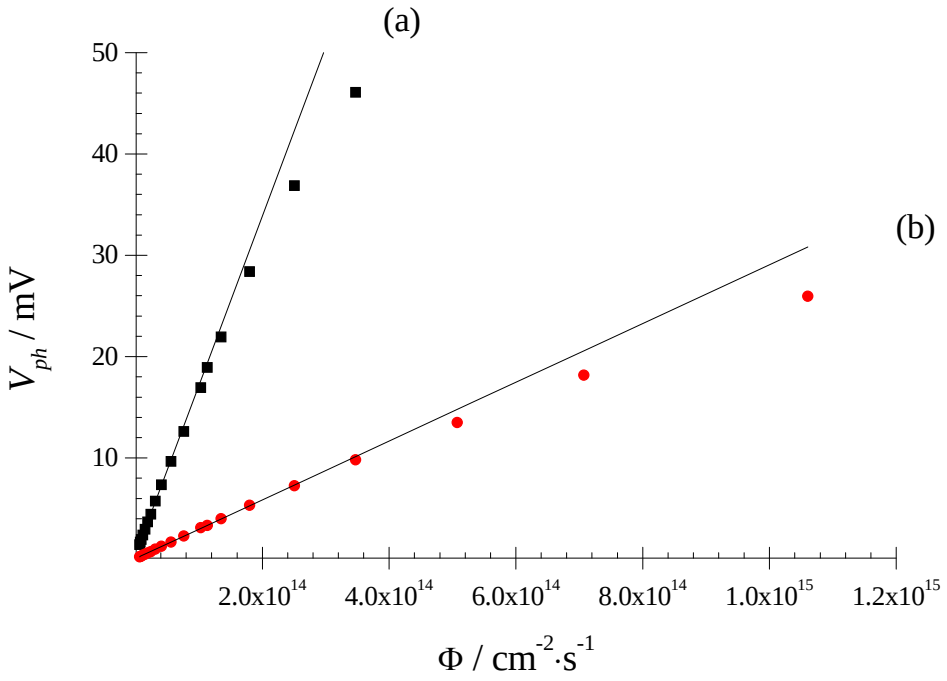

***Figure 6-30**. Photovoltage as a function of the photonflux in the low illumination intensity region for light modulation frequencies of (a) 10Hz and (b) 2kHz. The straight lines are extrapolated linear fit functions of the measured data for V_{ph} < 10mV.*

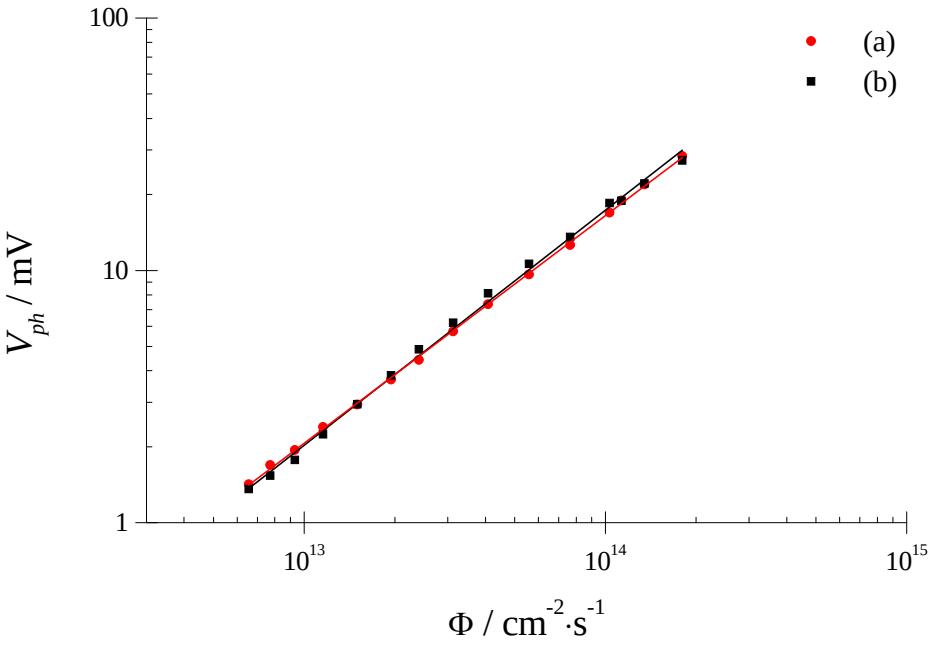

***Figure 6-31**. The photovoltage as a function of the photonflux measured with (a) the low impedance I-V converter input stage the and (b) high impedance input amplifier.*

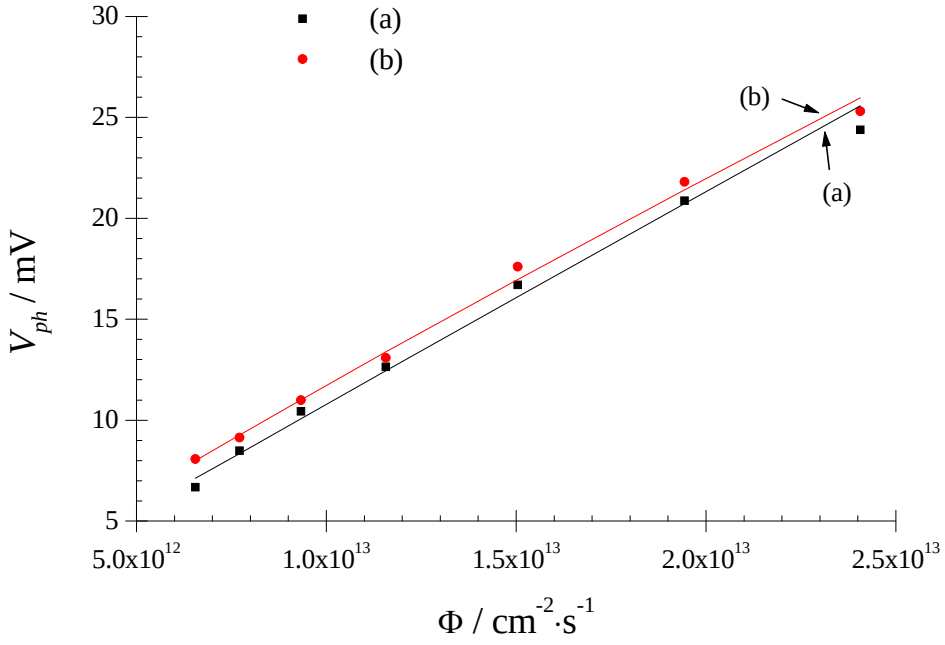

***Figure 6-32.** The photovoltage as a function of the photonflux measured with (a) the ac-SPV method at a modulation frequency of 10Hz and (b) under constant illumination with the Kelvin probe.*

A comparison of the photovoltage measured on sample C with the two different input stages is plotted in figure 6-31 via the photovoltage versus photonflux curve. The light signal was modulated with a frequency of 200Hz. We can conclude that, within the measurement error, both methods yield the same results and thus can be used equally. Further, as seen from the ac-SPV theory, the photovoltage in the low frequency region is governed by the majority carrier conductance g_{mj} and is thus independent of frequency, see also figure 6-33 below. Therefore the ac-SPV at low frequencies should be equal to the photovoltage under constant illumination as measured by the Kelvin probe. The curve plotted in figure 6-32 shows that this is indeed the case. Thus the majority carrier conductance g_{mj} can be obtained from the slope of the dc-SPV curve in the low injection region if the photonflux Φ is known exactly.

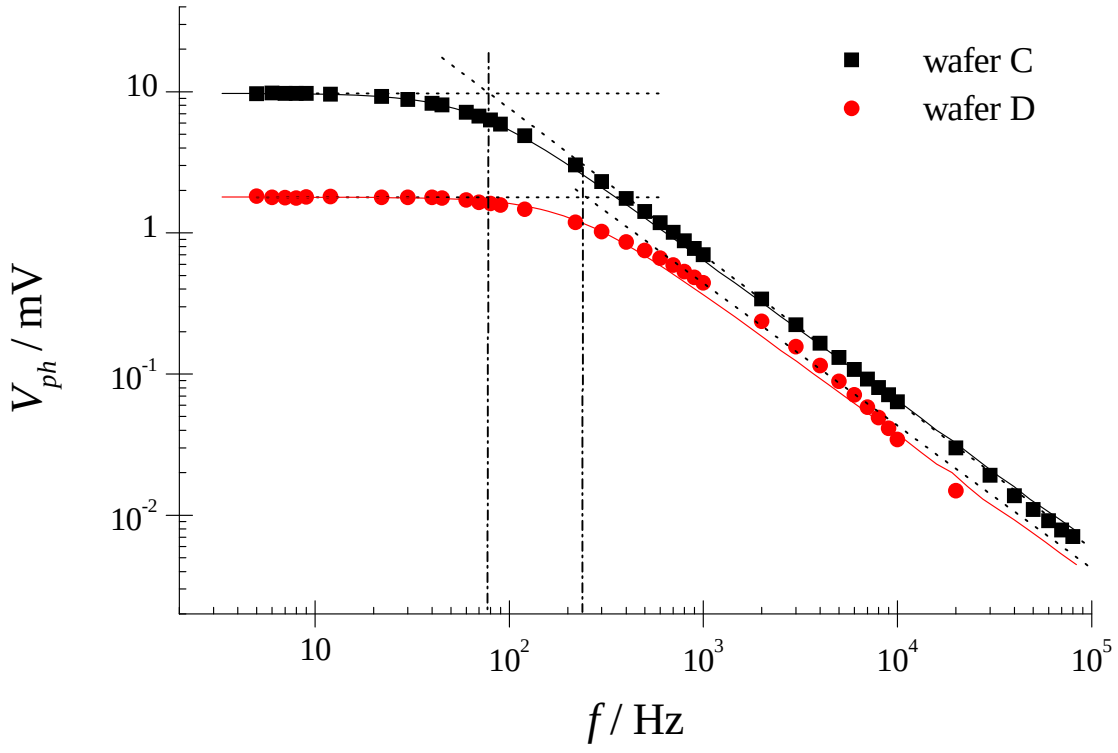

***Figure 6-33**. Frequency dependence of the ac-SPV measured on samples of wafer C and D at a photonflux of $9.25\times10^{12}cm^{-2}s^{-1}$ with the high impedance amplifier. The dotted lines are least square fit functions of the data in the low and high frequency region with the intercept of both lines giving the cutoff frequency f_c. The full lines are the SPV data calculated via equation 6-53 after determining the surface potentials and impedances from the respective cutoff frequencies.*

The frequency dependence of the ac-photovoltage measured on samples of both the clean and the iron contaminated oxidised wafers C and D is plotted in figure 6-33. As discussed in the theory of the ac-SPV, see §6.4.2, the photovoltage in the low frequency region is governed by the majority carrier conductance g_{mj} and is thus independent of frequency. whereas at higher frequencies the depletion layer capacitance dominates the surface impedance and thus $V_{ph} \propto f^{-1}$. Both regions can be clearly observed in the photovoltage curves in figure 6-33. The dotted lines indicate the least square fit functions obtained from the data points in the low and high frequency region. The cutoff frequency of the curve, f_c, was determined from the intercept of these functions The parameters for the wafer samples obtained from this measurement are listed in table 6-2 where the surface potential ψ_S was found by numerically solving equation 6-73 and Q_{SS} and g_{mj} via equations 6-32 and 6–64, respectively. The total surface charge Q_{SS} is given in number of elementary charges per unity area.

***Table 6-2**. Summary of the ac-SPV measurement results.*

wafer sample	f_c **/ Hz**	g_{mj} **/ Sm^{-2}**	ψ_S **/ mV**	Q_{SS} **/ cm^{-2}**
C	79.2	0.057	455.5	6.30×10^{10}
D	249.2	0.184	426.4	6.07×10^{10}

We observe distinctly different surface parameters for the clean and Fe contaminated wafer samples C and D, respectively. Similar to the results obtained with the saturation SPV technique, we find that the Fe contamination reduces the surface charge and therefore the surface potential. The lowering of ψ_S causes a significant increase in the majority carrier conductance and thus a reduced magnitude of the SPV in the low frequency region. Although the values of ψ_S are slightly higher than those obtained via the saturation SPV technique it has to be considered that the values given here are single

point measurements whereas the saturation SPV results are average values obtained from a scan over the whole wafer area.

A more simple method to obtain the cutoff frequency is shown in figure 6-34 where the transient of the photovoltage was recorded on a sample of wafer C. We see that the transient follows an exponential decay with a specific time constant τ which is thus related to the cutoff frequency via

$$f_c = \frac{1}{2\pi} \cdot \frac{1}{\tau} \qquad \textit{6-89.}$$

and therefore to g_{mj} and c_{dp} with equation 6-73:

$$\tau = \frac{c_{dp}}{g_{mj}} \ . \qquad \textit{6-90}$$

Although the measurement was not taken under exactly the same conditions as the ac-SPV versus frequency curve shown in figure 6-33, the resulting surface potential of ψ_S = 442.9mV is close to the result obtained above.

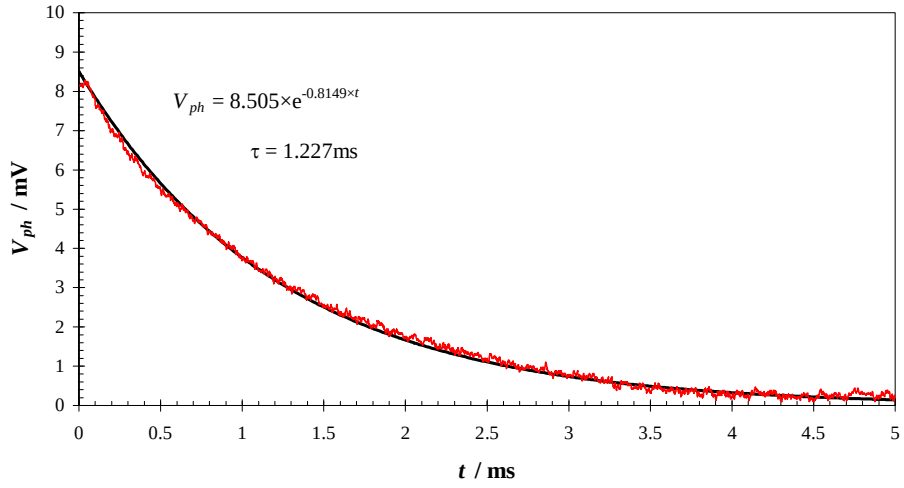

***Figure 6-34**. SPV transient recorded on sample C using a square wave modulated light signal and the high input impedance amplifier.*

6.4.5 Discussion

We can conclude from these measurements that the experimental results agree with the ac-SPV theory outlined in §6.4.2 if the photovoltage is measured in the linear region, i.e. below 10mV. For the case that the semiconductor surface impedance is governed mainly by the majority carrier conductance and depletion layer capacitance the surface potential can be determined from the cutoff frequency of the photovoltage versus frequency curve or, indeed, via the time constant of the SPV transient.

We find that both the saturation and ac-SPV method yield a lower surface potential and surface charge for the Fe contaminated wafer compared to the clean sample. We can therefore conclude that either method can be used as an indicator for potential chemical contamination of semiconductors. Most of the controversial issues raised in the discussion of the saturation SPV technique however can be avoided with the ac-SPV method since only low light intensities are used and therefore this method will yield the more reliable results.

REFERENCES

1. K. Graff, *Metal Impurities in Silicon Device Fabrication*, Springer Series in Materials Science 24, edited by H.J. Queisser, (Springer, Berlin 1995).

2. W.H. Brattain and J. Bardeen, *Bell System Tech.* J. **32**, 1 (1953).

3. L. Kronik, Y. Shapira, *Surf. Sci. Rep.* **37**, 1 (1999).

4. B. Lägel, I.D. Baikie, U. Petermann in *Defect and Impurity Engineered Semiconductors and Devices II*, edited by S. Ashok, J. Chevallier, K. Sumino, B.L. Sopori, W. Goetz, (Mater. Res. Soc. Proc. **510**, Pittsburgh, PA, 1998), pp. 619-625.

5. B. Lägel , I.D. Baikie, U. Petermann, *Surf. Sci.* **433-435**, 622 (1999).

6. C. Munakata, S. Nishimatsu, N. Honma and K. Yagi, *Jpn. J. App. Phys.* **23**, 1451 (1984).

7. W. Mönch, *Semiconductor Surfaces and Interfaces* (Springer Series in Surface Science **26**, Springer, Berlin, 1995).

8. S.M. Sze, *Physics of Semiconductor Devices* (John Wiley & Sons, New York, 1981).

9. E.O.Johnson, *Phys. Rev*. **111**, 153 (1958).

10. L.J. Brillson, D.W Kruger, *Surf. Sci.* **102**, 518 (1981).

11. H.C. Gatos, J.Lagowski, *J. Vac. Sci. Technol.* **10**, 130 (1972).

12. O.B. Aphek, L. Kronik, M. Leibovitch, Y. Shapira, *Surf. Sci.* **409**, 485 (1998).

13. E.O.Johnson, *J. Appl. Phys*. **28**, 1349 (1957).

14. A.M. Goodman, *J. Appl. Phys*. **32**, 2550 (1961).

15. P. Edelman, J. Lagowski and L. Jastrzebski in *Photo-Induced Space Charge Effects in Semiconductors*, edited by D.D. Nolte, N.M. Haegel and K.W. Gossen.

16. H. Shimuzu and C. Munataka, *Appl. Phys. Lett.* **62**, 276 (1993)

17. G. Zoth and W. Bergholz, *J. Appl. Phys.* **67**, 6764 (1990).

18. P. Horowitz, W. Hill, *The Art of Electronics* (Cambridge University Press, Cambridge, 1980) pp. 92-99.

19. Standard Operating Procedure for RCA Clean, available [online], http://www-mtl.mit.edu/~hoang/sop/rca.html [03/08/2000].

20. Handbook of Chemistry and Physics, 74th ed., edited by D. R. Lide (CRC Press, Boca Raton, 1993-1994), p. **12**-105.

21. P. Roman, I. Kashkoush, R. Novak, E. Kamieniecki and J. Ruzyllo, in *4th International Symposium on Cleaning Technology in Semiconductor Device Manufacturing* (Electrochemical Society Proceedings, **95-20**, 1995) pp. 344-349.

22. H. Dember, *Z. Physik* **32**, 554, 856 (1932).

23. C. Munakata, S. Nishimatsu, *Jpn. J. App. Phys.* **25**, 807 (1986).

24. C. Munakata, *Jpn. J. App. Phys.* **27**, 759 (1988).

25. Book of ASTM Standards **10.05**, F391a (1994).

26. E.J. Ryder, *Phys. Rev.* **90**, 766 (1953).

27. E.H. Nicollian and A. Goetzberger, *Bell Syst. Tech. J.* **46**, 1055 (1967).

28. A.S. Grove: Physics and Technology of Semiconductor Devices (John Wiley & Sons, Neew York, 1967).

29. W. Shockley, W.T. Read, *Phys. Rev.* **87**, 835 (1952).

30. H. Shimizu, K. Kinameri, N. Honma and C. Munakata, *Jpn. J. App. Phys.* **26**, 226 (1987).

Summary

This thesis reports on the application of the Kelvin probe in materials science and in particular on the study of metal and semiconductor surfaces in both ambient and UHV environments. We introduce in chapter 1 the two main topics of this thesis, namely (i) the production and characterisation of polycrystalline metal targets for advanced mass spectroscopy systems and (ii) the detection of defects and impurities in semiconductor substrate wafers.

In chapter 2 we discuss the concept of the work function and the importance of this parameter in materials science. The various methods to determine the work function are reviewed, i.e. the direct measurement methods via thermionic, photo and field- emission and surface ionisation as well as the diode and the Kelvin method which are indirect techniques. The advantages and disadvantages of these methods are discussed. The Kelvin method and the technical realisation of the probe are described in greater detail.

A novel approach to determine the work function by a combination of the photoelectric effect and the Kelvin method is presented in chapter 3. The development of this technique was driven by the requirement for the *absolute* work function of the specimen, rather than the data *relative* to the reference tip measured by the Kelvin probe, without giving up on the numerous advantages of the Kelvin probe; the novel method thus combines the benefits of both methods. The work function of the Kelvin probe tip is determined from the I-V characteristics of the diode arrangement formed by a low work function surface used as a source of photo-emitted electrons and the probe tip acting as the collector. The work function of any metal or semiconductor surface can be determined by subsequent CPD measurements with the Kelvin probe. This approach

has the further advantage of making full use of the existing instrumentation of the Kelvin probe with only a minimum of additional components.

The production and evaluation of high and low work function surfaces as target materials for a novel ion source based on hyperthermal surface ionisation is discussed in chapter 4. Five metal surfaces were studied: tungsten, molybdenum, rhenium, palladium and platinum. The highest work function of 7.15eV could be obtained via oxidation of rhenium (Re) at ~900K. Re has the further advantage of having a high melting point of 3180°C and is very stable to thermal cycling. Low work function lanthanum hexaboride (LaB_6) and calcium (Ca) surfaces were created via e-beam evaporation and gadolinium (Gd) via thermal cleaning of the metal foil. The lowest work function of ~2.54eV was measured on LaB_6 followed by Ca (2.92eV) and Gd (~3.08eV). Exposure to the residual gas at a pressure of 3.7×10^{-9} Torr revealed however that the lowest work function surface is also the most unstable. At 300K the work function of LaB_6 increases to 3.65eV after an exposure of 200L whereas Gd increases by only 70meV.

The process of thermal and hyperthermal surface ionisation (SI, HSI) as well as the generation of hyperthermal molecular beams is discussed in chapter 5. A simple model for the SI process is developed to estimate the ionisation efficiency of the model gas NO_2 on the high and low work function surfaces. We find that the ionisation efficiency depends exponentially on the factor $\Delta E/kT$, where ΔE is the energetic difference between the work function of the target surface and the ionisation potential or electron affinity for positive and negative SI (p-SI, n-SI), respectively. . Although experimental data of NO_2 positively ionised on oxidised Re follow the exponential relationship, the experimental parameters fitted to the equation of the ionisation efficiency do not agree with the model. This is presumably due to the fragmentation of NO_2 observed in p-SI

or, indeed, the use of a too simplistic model. Mass spectrometric data of p-SI show a fragmentation of NO_2 into mainly O_2^+, NO^+ and O^+ whereas n-SI produces a single peak at mass 48 which can be identified as NO_2^-. Negative SI and HSI data indicate a considerable increase in the work function of the LaB_6 target surface upon exposure to NO_2 even at elevated temperatures causing a substantial decrease in the ionisation efficiency. The ion current measured as a function of the NO_2 inlet pressure shows a change in the gradient of the curve between 0.7Torr and 0.9Torr using an inlet nozzle of diameter 0.5mm. This effect can be interpreted as the transition between thermal and hyperthermal surface ionisation.

The application of the Kelvin probe for the detection of defects and impurities in semiconductors, namely iron contamination, is demonstrated in chapter 6 via two methods based on the measurement of the surface photovoltage (SPV): (i) the saturation and (ii) the ac-SPV technique. With both methods the surface potential and thus the surface charge can be determined which are indicators of potential contamination on substrate wafers. We find that both methods yield a lower surface potential and surface charge for iron contaminated wafers compared to a clean sample. However, since the saturation SPV is determined under very high light intensities a number of secondary effects have to be considered that might interfere with the signal to be measured. Most of these problems can be avoided with the ac-SPV method where only low light intensities are used and therefore this technique will yield the more reliable results.